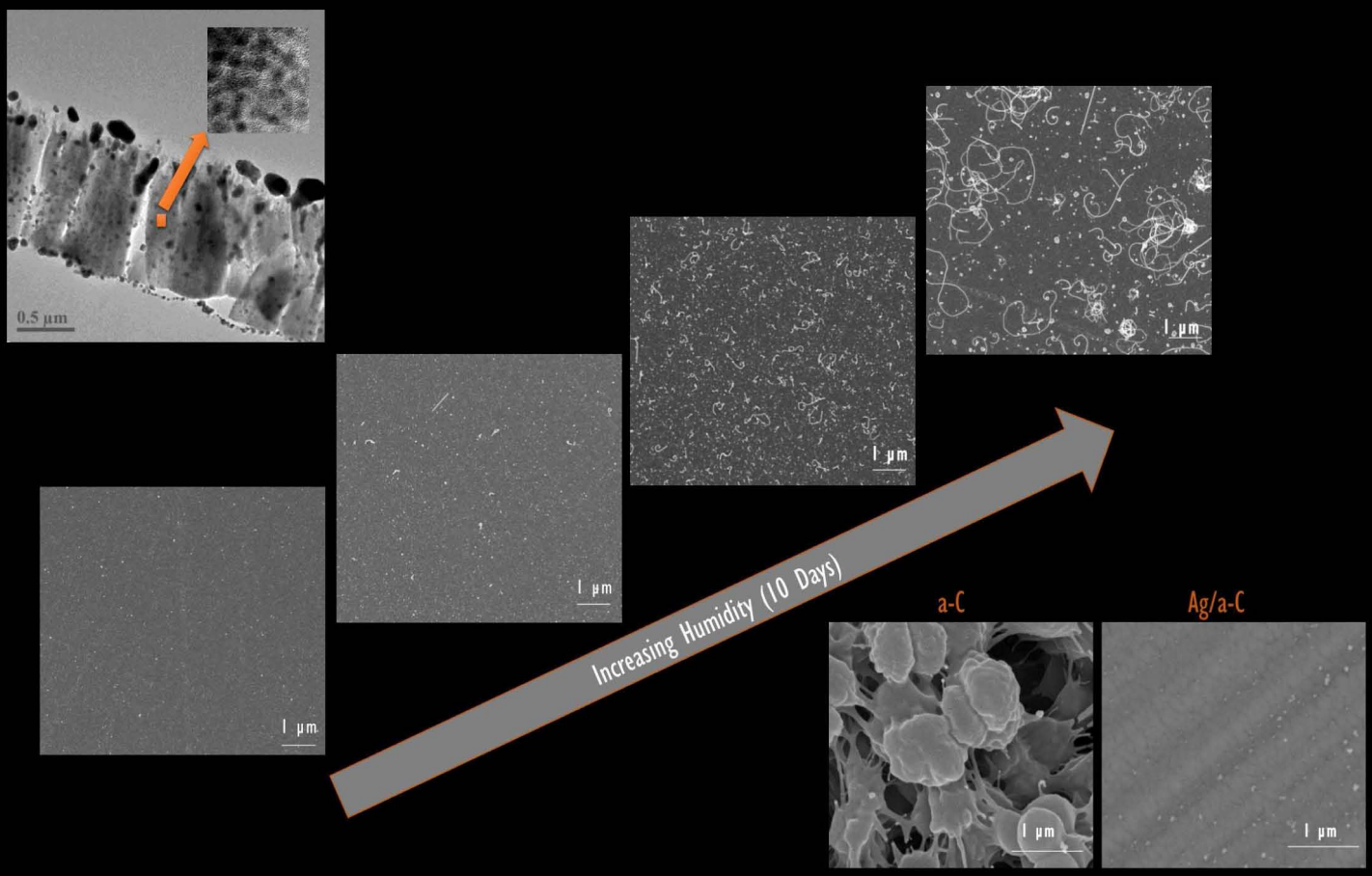

Noora Kristiina Alves de Sousa Manninen

SILVER SEGREGATION IN Ag/a-C NANOCOMPOSITE COATINGS FOR POTENTIAL APPLICATION AS ANTIBACTERIAL SURFACES

Doctoral Thesis in Mechanical Engineering, branch Surface Engineering, supervised by Professor Doctor Albano Augusto Cavaleiro Rodrigues de Carvalho and Professor Doctor Sandra Maria Fernandes Carvalho, submitted to the Department of Mechanical Engineering, Faculty of Sciences and Technology of the University of Coimbra.

September 2015

· U C ·

UNIVERSIDADE DE COIMBRA

• U C •

FCTUC FACULDADE DE CIÊNCIAS
E TECNOLOGIA
UNIVERSIDADE DE COIMBRA
DEPARTAMENTO DE ENGENHARIA MECÂNICA

Silver segregation in Ag/a-C nanocomposite coatings for potential application as antibacterial surfaces

Noora Kristiina Alves de Sousa Manninen

Doctoral Thesis in Mechanical Engineering, branch Surface Engineering, submitted to the Department of Mechanical Engineering, Faculty of Sciences and Technology of the University of Coimbra

Supervisors

Professor Doctor Albano Cavaleiro

Professor Doctor Sandra Carvalho

Coimbra

2015

Technical Sheet

Author: Noora Kristiina Alves de Sousa Manninen

Title: Silver segregation in Ag/a-C nanocomposite coatings for potential application as antibacterial surfaces

Editor: Department of Mechanical Engineering, Faculty of Science and Technology

Cover: The cover images show three figures that briefly summarize the thesis work:

Top left: TEM cross-sectional micrographs of Ag/a-C nanocomposite coating

Centre: SEM micrographs of Ag/a-C coatings evolution in a period of 10 days in environments with different humidity levels

Bottom right: SEM top-view micrographs of a-C and Ag/a-C coatings after the interaction with *Staphylococcus epidermidis*, showing the antibacterial activity of Ag containing coating

Bolsa de Doutoramento financiada por:

(SFRH/BD/82472/2011)

À minha avó Esteri, aos meus pais e irmãos

Poets say science takes away from the beauty of the stars - mere globs of gas atoms. I, too, can see the stars on a desert night, and feel them. But do I see less or more?

Richard Feynman

Acknowledgements

A realização de uma tese de doutoramento e trabalho de investigação envolve a colaboração e trabalho de equipa entre várias pessoas e instituições às quais manifesto o meu profundo e sincero agradecimento.

Em primeiro lugar quero agradecer aos meus orientadores, Professor Doutor Albano Cavaleiro e Professora Doutora Sandra Carvalho. Em 2008 enquanto aluna da Licenciatura de Engenharia de Materiais iniciei a minha atividade como investigadora com orientação da Professora Sandra que encorajou fortemente a iniciação do meu trabalho no mundo da investigação. Desde então tenho colaborado com a Professora Sandra que ao longo destes anos tem revelado uma disponibilidade e paciência inesgotáveis, contribuindo e encorajando a minha evolução na vida académica. Durante este percurso a Professora Sandra proporcionou-me a oportunidade de trabalhar sobre a orientação do Professor Albano no grupo SEG-CEMUC. Esta foi uma oportunidade única que me permitiu trabalhar com o Professor Albano por quem manifesto uma enorme admiração e apreço pelo seu conhecimento científico e pela capacidade, paciência e humildade com que o transmite aos mais "pequenos" como eu. Obrigada por tudo!

Gostaria de agradecer ao Professor Valdemar como presidente do CEMUC pela oportunidade de trabalhar num centro de investigação de elevada qualidade.

Um agradecimento especial a todos os elementos do grupo SEG-CEMUC em especial ao Doutor João Carlos Oliveira, Doutor Manuel Evaristo, Doutor Ricardo Serra e Nuno Figueiredo por todo o apoio prestado ao longo da realização desta tese. Gostaria também de agradecer ao grupo de Nanomateriais e Microfabricação, em especial à Professora Doutora Teresa Vieira. Agradeço os colaboradores do Led e Mat do IPN em especial o Engenheiro João Paulo e Engenheira Ana Manaia, António Fonseca, Bruno Martins, Carlos Patacas e João Costa por toda a disponibilidade e ajuda incansável em inúmeras situações, em especial pela ajuda na implementação do sistema de deposição de nanopartículas e na resolução de problemas durante o seu funcionamento. Agradeço ainda aos meus colegas da Universidade do Minho Cristiana Alves, Edgar Carneiro, Isabel Carvalho, Isabel Ferreri, Mariana Marques, Rita Rebelo, Sebastian Calderón e Simone Rodrigues.

Presto também um agradecimento especial ao Professor Doutor Paulo Ferreira da Universidade do Texas, Austin, e aos seus colaboradores e alunos que contribuíram para a minha evolução científica, quer através do apoio técnico na realização de análises de microscopia eletrónica de transmissão, quer através de discussões científicas.

Cabe ainda um agradecimento especial ao Doutor Ramon Escobar Galindo com quem tenho colaborado desde 2010 até à presente data. Obrigada pela colaboração, paciência e dedicação ao trabalho que desenvolvemos durante estes anos.

Gostaria de agradecer ao Professor Doutor Tomas Polcar pela colaboração e pelo interesse manifestado no trabalho que tenho desenvolvido no âmbito da tese.

Agradeço ainda a Fundação para a Ciência e Tecnologia pela concessão da bolsa de doutoramento SFRH/BD/82472/2011 sem a qual a realização deste doutoramento não teria sido possível.

Por fim gostaria de agradecer à minha família, em especial aos meus irmãos Heidi e Pedro, que sempre me encorajaram a seguir em frente e a lutar pelos meus objetivos, que sempre me dedicaram a atenção e carinho que necessitava nos momentos mais difíceis os quais muitas vezes não consegui retribuir durante este percurso. Espero conseguir compensar-vos de todos esses momentos e certamente e tal como sempre a minha motivação para fazer sempre melhor serão vocês. Durante este percurso tive a oportunidade de conhecer novas pessoas que hoje se tornaram amigos que jamais esquecerei pelos bons momentos que me proporcionaram durante a minha estadia em Coimbra e que tiveram um papel fundamental para eu seguir em frente nos momentos mais difíceis. À Ana Escudeiro, André Cavaleiro, Carla Lopes, Fábio Ferreira, Fábio Ribeiro, Filipe Fernandes, Maria João Madeira, Rita Farinha, Rita Santos e Sílvia Godinho.

Obrigada a todos!

Abstract

The development of antibacterial surfaces represents a great challenge in different industrial applications, namely, medical devices, food packaging industry, textiles or aquatic flow systems. Most of living bacteria are found to grow in biofilms which strongly adhere to different types of surfaces, where they find a strategic survival mechanism. This phenomena leads to the failure of different types of materials used in the above mentioned applications, which represent a huge economic loss and also an public health concern when it comes to fields such as medical devices or food packages. In this sense over the past years the development of antibacterial surfaces has been pointed as a new strategy for the development of more efficient materials to be applied in different industrial sectors.

This thesis deals with the development and characterization of multifunctional amorphous carbon coatings doped with Ag nanoparticles (Ag/a-C) for potential application in antibacterial surfaces. Ag is nowadays pointed as the most effective bactericidal agent, which is already the leading material in nanotechnology market. In other hand, the strategy of surface modification with amorphous carbon (a-C) coatings has become very popular due to its unique tribological properties, which allow to combine high hardness and low friction coefficient, chemical inertness and biocompatibility, just to name some of its properties, which has prompted its use in different applications, namely, medical devices, razorblades, mechanical components with enhanced tribological performance. In this sense, the incorporation of Ag nanoparticles within a-C coatings can be regarded as a promising approach for achieving multifunctional properties in different applications, such as medical devices.

In the present thesis Ag doped a-C nanocomposite coatings are deposited by two alternative deposition methods based on physical routes: (i) dual magnetron sputtering and (ii) combination of magnetron sputtering for a-C layer deposition and plasma gas condensation for Ag nanoparticles *in-situ* incorporation in the host matrix. The above mentioned deposition methods are compared with respect to the uniformity in the deposition of large surface areas, which allowed to select the most suitable deposition method (magnetron sputtering).

The Ag/a-C nanocomposite coatings are characterized with respect to their structure, thermodynamic stability at room temperature conditions and functional properties (antibacterial activity and tribological behavior). The core thesis work is focused in Ag/a-C nanocomposite coatings containing 20 at.% of Ag, with different thicknesses/morphologies and different multilayer structures.

The results suggest that Ag/a-C coatings are unstable even at atmospheric conditions, being found that Ag grows within the coatings column boundaries forming Ag nanowhiskers, which cover the coatings surface few weeks after deposition. The process of Ag nanowhiskering is found to be promoted by the humidity, being found that particles grew through a coalescence process.

The functional properties suggest that Ag/a-C coatings are promising in terms of antibacterial activity, which is correlated with the Ag ionization. The tribological tests reveal that in dry sliding condition Ag promotes a degradation in a-C coatings tribological properties; however, in biological medium simulating the synovial fluids, found in joint prosthesis, the tribological behavior is similar to the a-C layer.

Keywords: Ag/a-C nanocomposites, Ag nanoparticles, Coatings Structure, Coatings Stability, Antibacterial Surfaces

Resumo

O desenvolvimento de superfícies antibacterianas representa um desafio atual em diferentes aplicações industriais, nomeadamente, dispositivos médicos, embalagens alimentares, têxteis e sistemas de tratamento de água. A maioria das bactérias existe em biofilmes que aderem fortemente a diferentes tipos de superfícies uma vez que esta adesão representa um mecanismo estratégico de sobrevivência. O fenómeno da adesão e colonização microbiana resulta na falha de diferentes dispositivos e componentes utilizados nas aplicações acima mencionadas, tendo como consequência perdas económicas elevadas e representando também um problema de saúde pública quando se tratam de aplicações como dispositivos médicos ou embalagens alimentares. Neste sentido, ao longo das últimas décadas o desenvolvimento de superfícies antibacterianas tem sido considerada uma estratégia emergente no desenvolvimento de materiais mais eficientes a serem aplicados em diferentes sectores.

O objetivo da presente tese consiste no desenvolvimento e caracterização de revestimentos nanocompósitos multifuncionais baseados em revestimentos de carbono amorfo dopado com nanopartículas de prata (Ag/a-C) para potencial aplicação em superfícies antibacterianas. A Ag é atualmente considerada como o agente bactericida mais promissor e eficiente, sendo que as nanopartículas de prata representam o material mais comercializado na área da nanotecnologia. A estratégia de modificação superficial com revestimentos baseados em carbono amorfo (a-C) tem-se tornado popular do ponto de vista industrial essencialmente, devido entre outras propriedades, à sua resistência ao desgaste tribológico excecional, que permite combinar uma elevada dureza com um baixo coeficiente de atrito, elevada estabilidade química, resistência à corrosão e biocompatibilidade em diferentes aplicações biomédicas. Na atualidade os revestimentos de a-C são utilizados em diferentes aplicações industriais nomeadamente dispositivos médicos, lâminas de barbear e diferentes componentes mecânicos sujeitos a elevado desgaste tribológico. Neste sentido, a combinação das propriedades intrínsecas destes materiais pode ser considerada uma abordagem promissora para o desenvolvimento de revestimentos multifuncionais, os quais podem ser aplicados em diferentes produtos, nomeadamente, dispositivos médicos.

Na presente tese os revestimentos nanocompósitos de Ag/a-C são depositados por dois métodos distintos: (i) pulverização catódica em magnetrão e (ii) combinação da pulverização catódica em magnetrão para deposição da camada de a-C e condensação em atmosfera inerte para a incorporação simultânea de nanopartículas de Ag na matrix de carbono. Os métodos acima mencionados são comparados em relação à uniformidade dos revestimentos depositados, permitindo efetuar a escolha do método de deposição mais eficaz (pulverização catódica em magnetrão).

Os revestimentos nanocompósitos de Ag/a-C são caraterizados relativamente à sua estrutura, estabilidade termodinâmica em condições ambientais e propriedades funcionais (comportamento tribológico e atividade antibacteriana). O trabalho central da tese é focado na caraterização de revestimentos Ag/a-C contendo 20% at. de Ag, com diferentes espessuras e diferentes estruturas em multicamada.

Os resultados sugerem que os revestimentos Ag/a-C são instáveis mesmo em condições ambientais, sendo observado que a Ag forma nanofibras entre as fronteiras das colunas, as quais recobrem a superfície do revestimento poucas semanas após a produção. O processo de formação de nanofibras é promovido pela humidade, sendo que, as partículas crescem através de um processo de coalescência.

As propriedades funcionais sugerem que os revestimentos Ag/a-C são promissores do ponto de vista de actividade antibacteriana, a qual está relacionada com a sua ionização. Os testes tribológicos revelam que em ambiente não lubrificado a presença da Ag promove a degradação dos revestimentos a-C, contudo, em meios biológicos que simulam o líquido sinovial, presente nas articulações da anca, o comportamento tribológico é semelhante aos revestimentos a-C.

Palavras-Chave: Nanocompósitos de Ag/a-C, Nanopartículas de Ag, Estrutura dos revestimentos, Estabilidade dos revestimentos, Superfícies antibacterianas

List of Abbreviations

Abbreviations

a-C	amorphous Carbon
AFM	Atomic Force Microscopy
BSA	Bovine Serum Albumin
BSE	Backscattered Electrons
CoF	Coefficient of Friction
DLC	Diamond Like Carbon
EDS	Energy Dispersive Spectroscopy
EPA	Environmental Protection Agency
EPMA	Electron Probe Micro-Analysis
FDA	Food and Drug Administration
GDOES	Glow Discharge Optical Emission Spectroscopy
GIXRD	Grazing Incidence X-Ray Diffraction
HAI	Hospital Acquired Infection
HBSS	Hank´s Balanced Salt Solution
ICDD	International Center for Diffraction Data
ICP-OES	Inductively Coupled Plasma Optical Emission Spectroscopy
ISO	International Organization for Standardization
MeN	Metal Nitride
MS	Magnetron Sputtering
NP	Nanoparticle
OCP	Open Circuit Potential
PBS	Buffered Saline Solution
PGC	Plasma Gas Condensation
PVD	Physical Vapor Deposition
RfD	Oral Reference Dose
RH	Relative Humidity
SEM	Scanning Electron Microscopy
SZM	Structure Zone Model
TEM	Transmission Electron Microscopy
WDS	Wavelength Dispersive Spectroscopy
XPS	X-Ray Photoelectron Spectroscopy
XRD	X-Ray Diffraction
ZoI	Zone of Inhibition

Symbols

Z	Atomic number	
A	Atomic weight	[g/mol]
N	Avogadro´s Number	
θ	Bragg angle	[°]
V_b	Breakdown voltage	[V]
μ	Chemical potential	[J/mol]
α_c	Critical angle for total external reflection	[°]
D_g	Crystallite grain size	[nm]
ρ	Density	[g/cm^3]
R	Depth of analysis	[μm]
Ø	Diameter	[cm], [nm]
D	Diffusion coefficient	[cm^2/s]
D^0	Diffusion pre-factor	[cm^2/s]
E	Energy	[J]
EB	Binding energy	[eV]
KE	Kinetic energy	[eV]
G	Gibbs free energy	[J/mol]
h	height	[cm],[nm]
Pm	Mean Hertzian contact pressure	[Pa]
M	mass	[kg]
λ_m	Mean free path	[nm]
θ	Residual stress	[Pa]
R_a	Average roughness	[nm]
2θ	Scattering angle	[°]
S	Sputtering Yield	
γ	Surface energy	[J/m^2]
T	Temperature	[°C] [K]
t	Time	[s][min]
K_O	Incident wave vector	
K_f	Exit wave vector	
α	X-rays incidence angle	[°]
λ	X-rays wavelength	[Ä]

Table of Contents

List of Figures

List of Tables

Introduction

Microbial adhesion and consequent biofilm formation has been pointed as a major concern in different industrial applications. Microbial biofilms are defined as "microcosm attaching irreversibly to abiotic or biotic surfaces and promulgated as congregates of single or multiple populations" (Tamilvanan). Biofilm formation represents a strategic growth mechanism, which allows the microbes to survive even in hostile environments. The growth of these microorganisms in different surfaces such as medical devices, food packages and water treatment systems represents a public health concern, since the interaction of bacteria with these surfaces results in hospital acquired infections (HAI), foodborne and waterborne diseases, which still represent an important cause of mortality. In addition, biofilms also cause severe problems in industrial settings, such as pipes in heating systems or marine structures, since the presence of bacteria in these surfaces enhances the corrosion rate and consequently the degradation of these structures.

In the present scenario, surface modification and incorporation of nanoparticles (NP´s) in different materials have gained great popularity for the development of antibacterial surfaces, where different nanoparticles emerged as potential bactericidal agents, namely, silver, zinc oxide and titanium dioxide. Silver, has been used as antibacterial agent since 1000 B.C. and by this time it was used to store drinking water. Later and until 1940 when penicillin was introduced this metal was used for the treatment of burns and chronic wounds. More recently, the emergence of antibiotic resistant bacteria has prompted the interest in silver based products, which efficiency has largely increased due to the possibility of their production and control at nanoscale level, with the help of nanotechnology; hence, it has been possible to increase the materials reactivity and, consequently, to enhance their functional properties. In fact, nanotechnology is presently pointed as a rapidly growing field, with the number of consumer products increasing from 54 in 2005 up to 1628 in 2013. Among them, 383

products are antibacterial Ag based materials, which, presently, find numerous applications, in textiles, food packages, air purifying systems, dietary supplements, just to name a few.

Regarding the development of antibacterial surfaces containing silver, different concepts have been studied, namely, (i) direct incorporation of Ag nanoparticles in the surface of textiles and polymers and, (ii) deposition of different coatings incorporating silver. In the case of silver containing ceramic coatings produced by magnetron sputtering, different systems have been studied namely transition metal nitrides (TaN,TiN,CrN,ZrN), oxides (TiO_2, ZnO), carbonitrides (TiCN,) as well as carbon based coatings (a-C, commonly known as diamond like carbon (DLC)), which allow to combine the wear and corrosion resistance inherent to the base coating with the Ag antibacterial effect. This deposition process allows depositing a ceramic coating in which Ag precipitates as nanoparticles, due to its low solubility in these ceramic matrixes. Despite the promising results achieved with some nanocomposite coatings, namely Ag/a-C, the antibacterial efficiency of these materials is far from being understood and, thus, controlled. In fact, it has been reported that in some matrixes, namely TiCN, no antibacterial activity was achieved, while, in other systems, the fast and uncontrolled release of silver during the first hours of antibacterial tests undermines the long term antibacterial activity of these coatings.

Ag based nanocomposite coatings have been studied not only due to their potential antibacterial activity, but also due to the possibility to combine hard ceramic coatings (e.g. CrN, YSZ) with a soft lubricant Ag phase. These materials have been largely studied in last decades for high temperature tribological applications. In addition, the incorporation of noble metal nanoparticles, such as gold and silver in dielectric matrixes allows to tailor the optical properties, which has prompted the interest in several applications, namely, decorative coatings and gas sensors. However, the use of silver based nanocomposite coatings is limited, owing to the low stability of these metal nanoparticles in different matrixes. In many cases, silver has been often replaced by gold, due to the higher stability of Au nanoparticles, which despite its much higher cost is pointed as a cost effective solution for industrial applications. Silver surface segregation and surface nanoparticles growth has been reported by several authors, in different magnetron sputtered coatings (mainly on transition metal oxides and nitrides) although

the exact mechanism and driving force for these Ag segregation is far from being understood and, thus, controlled.

1. Motivation and work objectives

The main goal of the thesis is the development of multifunctional surfaces, through the surface modification of metallic substrates with magnetron sputtered amorphous carbon coatings containing silver (Ag/a-C). As previously mentioned, Ag is presently pointed as the most promising and efficient bactericidal agent. The combination of Ag nanoparticles with amorphous carbon coatings, many times designated as DLC – diamond-like carbon, allows the development of multifunctional nanocomposite coatings, able to combine high wear and corrosion resistance inherent to a-C coatings, with silver´s antibacterial activity. Moreover, a-C coatings are biocompatible, being presently used in different industrial applications, such as, joint prosthesis, uretheral stents, cardiovascular stents, medical instruments, razor blades and also in different mechanical components. CarboSoft™ (Optimed) and Medthin™ (Ionbond) represent some of the commercially available carbon coatings used in different biomedical devices.

Ag/a-C nanocomposites are deposited by two different approaches: (i) magnetron sputtering (MS) and combination of magnetron sputtering and plasma gas condensation (MS+PGC). MS deposition method is widely used for Ag-nanocomposites deposition; conversely the hybrid MS+PGC method is an innovative approach for Ag/a-C coatings deposition, being this deposition system implemented in the research group (SEG-CEMUC) in the scope of the present work. The main advantage of this technology is to allow a more precise control in nanoparticles size distribution and chemical composition.

As previously mentioned one of the major concerns related with Ag based nanocomposites is the low stability of Ag nanoparticles, which makes difficult to control the particle size distribution due to the occurrence of particle agglomeration and, consequently, the long term functional properties are comprised. In fact, the properties of nanocomposite coatings are determined by the size and distribution of Ag nanoparticles; thus, the evaluation of their morphology and stability is a key issue in the

control of the coatings functionality. The phenomena of silver surface segregation and agglomeration have been previously reported, although the mechanisms and driving force for this process are still poorly understood, despite the large number of publications regarding Ag based nanocomposites. Thus, one of the main focus of the thesis is the evaluation of the stability of Ag/a-C nanocomposites over time as well as the understanding of the mechanism for Ag surface segregation in amorphous carbon matrix. The influence of coatings ageing, with consequent Ag surface segregation and agglomeration, on the functional properties is also studied as well as the possible solutions which enable to avoid or reduce the Ag surface segregation and agglomeration process in carbon coatings.

2. Work methodology and thesis organization

The present thesis is organized in six chapters, which contents are summarized in the scheme of figure 1.

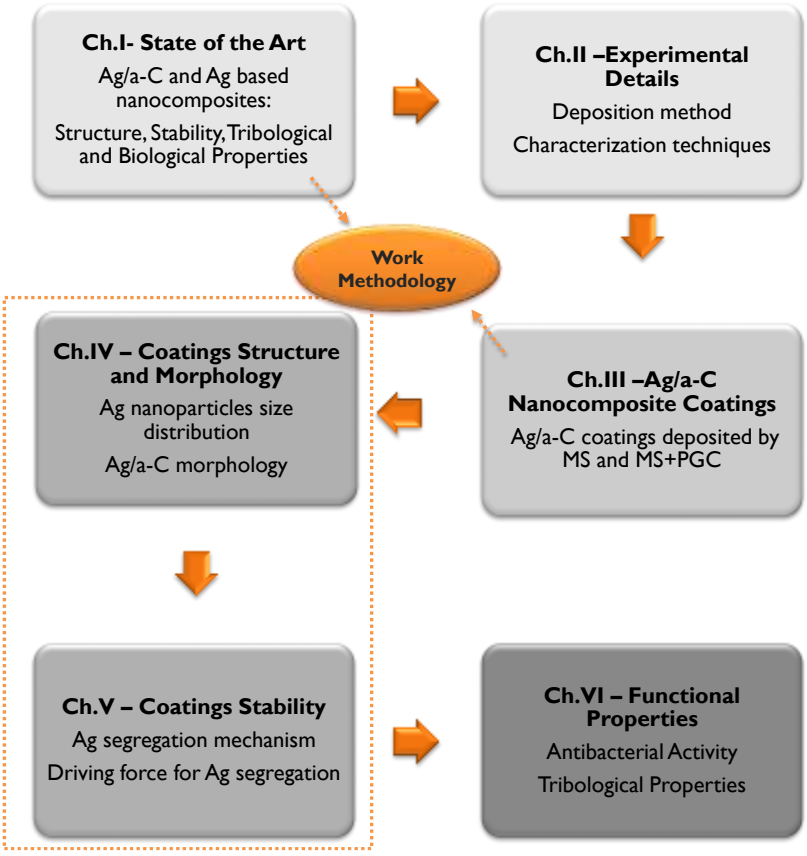

Figure 1 - Schematic representation of work structure and chapters contents

The first chapter (Chapter I- State of Art) aims to give the general background about Ag/a-C and Ag based nanocomposites, where the results related with coatings structure, stability, tribological and biological properties are reviewed.

Chapter II, Experimental Details, contains all the information about the methodology adopted for coatings preparation and characterization. The theoretical description of the deposition processes and characterization techniques necessary for the results interpretation is also given.

In Chapter III, Ag/a-C nanocomposites deposited either by magnetron sputtering (MS) and hybrid deposition method (magnetron sputtering (MS) and plasma gas condensation (PGC)), are analyzed in order to get some insights about the system structural features and tribological properties. It should be pointed out that the hybrid deposition method studied in the present work represents an innovative technological approach for the deposition of a-C/Ag nanocomposite coatings, being the PGC deposition system implementation one of the main goals of the present work. The above mentioned deposition methods are compared in relation to the Ag size distribution and coatings uniformity, which allowed to select the most adequate deposition method used in the subsequent work. At this stage the first conclusions about the coatings instability in atmospheric conditions are observed, which allowed to set the guideline for the development of the thesis core work.

Chapter IV is dedicated to the evaluation of the coatings structural and morphological features; the main focus is given to the evaluation of Ag nanoparticle size distribution along the coatings thickness as well as to the determination of the developed structural morphology.

In Chapter V the coatings stability is analyzed; some conclusions in relation to Ag segregation mechanisms and driving forces for the process occurrence are drawn.

Chapter VI is focused on the evaluation of the coatings functional properties: the antibacterial activity and the tribological behavior.

Chapter I

State of the Art

In this Chapter an overview of Ag/a-C and Ag nanocomposite coatings deposited mainly by magnetron sputtering within ceramic matrixes (transition metal nitrides, carbonitrides and oxides) is provided. The most relevant works are summarized in what regards the most important topics of the present thesis: coatings structure and morphology, stability, mechanical and tribological properties as well as their antibacterial activity.

1. Ag/a-C nanocomposite coatings

Carbon based coatings represent one of the most valuable engineering materials found in present days. These coatings were first discovered in 1950s by Schmellenmeier, however, the research in carbon coatings only gained a momentum in 1990s. Since then, the number of publications and patents on carbon coatings has largely increased and, presently, they can be found in different industrial applications ranging from microelectronics, optics, transportation to biomedical field[1].

Carbon is one of the most common elements in earth and it can be found in nature in different allotropic forms, such as graphite or diamond. The carbon coatings physical and chemical properties are determined by their structure, a topic which is nicely reviewed by Robertson[2]. The large variety of physical properties is mainly related with the different hybridization states present in carbon coatings (sp^1, sp^2 and sp^3), where the presence of sp^3 bonds, characteristic from diamond, leads to high hardness, chemical and electrochemical inertness, while the presence of sp^2 bonds, characteristic from graphite, allow to obtain low friction coefficient and high electrical conductivity, just to mention a few characteristics. The different forms of DLC coatings are displayed in a ternary phase diagram, developed by Jacob and Moller[3], where the amounts of $sp^3$and sp^2 bonds and hydrogen determine the type of achieved structure (see figure 2).

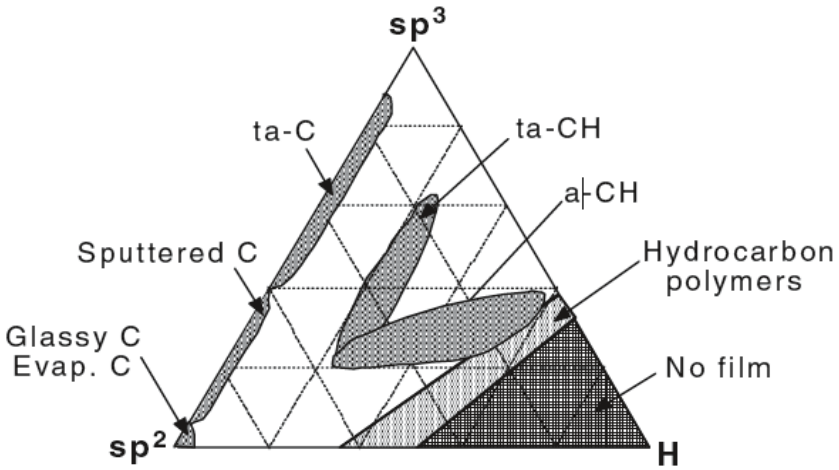

Figure 2 - Phase diagram of DLC coatings[1]

Since their discovery and industrial implementation, carbon based coatings have been largely studied in order to improve the specific required properties, which vary according to the desired application. The incorporation of different metallic and non-metallic elements allows to tailor the carbon coatings functional properties, e.g. hardness, residual stress, electrical resistivity, surface energy, just to mention few[1]. Among different alloying elements, silver has become very popular owing to its interesting electrical/optical properties, tribological behavior and antibacterial activity. The number of publications along time, as well as the type of evaluated properties, are summarized in the graphs of figure 3 (a) and (b), respectively. This results were based on the revision of the papers related with Ag/a-C system performed by the author, in the ScienceDirect database, thus, it should be pointed out that some papers might be missing in this analysis.

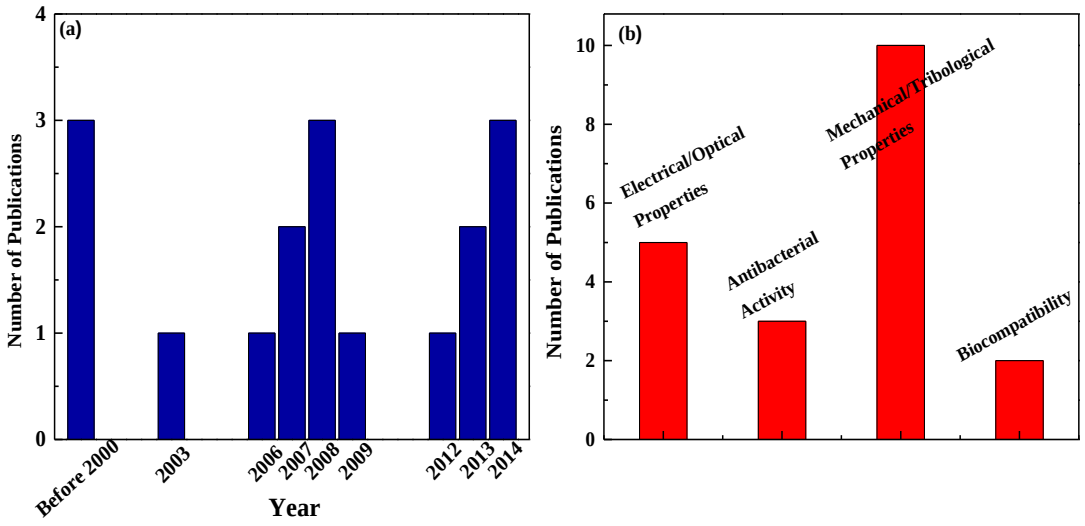

Figure 3 – (a) number of publications along time for Ag/a-C coatings and (b) number of publications per evaluated properties [4-21]

As can been found in the graph of figure 3 (a) the interest in Ag containing amorphous carbon coatings has raised during the 90´s, and, by this time, Biederman et al.[4,5,6] have studied the Ag/C:H system deposited by a hybrid magnetron sputtering and plasma enhanced chemical vapor deposition method in order to evaluate its structure, optical and electrical properties. Afterwards, in 2003, Narayan et al[7] evaluated the applicability of pulsed laser deposited nanostructured Ag/a-C composites for biomedical applications, through the study of their morphology, structure, hardness and

antibacterial susceptibility. The authors compared an uncoated silicon substrate with an Ag/a-C coating in a disk diffusion test with a total duration of 24 hours and found that *Staphylococcus aureus* did not grow over the Ag nanocomposite surface, thus suggesting that the Ag containing coatings presented antibacterial activity. Moreover, different research groups have been studying the mechanical, tribological, electrical and biological properties of these nanocomposite coatings in order to evaluate their applicability in different fields, such as in medical devices, sliding machinery components, protective layers or advanced sensors. An overview of these studies is given in this section, which focus mainly on the coatings structure, the tribological behavior and the biological activity.

1.1 Structure and Morphology

The growth mode and binding state of an element in carbon coating is mainly determined by its affinity with carbon. Thus, in case of carbide forming elements, the metallic component will form chemical bonds with carbon, which results in the dispersion of carbides in the carbon structure. In the case of noble metals, with low affinity to carbon, typically the metallic atoms will grow as a second phase, forming clusters or nanoparticles[1]. The phase diagrams allow to predict which type of structure will be formed as a function of the chemical composition. Since the envisaged coating structure in the present work is an amorphous carbon matrix with Ag nanoparticles, the first step is to guarantee that the amount of Ag incorporated is above the solubility limit of Ag in carbon. According to the calculated phase diagram of graphite – silver shown in figure 4, the solubility of Ag in carbon is zero, which means that in theory whatever is the chemical composition, Ag should segregate as a second phase in the carbon matrix.

The structure and morphology of Ag/ a-C coatings has been described in every paper regarding this system. However, in this review only the summary of the work performed in the papers where a more detailed structural analysis is performed is given. It should be pointed out that the main structural and morphological results are related with the phase composition, the size and distribution of Ag nanoparticles and the influence of Ag incorporation in the amorphous coatings structure, mainly in the variation of sp^2/sp^3 ratio.

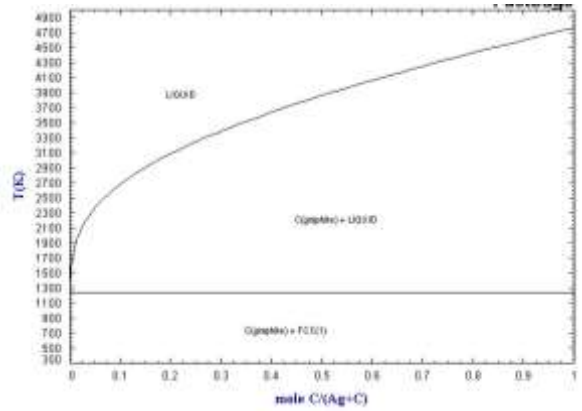

Figure 4 - Ag-C calculated phase diagram[8]

Choi et al[9] prepared hydrogenated amorphous carbon coatings deposited with Ag by a hybrid ion beam deposition method, combining decomposition of benzene and dc magnetron sputtering of silver. The structure of the coatings containing between 0 at.% and 9.7 at.% of Ag was analyzed. High resolution transmission electron microscopy (HRTEM) revealed that up to Ag concentration of 0.1 at.%, an uniform amorphous structure was observed, being concluded that all Ag atoms were fully dissolved in the amorphous carbon matrix. At higher Ag concentrations, silver started to segregate as a second phase, forming initially very small Ag nanocrystals with 2 nm diameter (1.7 at.%) and, for higher silver concentrations (9.7 at.% Ag), a crystalline fcc-Ag was detected, with silver particle size from 4 to 6 nm. Raman spectroscopy allowed to find that for 0.1 at.% Ag no changes in carbon structure were observed, while, for a further increase in the amount of Ag, an increase in the D/G peaks intensity ratio and narrowing of G peaks were observed, which are related to an increase in the amount and size of graphite like features in the amorphous carbon matrix.

Matenoglou et al[10] deposited non-hydrogenated amorphous carbon/silver nanocomposites by pulsed laser deposition. A detailed structural characterization of the Ag/a-C coatings deposited with different Ag/C atomic ratios was performed and the discussion was focused on the influence of the negative bias voltages applied to the substrate holder. The sp^2/sp^3 bonds fraction, determined by Auger electron spectroscopy (AES), was dependent on the Ag content, having been observed its increase with the presence of Ag. The grain size of Ag nanoparticles was determined by X-ray diffraction (XRD) analysis (by applying the Scherrer method) and the in-depth grain size distribution across the coatings thickness was investigated by varying the X-

rays incidence angle, below (at 0.3°) and above (at 0.6°) the coatings critical angle, which was reported to be at 0.4-0.5°. The XRD analysis revealed the presence of crystalline Ag phase and no differences in grain sizes across the coatings thickness, indicating a homogeneous size distribution. The Ag grain size was reported to increase as a function of Ag content.

Zang et al[11] deposited hydrogenated and non-hydrogenated amorphous carbon coatings containing 0 at. % and 5.5 at. % of Ag by plasma immersion ion implantation method. X-ray photoelectron spectroscopy (XPS) showed that Ag was present in metallic state. Regarding the carbon bonding state, sp^2 and sp^3 bonds were detected and quantified as a function of Ag incorporation. In non-hydrogenated coatings the amount of sp^2 bonds increased with silver incorporation while for non-hydrogenated coatings no changes were observed. This result is consistent with the observations found through Raman spectroscopy analysis in another report from same authors[12], although, not consistent with the quantification of sp^2 bonds achieved with X-ray absorption near edge spectroscopy (XANES) which suggested that the incorporation of silver had no effect on the carbon structure.

In summary the main conclusions achieved in relation to the coatings structure and morphology are:

- Ag segregates as a second phase in an amorphous carbon matrix forming crystalline nanoparticles which size depends on the specific deposition method, deposition parameters and also on its amount; the size of silver nanoparticles increases with the amount of Ag,
- The incorporation of Ag reduces the amount of sp^3 bonds in non-hydrogenated amorphous carbon coatings; this result is attributed to the presence of a ductile phase, which reduces the internal stress, characteristic of sp^3 bonding.

1.2 Stability

Biederman et al[4] found that the electrical and optical properties of Ag/C:H thin films varied with time, which was attributed to the changes in the Ag particles size distribution. The coatings were analyzed by TEM, in relation to both Ag particle size distribution and nearest neighbor distance, immediately, 2 and 10 days after deposition.

The authors found that both particles size and interparticle distance increased more significantly with time during the first two days, than thereafter with the nearest neighbor distribution starting at 4 nm and increasing up to 5 nm after 2 days, while after 10 days the distance shifted back to 4 nm.

Onoprienko et al[13] analyzed the microstructrural evolution of carbon thin films with 11 at. % of Ag during annealing at 600°C in vacuum by TEM. The as-deposited coating could be characterized by a bi-modal size distribution, with a few Ag-NP, 30 nm in diameter, combined with a larger density of smaller particles. Upon increasing the annealing time the particles average diameter increased along with an overall decrease in the areal density, which was attributed to the particle coalescence induced by temperature. The authors found that the rate of particle increase was higher than that predicted by the theory behind coalescence induced by diffusion.

In summary the main conclusions achieved in relation to the coatings stability are:

- Ag/a-C:H coatings change their functional properties (optical and electrical) within few days (2 to 10 days) due to the changes in Ag size distribution and interparticle distance;
- Ag particles coalesce in a-C matrix coatings submitted to annealing at a rate faster than predicted by coalescence and diffusion theories.

1.3 Mechanical and tribological properties

Choi et al[9] studied the residual stress state and hardness with Ag incorporation for the coatings already presented above in the 1.1 section. The incorporation of small amounts of Ag (1.7 at.%) gave rise to a great reduction in the coatings residual compressive stresses from 2.9 GPa down to 1.6 GPa, while for higher Ag contents the decrease was much smoother (down to 1.3 GPa at 9.7 at.% of Ag). The coatings hardness also decreased from 22.6 GPa down to 16.9 GPa when 9.7 at.% of Ag was incorporated. This results showed that Ag/a-C coatings might be promising from the mechanical point of view since they enable to reduce the coatings residual stress without degrading significantly their hardness values.

Wang et al[14] deposited Ag/a-C coatings by dual magnetron sputtering with Ag contents ranging from 0 at.% up to 24.7 at.% having determined a reduction of the compressive residual stresses from 3174 MPa down to 1310 MPa. This reduction had a significant positive impact on either the adhesion critical loads measured by scratch testing or on the cracks density induced by Rockwell C indent. Similar behavior with Ag incorporation was also reported by Narayan et al[7], who also found a reduction in the coatings hardness.

Wu et al[15] deposited Ag/a-C:H coatings by magnetron sputtering, with Ag contents ranging from 0 to 11 at.%. Similar trends to those reported by Choi et al[9] were found for the residual stress and hardness. The tribological properties of the coatings were evaluated in a ball-on disk tribometer in vacuum conditions against a steel counterpart. The Ag incorporation did not significantly changed the friction coefficient (CoF), although, for the sliding lifetime an inverse trend was shown depending on the Ag content: in relation to the Ag-free coating, it was improved for low Ag content (3.55 at.%) while for the highest Ag concentration (11 at.%) the coating lifetime was degraded. The degradation of tribological properties with the addition of high amounts of silver was attributed to the lower hardness resulting from either the increased graphitization or the presence of the softer Ag phase. Regarding the coating with 3.55 at.% Ag, the improved tribological behavior was attributed to the compromise between a still hard coating with the presence of a protective layer formed by low shear Ag clusters on the surface, which can be maintained over the time due to the diffusion of Ag from the bulk to the worn area, as observed by SEM analysis. In fact, the authors observed the presence of more Ag inside the wear track in relation to the unworn coating. Another interesting feature was the increase in CoF at the end of the tribological test, attributed to the progressive reduction of Ag concentration on the worn surface combined with the increase of the wear debris amount.

Dhandapani et al[16] studied Ag/a-C coatings deposited by rf magnetron sputtering onto SS316L substrates with increasing Ag contents up to 8.37 at.%. The tribological tests were performed in a reciprocating tribo-tester against alumina counterpart in dry sliding conditions. Ag-containing coatings showed a lower CoF in relation to pure a-C coating; however, the lowest CoF values were achieved with the coatings with lower Ag contents (2.9 and 4.4 at.% of Ag). The coatings with the highest Ag contents (5.4 and 8.3 at.%) showed a non-steady trend with the CoF increasing from about 0.3 up to 0.5 after

about 200 sliding cycles. Conversely, the coatings with no Ag and with lower Ag content showed stable and approximately constant CoF during the whole test. The wear rates were well correlated with the CoF values, i.e. the coatings with lower friction also showed lower wear rate. The increased wear rate in the coatings with higher Ag content was attributed to their lower hardness. The authors also claimed that the lower wear resistance could be related to an increase of the adhesion between the coating surface and the alumina counterpart.

In summary the main conclusions regarding the mechanical and tribological properties are:

- The incorporation of Ag even in small amounts promotes a reduction in residual stress of the coatings with a consequent improvement in the mechanical stability of the coating over the substrate;
- The presence of Ag reduces the coatings hardness, due to the intrinsic low hardness of Ag combined with the reduction in the amount of sp^3 bonds of the carbon matrix;
- The presence of small amounts of Ag (below 5 at. %) improves the coatings tribological behavior by reducing the CoF and the wear rate. At higher Ag concentrations an opposite effect is observed.

1.4 Biological properties

To the authors knowledge the first author to evaluate and report the potential antibacterial activity of Ag doped amorphous carbon coatings was Narayan et al[7]. Later on, two other studies were reported, which are now being reviewed in this chapter.

Morrison et al[16] deposited Ag/a-C, Pt/a-C and Ag,Pt/a-C coatings by pulsed laser deposition. TEM analysis showed that Ag and Ag,Pt formed nanoparticles with an average size from 3 to 5 nm, which were distributed in the amorphous carbon matrix. The antimicrobial activity against *Staphylococcus warneri* revealed that Ag/a-C and Ag,Pt/a-C reduced the biofilm formation at a rate of 50% and 90% , respectively, in relation to the uncoated substrate (silicon). The improved antibacterial activity of Ag,Pt doped coatings in relation to Ag doped coatings was attributed to the formation of a galvanic couple between Ag and Pt, which tends to enhance the silver ionization rate and consequently

its antibacterial activity. This topic will be reviewed in one of the following sections where the mechanism of Ag antimicrobial activity is analyzed.

K.Baba et al[18] prepared hydrogenated Ag containing a-C films by a combination of magnetron sputtering (for Ag deposition) and plasma source ion implantation (for the carbon deposition), with Ag contents between 0 and 27 at.% of Ag. The antibacterial tests were performed with *Staphylococcus aureus* bacteria and the activity was measured at different interval times. All Ag-containing coatings showed an antibacterial effect of about 80 %, and no linear relationship between the Ag content and the antibacterial activity was observed. The authors attributed this non-linear trend to the differences found in the coatings structure and morphology with Ag incorporation, which tends to promote an increase in the coatings roughness, in sp^2 bonds and in Ag particle size, which of them with its specific role in the antibacterial activity.

Despite the evaluation of antibacterial activity, the biocompatibility and protein adsorption in Ag-containing carbon coatings has also been subject of two different reports. Endrino et al[12] evaluated the cell survival and proliferation using mouse MC3T3 osteoblastic cells. The authors tested the cell survival rate of these cells in both a-C and a-C:H coatings with 0 and 5.5 at.% Ag, and they found that both types of amorphous carbon coatings can be considered biocompatible *in vitro*, despite the more favorable results achieved with a-C ones. The Ag incorporation did not lead to any statistical difference in relation to the Ag-free coating. Choi et al[19] evaluated the adsorption ratio of albumin and fibrogen in plasma to investigate the heamo-compatibility of Ag/a-C coatings deposited by a hybrid deposition method. The authors reported that by increasing the amount of Ag in a-C coatings, the protein adsorption rates increased, which makes them suitable for biomedical devices where very good heamo-compatibility is required, such as in cardiovascular stents.

In summary the main conclusions regarding the biological behavior of Ag/a-C nanocomposite coatings are:

- The nanocomposite coatings show good antibacterial activity against *Staphylococcus warneri* and *Staphylococcus aureus* bacteria. The antibacterial activity does not increase linearly with Ag content, being dependent on other structural and morphological features: amount of sp^2 bonds, roughness and Ag particle size,

- The incorporation of Ag (with Ag content up to 5 at.%) does not comprise the cell survival and proliferation (using mouse MC3T3 osteoblastic cells) of plasma immersion ion implanted a-C and a-C:H coatings,
- The incorporation of Ag in a-C coatings enhances the protein adsorption (albumin and fibrogen).

2. Ag based nanocomposite coatings

In this section an overview of Ag based nanocomposite coatings is given. It should be pointed out that the number of papers in this subject is very large (in the order of thousands of papers). The huge number of studies in Ag-NP and Ag-NP based coatings reflects the large interest in this metal, which has become very popular over the past decades, mainly due to its antibacterial activity, tribological properties, optical and electrical behavior. Thus, not all the papers are covered in this review. The main focus is given to those related with the objectives to be accomplished under the scope of this thesis. The overview is divided in three main sections: (i) structure and morphology of Ag based nanocomposite coatings, (ii) stability of Ag in nanocomposite coatings, and their tribological properties and (iii) biological activity. The cited papers are mainly related with the ceramic matrixes (transition metal nitrides, oxides, carbides and carbonitrides) incorporating Ag deposited mainly by magnetron sputtering, which represent the most common matrix coatings in magnetron sputtered Ag based nanocomposite coatings.

2.1 Structure and morphology

Similarly to what is observed in amorphous carbon coatings, the inclusion of Ag in different matrixes (namely TiN[22], CrN[23],TiO_2[24],SiC[25],HfC[25],ZrCN[26],TiCN[27]) leads to the growth of crystalline fcc-Ag clusters or nanoparticles, which is attributed to the low solubility of Ag in these different compounds. The increase in Ag content promotes an increase in the size of Ag nanoparticles[27] although other deposition parameters also play an important role in the size distribution of Ag nanoparticles. Despite the evolution of

Ag particle size, other interesting results have been reported regarding the Ag size distribution across the coatings thickness, which are also reviewed in this chapter.

Los Arcos et al[22] deposited Ag/TiN nanocomposite coatings by reactive magnetron sputtering. The evolution of Ag nanoparticles size distribution was studied by scanning electron microscopy (SEM) and transmission electron microscopy (TEM) as a function of the coatings thickness, the Ag content, the deposition temperature and the bias voltage applied to the substrate holder. The growth of Ag nanoparticles was better fitted with bimodal log-normal distributions, with the second mode particles (with bigger sizes and lower density) shifted towards bigger sizes as the coatings thickness or the Ag content increased. Two modes of distribution were shown to exist: embedded "trapped" clusters, and surface clusters, the latter being formed by diffusion of silver to the surface of the film where a process of coalescence with other surface clusters can occur. Surprisingly, by increasing the deposition temperature (from room temperature to 325°C) the size of Ag clusters decreased, even though their density increased. The amount of silver determined by XPS was approximately double in all heated samples, which was attributed to a redistribution of the surface silver clusters, which cover a larger part of the surface. Moreover, the total amount of silver able to diffuse to the surface during the deposition process also increased.

Chakravadhanula et al[24] investigated the in-depth size distribution of Ag and Au clusters incorporated on amorphous TiO_2 coatings through electron tomography. Ag and Au clusters grew with a biomodal size distribution, where bigger nanoparticles (with a diameter of 7 nm in case of Ag) were located at the coatings surface while smaller nanoparticles (2 nm) were embedded in the matrix. A two-step model was proposed to explain this distribution: in a first step, occurring during vacuum phase co-deposition, the formation of the smaller particles took place; the second step occurred after deposition leading to the formation of the bigger particles on the surface. According to this model, single silver atoms or very small clusters can diffuse in the matrix or on the surface, as long as the surface is not covered by the atoms of the matrix material. During the formation of the small nanoparticles, surface diffusion processes are probably dominant, but their growth is restricted since they are covered relatively rapidly by the matrix material. In the second step, when the deposition is stopped, silver atoms, and possibly very small clusters, diffused from the bulk (near surface region) to the surface to form larger nanoparticles which, then, grew by fast surface diffusion processes. These

larger particles were coarsened via Ostwald ripening and surface segregation processes. The model is summarized in figure 5 together with the TEM cross sectional micrograph of an Ag/TiO_2 coating.

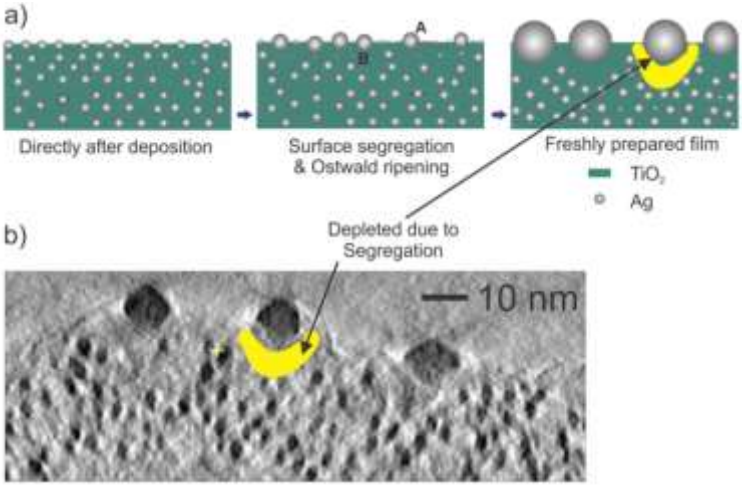

Figure 5 - (a) Model showing the two step model involved in the formation of Ag-TiO_2 nanocomposite coating developed by Chakravadhanula et al[26] and (b) TEM cross-sectional micrograph of the nanocomposite morphology

The authors claimed that the driving force for this process should be the large stresses associated with the growth of these coatings, combined with a fast kinetics for Ostwald ripening in the coatings surface. This bimodal size distribution and formation of a depletion zone below the coatings surface was also reported by Krzanowski et al[25] in SiC/Ag nanocomposites, although, the SEM cross-sections showed a much higher thickness of the depletion zone when compared to Chakravadhanula et al[24] study. In this case its thickness was about 50% of the total thickness, which was approximately 1 μm. The authors claimed that the development of this structure was related to the large positive heat of mixing between Ag and the carbide, and to the higher surface activity of Ag, which meant that placing silver on the surface reduces the free energy. The mechanism of Ag surface segregation was not perfectly understood by the authors, although they claimed that it was more likely that the observed film structures evolved during deposition, since the time required to cool from the deposition temperature of 200 °C down to below 100 °C is small compared to the time of deposition.

Escobar Galindo et al[28] evaluated the Ag in-depth distribution in Ag/TiCN nanocomposite coatings by three complementary techniques, (Rutherford backscattering spectrometry (RBS), glow discharge optical emission spectroscopy

(GDOES), and angle resolved X-ray photoelectron spectroscopy (ARXPS), and found an ultrathin (1 – 10 nm) Ag-rich layer on the coating surface followed by a silver depletion zone (20 –30 nm), being the thickness of both layers thicker for higher Ag contents and deposition temperatures. Conversely, Calderon et al[26] reported an homogeneous Ag in-depth distribution across Ag/ZrCN coatings with similar Ag contents, analyses performed also by RBS and GDOES.

Xiong et al[30] evaluated the Ag surface segregation in reactively sputtered Ag/TiO_x nanocomposite coatings, and found that Ag segregates to the surface even when a 60 nm thick TiO_x barrier layer was deposited on the top surface in the end of the coating process. The Ag surface segregation could only be stopped when the TiO_x barrier layer was dense enough, i.e. in their cases when it was deposited at high deposition rates and low deposition pressures.

In summary the main conclusions achieved in relation to the coatings structure and morphology are:

- Ag segregates as a second phase in an transition metal nitride, oxide, carbide and carbonitride matrixes forming crystalline nanoparticles which size depends on the specific deposition method, deposition parameters and also on its amount; the size of silver nanoparticles increases with the amount of Ag, similarly to what is observed in a-C coatings,
- Ag shows a bimodal size distribution in TiO_2, SiC, HfC and TiCN coatings deposited under specific deposition conditions, being found an Ag rich surface layer on the coatings outer surface followed by a depletion zone where the amount of Ag is lower in relation to the bulk as well as the particle size.

2.2 Stability

The most significant studies about Ag stability in nanocomposite coatings are provided in papers related with tribological properties at high temperature. In this section the most relevant works regarding the evaluation of Ag stability in different coatings are discussed, being the main emphasis given to the work developed by Voevodin and co-workers (from Air Force Research Laboratory) and Mulligan and co-

workers (from U.S. Army Armament Research Development & Engineering Center), who performed intensive studies on this subject.

Voevodin and his co-workers have been working on different Ag containing nanocomposite coatings over the past years, for the development of adaptive nanocomposite coatings, also known as "chameleon coatings", for aerospace applications. The main objective is to achieve materials that automatically adjust the surface composition and the structure to minimize friction as the environment changes, through the inclusion of elements that self-assemble into lubricious phases when exposed to a particular range of external conditions [31-33]. Among the different papers published by the group two of them are focused on the Ag diffusion, which are now summarized in this section [32,33].

Hu et al[32] deposited yttria-stabilized zirconia (YSZ) nanocomposite coatings alloyed with silver and molybdenum, using a hybrid process of filtered vacuum arc, magnetron sputtering and pulsed laser deposition. The objective was to study the tribological behavior at high temperatures, in particular the friction behavior. SEM cross sectional and top-view observation of the coatings after annealing at high temperatures were performed and XRD was applied for structural analysis. The experimental results are presented in the left side of figure 6 while a schematic representation of the silver diffusion mechanism is provided in the (right side). The annealed coating was composed by two distinct layers: an Ag depleted YSZ-Mo layer plus an Ag layer which covered the entire coatings surface, forming dense Ag grains with 1-2 μm, as shown on the SEM top-view micrograph. The Pt layer was deposited for protection during FIB cutting. The XRD analysis suggested an increase in both fcc-Ag and tetragonal ZrO_2 grain size after annealing at 300°C; however, neither the grain size nor the Ag particle size distribution were determined. The model proposed for the Ag diffusion (figure 6 right), explains how Ag segregates to the surface and forms the continuous Ag layer on the top. This behavior is far from that observed on macrocomposite coatings of the same type, such as NASA PS200 and PS300, which were produced by plasma spraying. In this case, the coatings are stable at these temperatures and no Ag segregation was observed. The differences between nanocomposite and macrocomposite coatings, containing similar volume of the silver phase, are attributed to two factors: (i) the larger surface area of smaller particles which provides a larger decrease in the grain boundary surface energy and (ii) shorter distance between the embedded silver nanograins.

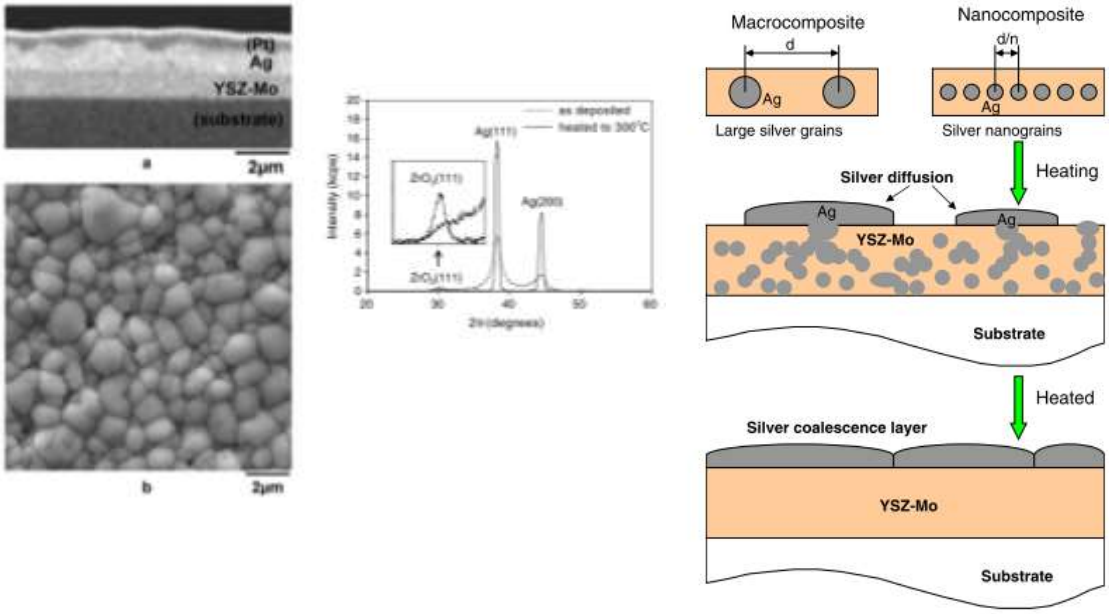

Figure 6 - SEM cross-sectional and top-view micrographs of YSZ-Ag-Mo (10 at.% Mo and 24 at.% Ag) after heating at 500°C and XRD diffractogram of the as-deposited and annealed coating (left) and schematic representation of the Ag diffusion after heating [32]

Since the coatings are completely dense and free of voids, there are space restrictions for Ag grain growth in the coatings bulk; thus, it is more likely that Ag diffuses to the coatings top-surface, where no space requirements restrict the silver coalescence. Still, the authors did neither observe nor commented what type of diffusion mechanism could be involved in the Ag diffusion to the surface, or in the Ag surface growth. The Ag incorporation was proved to improve the coatings tribological behavior, as observed for the CoF reduction, although a short lifetime was evaluated. The problem was that all silver diffused to the surface in approximately 45 minutes, at 500°C. In order to improve the coatings lifetime, the authors deposited a TiN diffusion barrier layer[33], with an array of pinholes.

The idea was to control the Ag surface segregation and, thus, to enhance the coatings lifetime over ten times. Ag could diffuse only through the pinholes present in TiN diffusion barrier layer, as depicted in figure 7. The cross-sectional SEM micrographs combined to EDS mapping allowed to observe the Ag diffusion to the surface and to determine the dimension of Ag depletion region, which was about 6 μm long. The authors used this value (as x) to determine the Ag diffusivity (D) in YSZ matrix at 500°C, assuming a parabolic diffusion, $x=\sqrt{Dt}$.

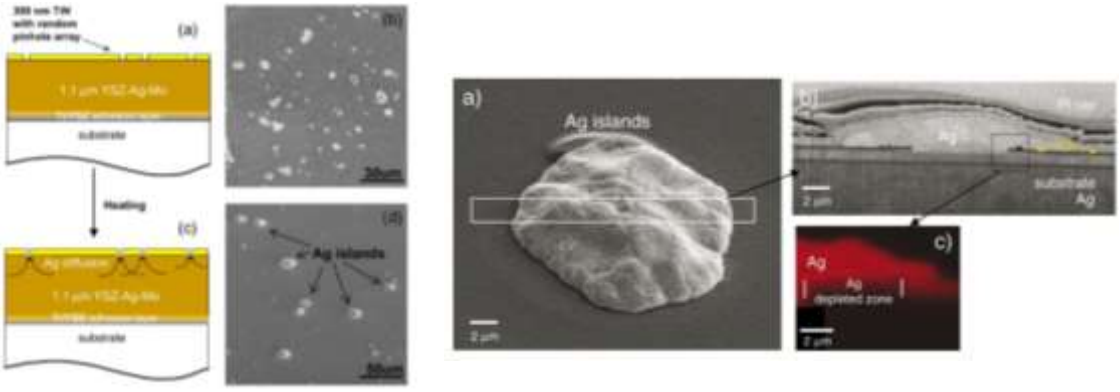

Figure 7 - (left) Schematic representation (a) and SEM top-view micrograph of pinholes in TiN mask (b), schematic representation of Ag diffusion through TiN mask (c) and SEM top view micrograph of YSZAgMo/TiN coating after heating at 500°C, (rigth) SEM micrograph showing the area selected for FIB cutting (a) coatings cross-sectional SEM micrograph after heating at 500°C (b) and EDS mapping of coating cross-section (c) [33]

The same methodology was adopted in order to determine the diffusivity at 425°C and 575°C, which allowed to built the Arhenius plot and thus, to determine the diffusion prefactor (D^0) and activation energy (E_a), which were reported to be $4.0x10^{-4}$ cm^2/s and 1 eV/atom, respectively.

Mulligan and co-workers have been studying Ag/CrN nanocomposite coatings deposited by reactive magnetron sputtering over the past decade with the aim of developing hard and wear resistant coatings with solid lubricant phase, Ag, for lubrication at high temperature (300°C-1000°C)[34-40]. In the first report found in literature [34], Ag/CrN coatings with different Ag contents (0, 3, 12 and 22 at.% Ag) were deposited and the effect of Ag content, annealing time (t_a = 5-60 minutes) and temperature (T_a = 600°C and 700°C) on the Ag-lubricant transport to the surface was studied. Ag segregated as a second phase in the crystalline CrN matrix being located at the column boundaries, which width was similar to the Ag grain size, evaluated through XRD analysis. The Ag lubricant transport to the coatings surface was analyzed through SEM top-view analysis, allowing to determine the areal density of Ag and the evolution of Ag particle size. The rate of Ag transport to the surface as well as the Ag agglomeration increased with either the Ag content incorporated in the coating or t_a and T_a. The Ag transport occurred mainly through the open column boundaries, which width increases with the Ag grain size. For this reason the amount of Ag on surface was 4 times higher when Ag content was doubled in the coatings, due to the increase in the volume of free surfaces between

CrN columns. In a subsequent paper, the authors developed diffusion barrier layers in order to prevent the fast Ag depletion and, thus, improve the coatings lifetime. In this study, Ag/CrN coatings containing 22 at.% Ag were covered by two CrN barrier layers, both with a thickness of 200 nm, but with different morphologies[36]. During annealing at 625°C for 20 minutes the porous CrN layer allowed the Ag to diffuse to the coatings surface, while the dense barrier layer completely avoided Ag diffusion to the surface. This allowed to prove that the presence of open spaces in the crystalline CrN matrix is a necessary condition for Ag diffusion, allowing to conclude that the diffusion rate in free surfaces is faster in relation to grain boundary diffusion or lattice diffusion. The effect of the coatings growth temperature, T_s, (300°C, 400°C and 500°C) on Ag diffusion at different annealing temperatures, T_a, (425°C, 525°C and 625°C) was also studied. The transport of Ag to the surface increased with T_a but decreased with T_s at a given T_a, e.g. for a coating deposited at 500°C the microstructure is stable up to 500°C; thus, a negligible effect in the Ag distribution after annealing was observed whenever $T_a<T_s$, as can be found in the SEM micrographs from figure 8 (left). When $T_a>T_s$, Ag diffuses to the surface at a rate that increases with T_a[37]. More recently, the authors published a paper entitled "Ag transport in CrN-Ag nanocomposite coatings"[39], where the same samples were analyzed by SEM (top-view and cross-sectional) and AES, in order to evaluate the depth profile distribution of silver, being some of the reported results presented in figure 8 (right). The SEM cross-sectional micrographs of the coating deposited at T_s=500°C indicated that in the as-deposited coatings Ag grew in a lamellar shape with an average width (parallel to surface) and height (in growth direction) of 50 nm and 25 nm, respectively. The cross-sectional micrographs were recorded in secondary electron + backscattered electron modes, thus, Ag appears brighter in the CrN matrix. The SEM micrograph after annealing at T_a=625°C, revealed the presence of lamellar voids (appear darker in the micrograph), resulting from the Ag that diffused to the surface for originating the large Ag agglomerates. The statistical analysis of the coatings micrographs allowed to conclude that the smaller grains disappeared during annealing, while the bigger grains remained unaffected, being the average width of the voids 20 nm.

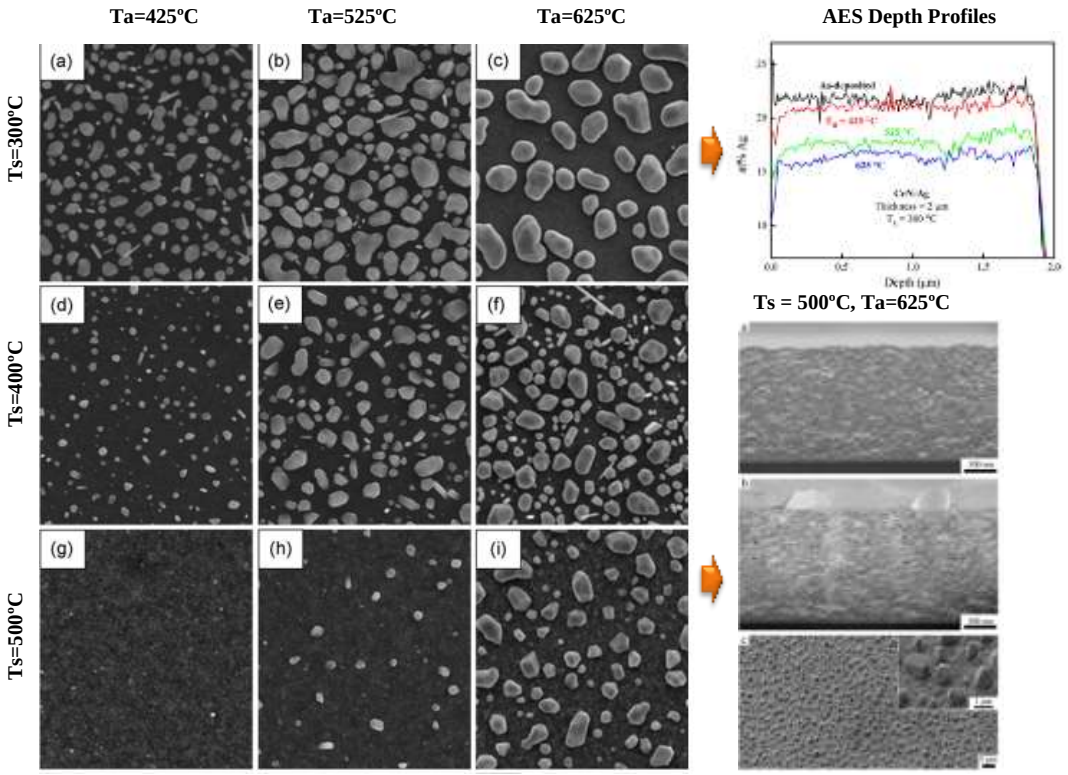

Figure 8 - (left) SEM micrographs of Ag-CrN coatings deposited and annealed at different temperatures (Ts and Ta) (right) AES depth profile of Ag-CrN coating deposited at 300°C and annealed at different temperatures and SEM cross-sectional micrograph of Ag-CrN coating deposited at 500°C and annealed at 625°C[37,39]

The AES depth profiles of the coating deposited at T_s=300°C and annealed at T_a=425,525 and 652 °C, suggested that the as-deposited coatings showed a constant Ag concentration of about 22 at. % across the coatings thickness. The annealed coatings also showed a constant in-depth Ag distribution; however, the amount of Ag is gradually reduced as the T_a increases, which means that Ag was diffusing from the entire coating thickness. It should be pointed out that before AES analysis the surface was polished in order to remove the segregated Ag, thus, the reduction in Ag content represents the amount of Ag that segregated to the coatings surface.

The driving force for this segregation was attributed to the larger chemical potential of smaller Ag clusters in relation to the larger Ag surface grains and coarsening through the Ostwald ripening mechanism[37,39].

In summary the main conclusions achieved in relation to the coatings stability are:

- Ag segregates to YSZ and MeN coatings surface when submitted to an annealing treatment at several hundred degrees;
- The deposition of a barrier layer based on MeN prevents the Ag surface segregation, which can be tailored by varying the barrier layer morphology/porosity. This indicates that Ag diffuses to the coatings surface through the column boundaries.

2.3 Biological properties/Antibacterial activity

Several mechanisms have been pointed to explain the antimicrobial activity of Ag nanoparticles, namely: (i) release of Ag^+ which reacts with thiol groups of proteins and interfere with DNA replication, (ii) generation of free radicals which damage the bacterial membrane and (iii) direct physical contact between the nanoparticles and bacterial cells which causes structural damage to their wall. Among the different proposed mechanisms, the Ag ions are pointed to be the most effective route for bacteria destruction[41-43]. Thus, in order to achieve the desired bactericidal effect it is necessary to guarantee that Ag based products are somehow transformed into Ag^+. Several fundamental studies regarding the bactericidal action of Ag nanoparticles against a wide range of microrganisms have been performed over the past years. The effect of nanoparticles size[43-46] and chemical properties[44] on the antibacterial effect have been evaluated. Most of the studies claim that smaller particles show an enhanced antibacterial activity and the presence of surface oxide layer enhances the bactericidal action.

The deposition of Ag thin films and incorporation of Ag nanoparticles in different matrix coatings has been followed by several research groups in order to produce multifunctional nanocomposite coatings as, for example, the incorporation of Ag nanoparticles in photocatalytic TiO_2 matrixes or the combination of hard/wear and corrosion resistant coatings, based on transition metal nitrides and carbonitrides, for prosthetic and dental implants. Some of the most relevant studies on this field are here reviewed.

Sant et al[47] deposited Ag based coatings by magnetron sputtering in order to evaluate the effect of different deposition parameters (input power, gas pressure and gas

composition) on the Ag dissolution rate and the antibacterial activity against *Staphylococcus aureus* and *Pseudomona aeruginosa*. The Ag coatings biological response was well correlated with the Ag ions dissolution rate, which was strongly dependent on several (micro)structural features, such as the nanocrystals size or the, presence of defects and oxygen species; smaller nanocrystals and defective crystals enhance the Ag ions dissolution rate. Pure silver was stable and not soluble in water. To promote its dissolution a driving force should be provided, which can be based in the presence of heterogeneities at microstructural level. Therefore the presence of minor impurities, local structural defects or differences in grain size distribution, could drive the dissolution process.

Unosson et al[48] deposited a gradient Ag-Ti oxide thin film by reactive magnetron sputtering and evaluated the effect of Ag content on the antibacterial activity against *S. aureus*. For high Ag content (62 wt.%) the viable count of *S.aureus* decreased by 99.6%, while at lower Ag contents (35 wt.%) only a reduction of 17% in relation to the control was observed after 2 hours of exposure. The variation of the antibacterial activity was well correlated with the Ag^+ ion release, which was much higher in Ag rich coatings, although it is not proportional to the variations in Ag content. Other factors, such as a higher porosity or a more hydrophilic character of Ag rich layers, which enhances the interaction with water molecules, are also claimed to be determinant on the Ag ion release.

Kelly et al[49] studied the antibacterial activity of CrN/Ag, ZrN/Ag, TiN/Ag and TiN/Cu systems with different Ag and Cu contents (about 5 at.%, 10 at.% and 20 at.%) against *P. aeruginosa* and *S. aureus.* The coatings structure was composed of MeN and Ag(Cu) crystalline phases. The incorporation of Ag resulted in the development of compact coatings, shown by SEM cross-sectional observations. A significant reduction in the number of viable cells with increasing Ag and Cu content is reported in relation to pure nitride coatings. Whilst no zones of inhibition were observed for *S. aureus*, on any of the surfaces, the diameter of the 'kill' zones generally increased with increasing silver content for *P. aeruginosa*. Moreover, despite the very similar morphology of the different nanocomposite coatings, CrN showed the best antibacterial efficiency while, for TiN matrix, the antibacterial activity was not observed. The influence of matrix coating on the antibacterial activity was not truly discussed in the paper.

Carvalho et al[50] evaluated the effect of surface features on *Staphylococcus epidermidis* adhesion to Ag/TiCN surfaces. The coatings were deposited by reactive magnetron sputtering (in $Ar+C_2H_2+N_2$ atmosphere) with varying Ag/Ti ratios (0, 0.37 and 0.62) and nearly constant N and C contents (about 30 at.% and 20 at.%, respectively). The coatings were composed of crystalline TiCN and Ag phases. With the increase in Ag content, TiCN grain size decreased, from 32 nm down to 5 nm, while Ag grain size increased from 19 nm up to 29 nm and a higher amount of amorphous phases based on a-C and a-CN were observed. Regarding the coatings morphological features, TiCN coatings were columnar, showing a very high porosity and a surface roughness of about 39 nm. The incorporation of Ag resulted in the development of more compact coatings with a lower average roughness (9 nm and 7 nm, for Ag/Ti of 0.37 and 0.62, respectively). The number of viable cells (*S.epidermidis*) revealed that the coatings did not show any antibacterial effect; SEM micrographs suggested that Ag containing coatings favor the bacterial adhesion and biofilm formation. The adhesion and proliferation of hydrophilic *S.epidermidis* strains were attributed to the surface properties, namely, to the more hydrophobic character of Ag based coatings in relation to TiCN. Moreover, the high densities of apolar areas in Ag containing coatings also promote the *S.epidermidis* adhesion. The lack of antibacterial effect was attributed to the possible absence of Ag ionization although the amount of Ag ions released to the medium were not determined in the study.

Ferreri et al[51] analyzed the antibacterial activity of sodium hypochlorite activated Ag/ZrCN based coatings deposited by reactive magnetron sputtering, containing 0 and 11 at.% of Ag. The zone inhibition (ZoI) tests revealed that ZrCN and Ag/ZrCN did not show antibacterial activity against *S.epidermidis*. Nevertheless, when Ag/ZrCN coatings were activated with NaClO (by immersion in 5% w/v solution before ZOI tests) a halo inhibition zone was observed, suggesting that antibacterial activity has occurred. SEM, XPS and GDOES analysis revealed that the activation process lead to an increase in the amount of Ag in the coatings surface after activation, resulting from the out-diffusion of Ag to from a few nanometers below the surface. A mechanism was proposed for explaining the Ag activation, which ends up in the formation of Ag ions, which are responsible for the antibacterial effect.

In summary the main conclusions achieved in relation to the coatings antibacterial activity is:

- Several Ag based nanocomposite coatings show good antibacterial activity against different type of bacteria. The antibacterial activity is dependent on coatings structure, morphology and nature of matrix coating. The presence of smaller Ag-NP, smaller nanocrystals size or the, presence of defects and oxygen species enhance the antibacterial performance,
- The antibacterial activity seems to be dependent also on the matrix nature nevertheless its exact influence is still poorly understood.

3. Soft metal whiskering

Despite being out of the scope of this thesis the phenomenon known as metal whiskering will be reviewed since this topic has been largely studied over the past decades. Several mechanisms regarding the formation of whiskers in coatings surface have been proposed, which will be important for the work presented in Chapter V-Section 2.

Metallic whiskers are a single crystalline filamentary eruption from a metal surface, which is generally observed in thin films, although it can also occur in bulk materials[52]. Metallic whiskering was first reported in the 1940´s and, presently, this phenomenon is still under extensive study since it is one cause of failure of different electronic devices (namely heart pacemakers, commercial electronic devices, military aircraft, aerospace electronics) due to short circuits and arcing. Metal whiskering has been observed in different metals such as Ag, Au,Sn,Zn,Cd, Cu,W, although the most studied whiskers arise from electroplated Sn and its alloys, which are the most common for electronic components. The mechanisms behind the whiskering effect have been largely studied since its discovery, and, presently, numerous solutions have been proposed, especially for Sn whisker formation. It should be pointed out that there is still no consensus in the scientific community in what regards the mechanisms underlying this phenomena in spite of the studies performed over the last 50 years. The main problem seems to be the very high number of factors having influence in the process. Nevertheless, at least for Sn, most authors agree that the driving force for whiskering is

related with the relaxation of compressive stress, which may arise from different sources: (i) internal stresses developed during coatings deposition; (ii) formation of intermetallic compounds due to the reaction with the substrate material (namely formation of Cu-Sn phases); (iii) oxidation reactions, enhanced by humidity, which among different factors can promote the formation of tin oxides. Despite some controversial discussions in scientific community, this mechanisms has been extended to explain other metals whiskering[51,52,53].

In the particular case of Ag, the NASA whisker group has reported the occurrence of this phenomena in primary current conductors of circuit breakers in switchgear at pulp recycling mill[54]. The studies related with Ag whiskers claim that the major factor behind Ag whiskering is related with environmental conditions, mainly to the presence of hydrogen sulfide (H_2S). Ag whiskering is, thus, attributed to the strong tendency of silver to corrode in H_2S environments with the consequent formation of Ag_2S. As soon as a thick enough layer of silver sulfide has been formed, metal filaments start to grow virtually everywhere but, more intensely, in the zones of higher temperature occurring while electrical units are energized[55,56]. Just in two months after previous cleaning, the whisker grew up to several inches (6-8 cm) long and up to 0.04 in (1 mm) thick (see figure 9). This phenomena was observed in Ag plated copper, being found that most of the whiskers are made of silver with 1-3 % of copper.

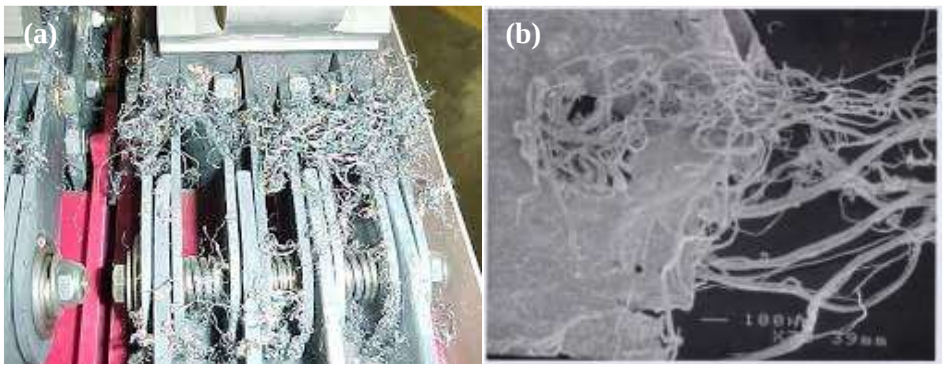

Figure 9 - (a) Ag whiskers in circuit breakers after failure (b) SEM micrograph of Ag whiskers[55]

References

[1] Donnet C. and Erdemir A., in *Tribology of Diamond-like carbon films*, Springer, New York, 2008.

[2] J.Robertson, *Diamond-like amorphous carbon*, Materials Science and Engineering R, 37 (2002) 129-281.

[3] W.Jacob and W.Moller, *On the structure of thin hydrocarbon films*, Applied Physic Letters, 63 (1993) 1771.

[4] H. Biederman, Z. Chmel, A. Fejfar, M. Mišina, J. Pešička, *Temperature induced structural rearrangements of Ag/a-C:H composite films and their dc electrical conduction*, Vacuum, 40 (1990) 377-380.

[5] H. Biederman, I.Cermak, A. Fejfar and J. PeSiEka, Electronics, 76 (1994) 937.

[6] H. Biederman, P. Hlidek, J. PeSiEka, D. Slavinsk,V. Stundlia, *Deposition of composite metal/C:H films - the basic properties of Ag/C:H*, Vacuum, 47 (1996) 1385-1389.

[7] R.J. Narayan. H. Wang, A. Tiwari, *Nanostructured DLC-Ag composites for biomedical applications*, Materials Research Society Symposium, 750 (2003) 205-210.

[8] Ag-C phase diagram, SGTE-SGTE Alloy Phase Diagrams, Accessed in March 2014, Available online: http://www.crct.polymtl.ca/fact/phase

[9] H. W. Choi, J.H. Choi, K.R. Lee, J.P. Ahn , K. H. Oh, *Structure and mechanical properties of Ag-incorporated DLC films prepared by a hybrid ion beam deposition system*, Thin Solid Films, 516 (2007) 248 – 251.

[10] G. Matenoglou, G.A. Evangelakis, C. Kosmidis, S. FouliasD. Papadimitriou, P. Patsalas, *Pulsed laser deposition of amorphous carbon/silver nanocomposites*, Applied Surface Science, 253 (2007) 8155–8159.

[11] H.S. Zhang, J.L. Endrino, A. Anders, *Comparative surface and nano-tribological characteristics of nanocomposite diamond-like carbon thin films doped by silver*, Applied Surface Science, 255 (2008) 2551–2556.

[12] J.L. Endrino, R. Escobar Galindo, HS. Zhang, M. Allen, R. Gago, A. Espinosa, A. Anders, *Structure and properties of silver-containing a-C(H) films deposited by plasma immersion ion implantation*, Surface and Coatings Technology, 202 (2008) 3675 – 3682.

[13] A.A. Onoprienko, M.I. Danylenko, *Annealing effects in Ag-doped amorphous carbon films deposited by dc magnetron sputtering*, Surface and Coatings Technology, 206 (2012) 3450–3453.

[14] C. Wang, X. Yu, M. Hua, *Microstructure and mechanical properties of Ag-containing diamond-like carbon films in mid-frequency dual-magnetron sputtering*, Applied Surface Science, 256 (2009) 1431–1435.

[15] Y. Wu, J. Chen, H. Li, L. Ji ,Y. Ye, H. Zhou, *Preparation and properties of Ag/DLC nanocomposite film fabricated by unbalanced magnetron sputtering*, Applied Surface Science, 284 (2014) 165-170.

[16] V.Dhandapani, E. Thangavel, M. Arumugam, K. S. Shin, V. Veeraraghavan, S. Yau, C. Kim, D.-E. Kim, *Effect of Ag content on the microstructure, tribological and corrosion properties of amorphous carbon coatings on 316L SS*, Surface and Coatings Technology, 240 (2014) 128-136.

[17] M.L. Morrison, R.A. Buchanan, P.K. Liaw, C.J. Berry, R.L. Brigmon, L. Riester, H. Abernathy, C. Jin, R.J. Narayan, *Electrochemical and antimicrobial properties of diamond like carbon-metal composite films*, Diamond and Related Materials, 15 (2006) 138 – 146.

[18] K. Baba, R. Hatada, S. Flege, W. Ensinger, Y. Shibata, J. Nakashima, T. Sawase, T. Morimura, *Preparation and antibacterial properties of Ag-containing diamond-like carbon films prepared by a combination of magnetron sputtering and plasma source ion implantation*, Vacuum, 89 (2013) 179-184.

[19] H. W. Choi, R. H. Dauskardt, S.C. Lee, K.R. Lee, K. H. Oh, *Characteristic of silver doped DLC films on surface properties and protein adsorption*, Diamond and Related Materials, 17 (2008) 252 – 257.

[20] T. Tamulevicius, A. Tamuleviciene, D. Virganavicius, A. Vasiliauskas, V. Kopustinskas, Š. Meškinis, S. Tamulevicius, *Structuring of DLC:Ag nanocomposite thin films employing plasma chemical etching and ion sputtering*, Nuclear Instruments and Methods in Physics Research Section B: Beam Interactions with Materials and Atoms, 341 (2014) 1-6.

[21] Š. Meškinis, A. Vasiliauskas, K. Šlapikas, R. Gudaitis, M. Andrulevičius, A. Čiegis, G. Niaura, R. Kondrotas, S. Tamulevičius, *Bias effects on structure and piezoresistive properties of DLC:Ag thin films*, Surface and Coatings Technology, 255 (2014) 84-89.

[22] T. de los Arcos, P. Oelhafen, U. Aebi, A. Hefti, M. Duggelin, D. Mathys, R. Guggenheim, *Preparation and characterization of TiN–Ag nanocomposite films*, Vacuum, 67 (2002) 463–470.

[23] C.P. Mulligan, D. Gall, *CrN–Ag self-lubricating hard coatings*, Surface and Coatings Technology, 200 (2005) 1495 – 1500.

[24] V. S. K.Chakravadhanula, C. K.T. Hrkac, V. Zaporojtchenko, T.Strunskus, F. Faupel and L. Kienle, *Surface segregation in TiO_2-based nanocomposite thin films*, Nanotechnology, 23 (2012) 495701 (7pp).

[25] J.E. Krzanowski, J.L. Endrino, J.J. Nainaparampil, and J.S. Zabinski, *Composite Coatings Incorporating Solid Lubricant Phases*, Journal of Materials Engineering and Performance, 13(4) (2004) 439.

[26] S Calderon V , R Escobar Galindo , N Benito , C Palacio , A Cavaleiro, S Carvalho, *Ag^+ release inhibition from ZrCN–Ag coatings by surface agglomeration mechanism: structural characterization*, Journal of Physics D: Applied Physics, 46 (2013) 325303 (10pp).

[27] N K Manninen , R Escobar Galindo , N Benito , N M Figueiredo , A Cavaleiro, C Palacio, S Carvalho, *Ag–Ti(C, N)-based coatings for biomedical applications: influence of silver content on the structural properties*, Journal of Physics D: Appllied Physics, 44 (2011) 375501 (8pp).

[29] R. Escobar Galindo, N. K. Manninen, C. Palacio, S. Carvalho, *Advanced surface characterization of silver nanocluster segregation in Ag – TiCN bioactive coatings by RBS, GDOES, and ARXPS*, Analytical and Bioanalytical Chemistry, (2013) 405:6259 – 6269.

[30] J. Xiong, M. Z. Ghori, B. Henkel, T. Strunskus, U. Schurmann, L. Kienle , F. Faupel, *Controlling surface segregation of reactively sputtered Ag/TiO_x nanocomposites*, Acta Materialia, 74 (2014) 1–8.

[31] A.A. Voevodin, C. Muratore, S.M. Aouadi, *Hard coatings with high temperature adaptive lubrication and contact thermal management: review*, Surface and Coatings Technology, 257 (2014) 247-265.

[32] J.J. Hu , C. Muratore, A.A. Voevodin, *Silver diffusion and high-temperature lubrication mechanisms of YSZ–Ag–Mo based nanocomposite coatings*, Composites Science and Technology, 67 (2007) 336–347.

[33] C. Muratore, J.J. Hu, A.A. Voevodin, *Adaptive nanocomposite coatings with a titanium nitride diffusion barrier mask for high-temperature tribological applications*, Thin Solid Films, 515 (2007) 3638 – 3643.

[34] C.P. Mulligan, D. Gall, *CrN–Ag self-lubricating hard coatings*, Surface and Coatings Technology, 200 (2005) 1495 – 1500.

[35] C.P. Mulligan, T.A. Blanchet, D. Gall, *CrN–Ag nanocomposite coatings: Effect of growth temperature on the microstructure*, Surface and Coatings Technology, 203 (2008) 584–587.

[36] C.P. Mulligan, T.A. Blanchet, D. Gall, *Control of lubricant transport by a CrN diffusion barrier layer during high-temperature sliding of a CrN–Ag composite coating*, Surface and Coatings Technology, 205 (2010) 1350–1355.

[37] C.P. Mulligan, T.A. Blanchet , D. Gall, *CrN–Ag nanocomposite coatings: High-temperature tribological response*, Wear, 269 (2010) 125–131.

[38] C.P. Mulligan, T.A. Blanchet, D. Gall, *CrN–Ag nanocomposite coatings: Tribology at room temperature and during a temperature ramp*, Surface and Coatings Technology, 204 (2010) 1388–1394.

[39] C.P. Mulligan, P.A. Papi, D. Gall, *Ag transport in CrN–Ag nanocomposite coatings*, Thin Solid Films, 510 (2012) 6774-6779.

[40] P.A. Papi, C.P. Mulligan, D. Gall, *CrN–Ag nanocomposite coatings: Control of lubricant transport by diffusion barriers*, Thin Solid Films, 524 (2012) 211-217.

[41] L. Sintubin, B De Gusseme, P. Van der Meeren, B. F. G. Pycke, W. Verstraete, N. Boon, *The antibacterial activity of biogenic silver and its mode of action*, Applied Microbiology and Biotechnology, 91 (2011)153 – 162.

[42] Z. Xiu,Q. Zhang, H. L. Puppala, V. L. Colvin, P. J. J. Alvarez, *Negligible Particle-Specific Antibacterial Activity of Silver Nanoparticles*, Nano Letters, 12 (2012) 4272-4275.

[43] S. Chernousova, M. Epple, *Silver as Antibacterial Agent: Ion, Nanoparticle, and Metal*, Angewandte Chemie International Edition, 52 (2013) 1636 – 1653.

[44] C N. Lok, C.M. Ho, R. Chen, Q.Y. He, W.Y. Yu, H. Sun, P. K. H. Tam, J.F. Chiu, C.M. Che, *Silver nanoparticles: partial oxidation and antibacterial activities*, Journal of Biological Inorganic Chemistry, 12 (2007) 527–534.

[45] G. A. Martınez-Castanon, N. Nino-Martınez, F. Martınez-Gutierrez, J. R. Martınez-Mendoza, F. Ruiz, *Synthesis and antibacterial activity of silver nanoparticles with different sizes*, Journal of Nanoparticle Research, 10 (2008) 1343–1348.

[46] G. A. Sotiriou, Sotiris E. Pratsinis, *Antibacterial Activity of Nanosilver Ions and Particles*, Environmental Science Technology, 44 (2010) 5649–5654.

[47] S.B.Sant, K.S.Grill, R.E.Burrel, *Nanostructure, dissolution and morphology characteristics of microcidal silver films deposited by magnetron sputtering*, Acta Biomaterialia, 3 (2007) 341-350.

[48] E.Unosson, D.Rodriguez, K.Welch, H.Engqvist, *Reactive combinatorial synthesis and characterization of a gradient Ag–Ti oxide thin film with antibacterial properties*, Acta Biomaterialia, 11 (2015) 503–510.

[49] P.J. Kelly, H. Li, P.S. Benson, K.A. Whitehead, J. Verran, R.D. Arnell, I. Iordanova, *Comparison of the tribological and antimicrobial properties of CrN/Ag, ZrN/Ag, TiN/Ag, and TiN/Cu nanocomposite coatings*, Surface and Coatings Technology, 205 (2010) 1606-1610.

[50] I.Carvalho, M.Henriques, J.C.Oliveira, C.F.Almeida,A.P.Piedade, S.Carvalho, *Influence of surface features on the adhesion of Staphylococcus epidermidis to Ag-TiCN thin films*, Science and Technology of Advanced Materials, 14 (2013) 035009.

[51] I. Ferreri, S. Calderon V., R. Escobar Galindo, C. Palacio, M. Henriques, A.P. Piedade, S. Carvalho, *Silver activation on thin films of Ag–ZrCN coatings for antimicrobial activity*, Materials Science and Engineering C, 55 (2015) 547-555.

[52] Crandall E. *Factor governing tin whisker growth – Springer Theses*, PhD thesis, s.l. Auburn University, 2013.

[53] E. Chason, N. Jadhav, F. Pei, E. Buchovecky, A. Bower, *Growth of whiskers from Sn surfaces: Driving forces and growth mechanisms*, Progress in Surface Science, 88 (2013) 103-131.

[54] Metal Whiskers, NASA Tin Whisker (and Other Metal Whisker) Homepage, Accessed in July 2015. Available online: http://nepp.nasa.gov/whisker/

[55] B.H. Chudnovsky, *Degradation of power contacts in industrial atmosphere: silver corrosion and whiskers*, Proceedings of the 48th IEEE Holm Conference on Electrical Contacts, 2002.

[56] M.A.Rivera, *Design considerations for reliable electrical, control and instrumentation systems in geothermal power plants with emphasis on hydrogen sulphide related problems*, Geothermal Training Programme, 20 (2007).

Chapter II

Experimental Details

This chapter is dedicated to the description of the experimental methodologies used in the thesis. The coatings are deposited following two different methodologies: magnetron sputtering and hybrid deposition method combining magnetron sputtering for amorphous carbon deposition and plasma gas condensation for Ag nanoparticles deposition. A summary of the theoretical background and fundamental concepts regarding both methodologies is given. The deposition system used in the work is described as well as the deposition conditions used for the preparation of the coatings analyzed in the preliminary work, presented in Chapter III. In the second part of this chapter the theoretical background and the experimental conditions used for the coatings characterization along the thesis are provided.

1. Coatings deposition

1.1 Magnetron sputtering

Sputtering represents one of the most popular physical vapor deposition (PVD) methods for thin films production, along with thermal evaporation, electron beam evaporation and laser ablation. PVD methods basically consist in the creation of vapor species from a target material with their subsequent condensation onto a substrate. In the sputtering process the atoms are ejected from the target through the collision of energetic ions, where the momentum transfer between the ions and the target material drives the process[1].

In a basic sputtering process a plasma is created by applying an electrical field to a neutral gas in a low vacuum environment. The electrical field causes the acceleration of charged particles, electrons and ions, the first ones ensuring the ionization of the neutral atoms of the discharge gas and the collision of the ions with the target material being responsible for the removal of target atoms and secondary electrons, which allow to sustain the plasma[1,2,3]. The necessary voltage for the creation of the plasma is known as the breakdown voltage (V_b), being found that at lower voltage values, ions do not acquire enough kinetic energy to create a charged particle (secondary electron). This voltage has been described by the Paschen law, where the dependence of V_b on the product "pressure times electrode spacing" is described[4].

Magnetron sputtering was developed in order to overcome some limitations inherent to dc diode discharge, thus allowing to increase the deposition rate, to reduce the target heating and to allow the plasma to be maintained at low operating pressures and voltages. This method basically consists in the use of magnets that create magnetic fields which are able to constrain the electrons motion in the target vicinity, increasing the electron-atoms collision probability and also the ion-target interaction[1,2].

The efficiency of a sputtering process is described by the sputtering yield, which measures the amount of atoms ejected per incident particle. The sputtering yield, derived by Sigmund´s theory, is given by:

$$S = \frac{3\varphi\alpha}{4\pi^2}\frac{4M_1M_2}{(M_1+M_2)^2}\frac{E_1}{E_2}\ for\ (E_1 < 1\ keV)$$

(2.1)

where M_1 refers to the mass of the discharge gas ion and M_2 the mass of the target atom, E_b is the surface binding energy, φ is a factor that is a measure of the efficiency of the momentum transfer in collisions. The E_1 is the energy of bombarding ion, which in the sputtering process is typically in the range from 50 eV to 1 keV [3,5].

The working gas typically used in the sputtering process is argon (Ar), due to either its inert nature, which means that it will not react with the deposited material, or the mass compatibility with most of the materials typically used in sputtering process, which allows to enhance the sputtering yield owing to the more efficient energy transfer [1,2,3].

1.2 Plasma gas condensation

Plasma gas condensation method, also designated as gas aggregation technique or inert gas condensation, represents a bottom-up approach for nanoparticles or clusters production. The technique is based on the formation of nanoparticles in the gas phase, which resembles the cloud or fog formation in nature, a process based on the condensation of atoms or molecules from supersaturated vapor in a noble gas atmosphere. The experimental setup consists in a vapor source inside a vacuum chamber, where the inert gas is introduced. The vapor source can be based on different approaches, which are used also in the PVD processes in thin film deposition. In this thesis, the vapor source is based on magnetron sputtering of a target material in a high pressure inert gas atmosphere (in this work Ar). One of the major advantages of this method is the possibility to tailor the particle size distribution and its easy combination with other different thin film production methods, allowing the deposition of nanocomposite coatings. This process is very similar to conventional magnetron sputtering; in the latter, the thin film grows from the sputtered atoms arriving to the substrate through the vapor phase while, in the plasma gas condensation, the nanoparticles are condensed in the cluster source, arriving to the substrate already in

solid state. The main difference between the two methods is the discharge pressure, which should be much higher in the latter case in order to allow the supersaturation to occur. It should be pointed out that the designation of plasma gas condensation is a particular case of inert gas condensation, where the term plasma is related with the clusters source method[6,7].

The clusters formation and growth occurs in three different stages:

i. Nucleation;
ii. Monomeric growth;
iii. Aggregation or coagulation.

The nucleation process is described by the classical nucleation theory, where homogeneous nucleation is considered in the formation of clusters in gas phase while heterogeneous nucleation occurs in the walls of the container. The first step involved in the clusters formation is a three body collision which is a necessary condition for dimer formation. The atom-atom recombination was postulated by Boltzmann in 1898, which is based on energy and momentum conservation. The process implies the formation of a metastable excited Ag_2* orbiting complex which is stabilized by a third atom (Ar) which carries away the excess internal energy of the dimer. After the formation of a stable nuclei the cluster continues to grow through the addition of single monomers. At a later stage of growth the number of monomers are almost vanished and, thus, the clusters continue to grow by coagulation or aggregation mechanisms, which involve two modes of growth: (i) collision of small clusters, with formation of quasi-spherical particles or (ii) growth via collision of large clusters, which results in fractal-like aggregates[6,7,8,9]. The different stages of clusters growth are schematically represented in figure 10, proposed by Mikhail Dutka[6].

The cluster diffusion and collisions between clusters in the initial stages are described by the kinetic theory of gases, which is valid when the mean free path of the clusters is large in relation to their own dimensions[2,8]. The mean free path is determined by the equation:

$$\lambda_m = \frac{RT}{\sqrt{2}N\sigma_{Ar}p} \tag{2.2}$$

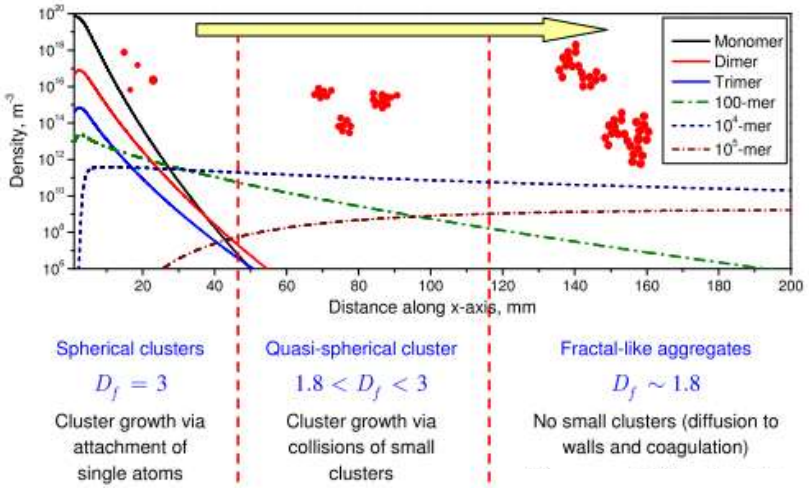

Figure 10 - Evolution of nanoclusters size distribution along the aggregation chamber (reference 6).

Where the pressure is considered to be similar to the Ar pressure since the density of Ar is much higher than the clusters density. The R is the Boltzmann constant, T the temperature, N the Avogadro´s number, σ_{Ar} the collision cross-section and p the pressure. Accordingly, the mean residence time (τ) can be calculated as:

$$\tau = \frac{pVN}{RT\phi} \tag{2.3}$$

At this stage, while the clusters grow they are heated by the binding energy delivered by the aggregating atoms, which in the case of a monomer growth represents the release of latent heat of condensation associated with the addition of new monomers. This energy is dissipated through collisions with inert gas and also through atomic rearrangements leading to the spherical shape of the small clusters. As the clusters become larger the energy delivered in the growth process is not enough for the complete coalescence or the sintering of the clusters. If the time of thermal sintering is larger than the mean time between successive collisions, the aggregates will grow as fractal shaped. The fractal structures show different collision rates even when the mass is equivalent to a spherical particle with the same number of atoms and, thus, their growth is not anymore described by the kinetic theory of gases, but instead by the Brownian model[6,8]. As can be depicted in figure 10 proposed by Mikhail Dutka[6] the

diffusion coefficient changes through the different stages of the clusters growth, being found that it is reduced as the particle size increases.

The main variables in this type of deposition systems are:

i. Gas flow rate, which will determine the clusters mean residence time,
ii. Pressure in the aggregation chamber, which will determine the collisions probability;
iii. Type of buffer gas;
iv. Current or power density applied to the target, which will determine the amount of sputtered metal atoms.

The increase in the gas flow rate will promote a decrease in the clusters mean residence time, thus reducing the clusters growth, while an increase in the aggregation chamber pressure will increase the collision probability, thus enhancing the growth rate[10,11,12]. It should be pointed out that these two variables are correlated; in general, the pressure in aggregation sources is increased by increasing the gas flow rate, which promote opposite effects in the clusters growth. Regarding the type of buffer gas, it will also influence the clusters final size, being found that, in general, He promotes the growth of smaller clusters owing to its higher drift velocity, which reduces the clusters residence time[10,11,12]. The current density will determine the amount of metal atoms ejected and, thus, the clusters size generally increases by increasing this parameter[11].

1.3 Deposition system

Two different deposition methods are involved for the production of either the Ag nanoparticles and/or the Ag/a-C nanocomposite coatings: plasma gas condensation (PGC) and magnetron sputtering (MS). Both methods are coupled in the same deposition system which is briefly described in this section.

The depositions are performed in a homemade equipment which is mainly composed by the deposition chamber, the vacuum pumps, the gas flow control and the electrical systems, everything connected to a control unit. A clusters source is connected to the main deposition chamber, allowing the co-deposition of sputtered coatings and nanoparticles. The deposition system is presented in figure 11.

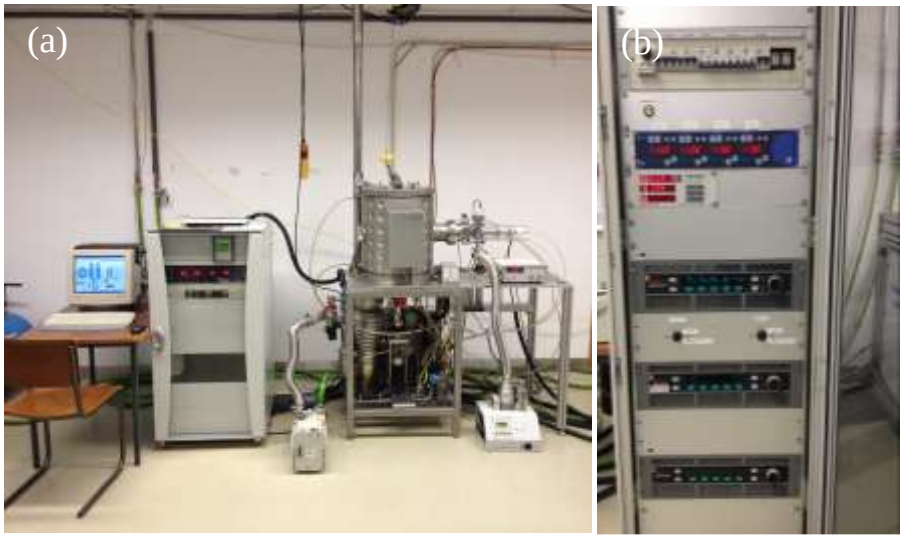

Figure 11 – (a) deposition system and (b) power sources

The deposition chamber is cylindrical with a diameter of about 40 cm and a height of 44 cm. The system can accommodate two parallel cathodes, supporting targets with dimensions of 20 cm x 10 cm, working in close field unbalanced magnetron mode. The substrate holder is placed in the center of the deposition chamber and can operate either in static or rotation mode, being the rotation speed possible to be adjusted. The substrate holder can also be electrically biased.

The vacuum system is composed by two vacuum pumps, which allow to achieve base pressures in the order of $5x10^{-4}$ Pa: a rotary vacuum pump (Pfeiffer DUO 20M, pumping speed 20 m^3/h) and a diffusion pump (BOC Edwards – Diffstak 160/700, pumping speed 760 l/s). The working gas - argon (Ar) - is introduced in the chamber through an Aera FC-7700 Series MFCS flowmeter. It should be pointed out that the deposition chamber is connected to three additional flowmeters, which allow to incorporate different gases in the deposition chamber, namely N_2, O_2 and CH_4. The system base pressure is monitored through a wide range pressure gauge (BOC Edwards – WRG-S, measurement range: from atmosphere to 10^{-9} mbar), while the deposition pressure is monitored by a Pirani pressure gauge (APG100-XLC measurement range: from atmosphere to 10^{-4} mbar). The pressure in the nanoclusters source is monitored through a BOC Edwards – WRG-S sensor.

The electrical system is mainly composed by 2 power supplies: (i) a pulsed DC power source (Advanced Energy Pinneacle Plus working with a maximum power of 5

kW) and a (ii) DC power supply (Advanced Energy Pinneacle Plus (2 x 6 kW)). The power supplies, as well as the different opening/closing of the valves and the gas feeds are computer controlled.

The deposition chamber also contains a shutter which allows to place SS316L shields in-between the targets and the substrate holder, which is used during the targets and substrates cleaning procedure. During the deposition, the shields are removed from the space between the targets and the substrate holder, thus allowing the coatings deposition.

The cluster source is a homemade system acquired from Charles University in Prague, Faculty of Mathematics and Physics. The cluster source (figure 12) is mounted aside to the main deposition chamber (figure 11) and it is separated from the main chamber by an exit orifice with a diameter of 2 mm. Neither differential pumping between the main chamber and the cluster source nor a mass filter are used.

Figure 12 - (a) Clusters source, (b) inside view of the clusters source and (c) conical nozzle

The cluster source walls are cooled by water as well as the magnetron head. As can be seen in figure 12 (b) and (c) the cluster source has two parts: a cylindrical chamber and a conical nozzle, which dimensions (diameter, Ø and height, h) are presented in Table 1. The exit orifice has a diameter of 2 mm and a cylindrical shape in the last 2 mm, in order to inhibit the effects of aerodynamic focusing.

Table 1 - Clusters source main dimension (Ø, diameter and h, height)

Component	Dimension (mm)
Exit Orifice (Ø)	2
Interior of Cluster Source (Ø)	62
Cylindrical Part (h)	55
Conical Part (h)	31
Target (Ø)	50
Distance target exit orifice	86

The working gas (Ar) is introduced in the deposition system through the clusters source; thus, the pressure inside the clusters source and the main deposition chamber cannot be controlled independently.

1.4 Preliminary depositions

Deposition of Ag/a-C nanocomposite coatings by magnetron sputtering

In a first approach, Ag/a-C nanocomposite coatings are deposited using one pure carbon target (99.99%) inserted with varying number of Ag pellets, in order to vary the amount of Ag in the carbon coatings, and a Ti target (99.99%) for depositing an adhesion enhancement interlayer. All the target materials were acquired in Testbourne Ltd. The coatings are deposited by dc magnetron sputtering in Ar atmosphere with substrates rotating at 17 cm from the target at a constant speed of 18 rpm. The base pressure in the deposition chamber is approximately 5×10^{-4} Pa and rose up to values of approximately 5×10^{-1} Pa for the deposition. During deposition, the substrate holder is connected to the pulsed dc power supply and a bias voltage of -50 V is applied, being the reverse time and frequency 0.5 μs and 250 kHz, respectively. The coatings deposition parameters, Ag/C relative erosion area and power density applied to C target (J_C), are summarized in Table 2. The coatings were labeled as a-C (Ag-free amorphous carbon coating) and as Ag_x, where x represents the Ag content in the coating. The deposition time is adjusted in order to achieve similar thicknesses in all coatings.

Table 2 - Deposition conditions used in the Ag/a-C nanocomposite coatings deposition in the preliminary work

Coating	Erosion Area Ratio (Ag/C)	J_C (W/cm^2)
a-C	0	
Ag1	0.01	
Ag4	0.03	7.5
Ag6	0.06	
Ag13	0.11	

In order to remove the contamination from the targets, a sputter cleaning procedure is performed before each deposition and, simultaneously, the substrates are also sputter etched. During this stage the shutter shield is placed between the target and the substrate holder in order to avoid cross contamination. The power density applied to C and Ti targets is 1.75 W/cm^2 and 0.25 W/cm^2, respectively. The substrate holder is connected to a pulsed dc power supply being the voltage fixed at 500 V; the reverse time and frequency were 1.6 μs and 250 kHz, resulting in a reverse phase of 40 %. The total etching time is 45 minutes. In order to further improve the coatings adhesion to the substrate, an adhesion interlayer consisting of a Ti/TiN/TiCN multilayer with a total thickness of 450 nm was previously deposited. The Ti target is first sputtered with a target power density of 10 W/cm^2 in pure Ar atmosphere, during 5 minutes; then, nitrogen is introduced (17 sccm) during 15 minutes, to deposit the TiN layer and, lastly, the power of the graphite target was gradually increased from 0 up to 7.5 W/cm^2, during 5 minutes.

The substrates used in this stage are: tool steel (used for tribological tests), stainless steel (determination of the residual stress and XRD analysis) and silicon (nanoindentation tests). Previously to the deposition process, the steel substrates are polished and all substrates were ultrasonically cleaned in acetone, ethanol and distilled water, for 10 minutes in each medium.

Deposition of Ag nanoparticles

In this stage different samples are deposited in order to evaluate: (i) the influence of deposition parameters on the Ag nanoparticles size distribution, (ii) the evolution of

Ag-NP´s size distribution with the amount of deposited Ag nanoparticles, (iii) the chemical composition and structure of Ag films and (iv) the uniformity of Ag nanoparticles distribution in Ag/a-C nanocomposite coatings deposited by hybrid process (MS+PGC).

Two series of samples are prepared in order to evaluate the effect of (i) current density applied to Ag (J_{Ag}) target and (ii) Ar flow, on the clusters size distribution. In the first series the Ar flow is varied in the range [10 – 40] sccm (with a step of 10 sccm), while the current density is fixed at 7.6 mA/cm^2. The variation in the Ar flow results in different pressures inside the cluster source and also in the main deposition chamber. In the second series the J_{Ag} was varied in the range [7.6 -22.9] mA/cm^2, while the Ar flow was fixed at 40 sccm. The deposition times are adjusted for each deposition parameter in order to deposit individual NP, being the deposition time in the order of just a few seconds in all depositions. The substrate holder is placed at 25 cm away from the cluster source exit, where transmission electron microscopy (TEM) grids with carbon foils are placed aligned with the cluster source exit. No substrate heating or bias polarization is applied neither previous to the clusters deposition nor during the deposition process, in order to avoid the substrate damage. The depositions are performed with the substrate holder in static mode. It should be pointed out that each series are deposited in the same deposition run. Each carbon grid is placed in one face of the substrate holder and, after the deposition of each sample, the substrate holder is rotated in order to locate a new substrate in front of the clusters source, prepared for another set of conditions. Previously to the deposition of a new sample the plasma is stabilized during approximately 3 minutes. The deposition parameters are summarized in Table 3.

In order to evaluate the NP growth mechanism along time, Ag-NP´s are deposited with an Ar flow of 30 sccm and J_{Ag} of 7.6 mA/cm^2 with three different deposition times (0.5 s 1 min, 3 min) in static mode. As previously, each carbon grid is placed in one face of the substrate holder and after the deposition of each sample the substrate holder is rotated in order to locate the new substrate in front of the clusters source. In order to perform EDS and XRD analysis, a thicker coating is deposited in a silicon substrate with a deposition time of 8 min., J_{Ag} = 7.6mA/cm^2 and argon flow of 40 sccm.

Table 3 - Deposition parameters used for the deposition of Ag nanoparticles by the plasma gas condensation method

	Ar Flow (sccm)	J_{Ag} (mA/cm^2)	Pressure in Deposition Chamber (Pa)	Pressure in Cluster Source (Pa)
1st Series	10	7.6	5.9×10^{-2}	187
	20		1.9×10^{-1}	320
	30		3.0×10^{-1}	459
	40		$4.4.\times10^{-1}$	595
2nd Series	40	7.6	4.4×10^{-1}	595
		11.7		
		17.8		
		22.9		

Deposition of Ag/a-C nanocomposite by hybrid method (PGC+MS)

Ag/a-C nanocomposite coatings are deposited by a combination of magnetron sputtering for the carbon deposition and plasma gas condensation for the Ag nanoparticle deposition. A pure carbon target is placed in the main deposition chamber, while a silver target is placed in the cluster source. The substrate holder is placed at 10 cm from the carbon target and 25 cm from the cluster source exit, being the rotation speed 18 rpm. The base pressure in the main deposition chamber is approximately 5×10^{-4} Pa and rose up to values of approximately 5×10^{-1} Pa in the main chamber and 595 Pa in the clusters source, during the deposition process. During deposition, the substrate holder is connected to the pulsed dc power supply and a bias voltage of -50 V is applied, being the reverse time and frequency 0.5 μs and 250 kHz, respectively. The deposition time is set to 165 min, which allows the deposition of a coating with about 1 μm.

The sputter etching process and sample preparation is similar to the procedure used for Ag/a-C coatings deposited by magnetron sputtering.

Two silicon substrates are placed in the substrate holder at a distance of about 3 cm (in vertical direction), being one of them placed in front of the cluster source nozzle. The coatings are analyzed through SEM/EDS analysis in order to determine the deposition uniformity along vertical direction.

2. Coatings characterization

2.1 Chemical composition

Electron-Probe X-ray Microanalysis (EPMA)

Electron probe X-ray microanalysis (EPMA) is an elemental analysis characterization technique widely used in thin films characterization. An electron beam is focused on the sample and, then, the characteristic X-rays emitted by the sample are analyzed by an energy dispersive spectrometer (EDS) and wavelength dispersive spectrometer (WDS); the later one allows to obtain a more accurate quantitative analysis.

The chemical composition of Ag/a-C nanocomposite coatings is accessed by EPMA in a Cameca SX-50 apparatus operating at 10 keV. The chemical elements are analyzed in the wavelength dispersive spectrometry (WDS) mode. Five punctual measurements are performed in each sample. The measured intensities are compared with standard ones and the elemental concentrations were calculated after applying a ZAF (Z=atomic number correction, A=Absorption correction and F= Fluorescence correction) correction to the experimental results.

The depth of analysis (R) is easily determined by using Kanay-Okayama equation given by:

$$R = \frac{0.0276AE^{1.67}}{(Z^{0.89}\rho)} \qquad (2.4)$$

where A is the atomic weight (for carbon 12 g/mol), E the beam energy in keV, Z the atomic number (6 for C) and ρ the density (about 1.8-2.2 g/cm^3 for amorphous carbon). The depth of penetration for a beam with energy of 10 keV is between 1.4 μm to 1.6 μm for pure carbon coatings. Obviously, the incorporation of a heavier element (Ag) will decrease the depth of analysis. Due to the high depth of penetration, the chemical analysis is only performed in coatings with a thickness of about 1 μm[13].

X-Ray Photoelectron Spectroscopy (XPS)

X-ray photoelectron spectroscopy is a chemical characterization technique that allows to obtain information about surface chemical composition and, also, about the atomic bonding state. In this technique the sample is analyzed with X-rays. From the conceptual point of view, the technique is based on the photoelectric effect. The kinetic energy of photoelectrons (KE) emitted by the sample are analyzed and aftermost their binding energy (E_B) can be calculated according to the following equation:

$$KE = E_{X-ray} - E_B - \psi \tag{2.5}$$

where $E_{X\text{-}ray}$ and ψ represents the energy of incident radiation and spectrometer work function, respectively.

Only the electrons created in a depth called escape depth, given by $\lambda_a \cos\theta_n$, are able to escape from the sample and contribute to the XPS spectrum. The depth of analysis depends on the attenuation length (λ_a), which shows values ranging from 0.5 to 2.5 nm, and also on the angle of emission with respect to the surface normal, θ_n. These values allow to explore the extreme surface sensitivity of this technique. Since the core electron binding energies are sensitive to the atom´s chemical state, information about materials bonding state can also be obtained[13,14,15].

The XPS analysis is performed in a hemispherical analyzer (SPECS EA-10 Plus).The pass energy was 15 eV giving a constant resolution of 0.9 eV. The C line at 284.8 eV is used in order to calibrate the binding energies. A twin anode (Mg and Al) X-ray source is operated at a constant power of 300 W using AlKα radiation. The samples are sputter-cleaned *in situ* using a broad 3 keV Ar^+ beam for 10 min.

Glow Discharge Optical Emission Spectroscopy (GDOES)

In glow discharge optical emission spectroscopy (GDOES) the sample atoms are sputtered by Ar ions and aftermost the atoms are excited by the plasma and de-excited by emitting photons with characteristic wavelength, which allows to identify and quantify the materials chemical composition. This technique is relatively new and it has been

widely used as depth-profiling technique due to its good depth resolution and fast analysis (in order of few seconds) when compared with other depth-profile techniques such as XPS. The depth resolution is about 2 nm in the surface and degrades gradually due to the surface roughening and layers partial mixing promoted by the sputtering process[15,16].

GDOES is performed in a Horiba Jobin Yvon RF GD Profiler equipped with a 4-mm diameter copper anode, operating at radiofrequency discharge pressure of 650 Pa (in argon atmosphere) and a power of 40 W.

Inductively Coupled Plasma-Optical Emission Spectroscopy (ICP-OES)

Inductively coupled plasma-optical emission spectroscopy (ICP-OES) is a technique used in the chemical analysis of liquid samples or solids dissolved in liquids. The main advantage of this technique is the low detection limit (in range of ppb to ppm) and possibility to perform a fast analysis of numerous elements. The technique is based on the analysis of the characteristic wavelength emitted by the atoms and ions present in the plasma, which allows the element identification. The quantification is performed by comparing the emission intensities of the samples and standards. In the plasma the sample is vaporized and the chemical bonds are broken resulting in free atoms and ions. Most of the elements exist as singly charged ions in the plasma and, thus, the spectral lines from ions are more intense[13].

Silver ion release is analyzed using an ICP-OES spectrometer PERKIN ELMER OPTIMA 8000. SS316L coated samples with 4 cm^2 are immersed into a 50 ml vessel, containing 50 ml of 0.9% NaCl at room temperature. 2 ml of the solution are taken out after 0, 2, 6, 12, 24, 168 and 720 hours of immersion and reserved for ICP-OES in dark, to avoid silver precipitation. Two calibration curves are prepared using a silver standard solution for ICP (silver, plasma standard solution, specpure, Ag 1000 ppm), diluted in HNO_3 at 5% v/v in order to mimic the standard solution matrix or NaCl 0.9 % w/v to replicate the experimental conditions used for the samples. Both calibration curves showed indistinguishable results. At least 3 samples are evaluated and the standard deviation are presented.

2.2 Morphological characterization

Transmission Electron Microscopy (TEM)

Transmission electron microscopy (TEM) is an electron microscopy technique that allows to obtain information about morphology and structure of different types of materials (e.g. ceramics, polymers, metals, biological samples, etc). The first TEM was built in 1931 by Knoll and Ruska and ever since this technique has been subjected to great developments prompted by the high spatial and analytical resolution, which has revolutionized our understanding about matter own to the possibility to observe it at an atomic level[17].

In TEM an electron beam passes through a thin specimen and an image is formed from the interaction of electrons and the specimen. The image is then magnified and focused onto an imaging device. The electrons interact with the specimen in different ways as they pass through it: they can be scattered or remain unaffected. The non-uniform distribution of the electron beam that merges from the specimen surface contains all the information about the specimen, and the different types of interaction can be used to obtain different type of information. The TEM images are generally classified according to the type of contrast: (i) mass-thickness contrast, (ii) diffraction contrast and (iii) phase contrast. In the present thesis two types of images were recorded: (i) bright field (BF) imaging using diffraction contrast and (ii) high resolution (HRTEM) imaging based on phase contrast. The diffraction contrast is controlled by the crystalline structure of the material and specimen orientation according to the Bragg´s law being the interaction between the specimen and the electron beam classified as coherent elastic scattering, which is related with the particle like behavior of the electrons. Generally the diffraction contrast images can be bright field (BF) or dark-field (DF) image; in BF mode the direct beam is selected to form the image while in DF the diffracted one is selected with the objective aperture. In phase contrast imaging the information is built through the changes on the electrons phase, which are related with their wave like characteristics. In this imaging mode a recombination of various beams is used and the resulting interference pattern is observed[17].

The coatings are analyzed in three different equipment's: TEM (Tecnai G2) (University of Coimbra), JEOL 2010F (Texas Materials Institute) and TEM TECNAI G2 F30 X-TWIN (Microelectronics Research Center, the University of Texas at Austin).

Specimen preparation

In the present thesis two types of samples were observed in TEM: (i) Ag-NP´s coated TEM grids with carbon foil and (ii) Ag/a-C nanocomposite coatings with a thickness of 750 nm. In the case (i) no previous specimen preparation is required while in case (ii) the polymer coated Ag/a-C coatings were prepared by ultra-microtomy. In this technique the samples are cut into very thin slices, with a thickness of about 60 nm. Previous to the cutting the sample is immersed in an epoxy and cured during 24 hours in an owen at 70°C. In ultramicrotome the specimen is moved past a knife blade, which is made of diamond. The knife is immersed in a water container where the samples will be collected into a TEM grid.

Scanning Electron Microscopy (SEM)

Scanning electron microscopy (SEM) is an electron microscopy technique which allows to obtain information about the surface morphology, topography and chemical composition. The technique is based on scanning the samples surface with a focused electron beam. Numerous types of interactions occur when the electrons interact with the sample, being the most relevant ones in SEM the elastic interactions with atomic electrons, which lead to the emission of secondary electrons (SE), and the elastic collision with atomic nucleus, which lead to the emission of backscattered electrons (BSE). The SE electrons result from the energy transfer between the electron beam and the specimen electrons, thus, the energy of emitted SE electron is much lower than the beam energy. In fact, these energy losses limit the depth from which the electrons are emitted to the detector, thus, the information obtained with SE is related with the first ten of nanometers in the samples surface. These electrons are usually used to achieve topographical information. The BSE electrons result from elastic collision with samples nuclei, thus, these electrons generally possess an energy comparable to the beam energy.

The BSE´s allow to obtain morphological analysis and also to obtain information about the phase composition, since the atoms with higher mass will scatter the electrons more strongly, thus, the regions of higher atomic mass will appear brighter in the micrographs. The BSE electrons generate information from a high depth, which depends mainly on the primary beam energy.

The coatings are analyzed in three different equipment's: NanoSEM - FEI Nova 200 (FEG/SEM) equipped with a EDAX - Pegasus X4M (EDS/EBSD) detector (SEMAT-Universidade do Minho); Hitachi S-5500 (UT Austin) and ZEISS MERLIN Compact/VPCompact, Field emission scanning electron microscope (FDSEM) (IPN).

Atomic Force Microscopy (AFM)

Atomic force microscopy is used to evaluate the surface topography by using a sharp solid force probe, which measures the surface height. This analysis allows to determine the surface roughness and topography at nanoscale level.

AFM is performed in a Bruker Innova apparatus equipped with a silicon probe working in tapping mode. Five measurements are performed in the sample surface in order to evaluate the average roughness (Ra).

2.3 Structural characterization

X-Ray Diffraction (XRD)

Among different characterization techniques used for the evaluation of thin films structure, X-ray diffraction is one of the most powerful ones and, thus, is the most largely used. This technique is nondestructive and does not require previous specimen preparation, allowing to identify the crystalline phases present in the coatings as well as the texture evolution. Moreover, the line broadening in XRD patterns allows to determine the crystallite size and, in specific conditions, to access information about any distortion of the crystal structure, such as microstrains, dislocations, twin planes and stacking faults. In conventional symmetric $\theta/2\theta$ configuration, the path travelled by X-rays in the sample is too short for typical Bragg angles to deliver X-ray reflections with

acceptable peak to noise ratio, moreover, the penetration depths of X-rays are generally in micrometer range, which means that most of the information obtained in the diffractogram stems from the substrate. In order to overcome these drawbacks new X-ray diffraction techniques have been developed where the primary beam enters the sample at very small incidence angles, thus allowing to increase the signal coming from the thin film surface. Among them, grazing incidence X-ray diffraction (GIXRD) is widely used for thin film analysis, since it allows to overcome the drawbacks of conventional $\theta/2\theta$ configuration; moreover, this technique allows to obtain depth resolved information through the variation of incidence angle[18].

In GIXRD a parallel monochromatic X-ray beam impinges on the surface at a fixed incidence angle (α), with a value close to the critical angle for total external reflection, α_c, while the detector is rotated on a goniometer circle. The incident wave vector (K_o), exit wave vector (K_f) and surface normal lie all in the same plane, thus, the technique belongs to coplanar configuration. The scattering angle (2θ) is the angle between exit beam and elongation of the incident beam (see figure 13).

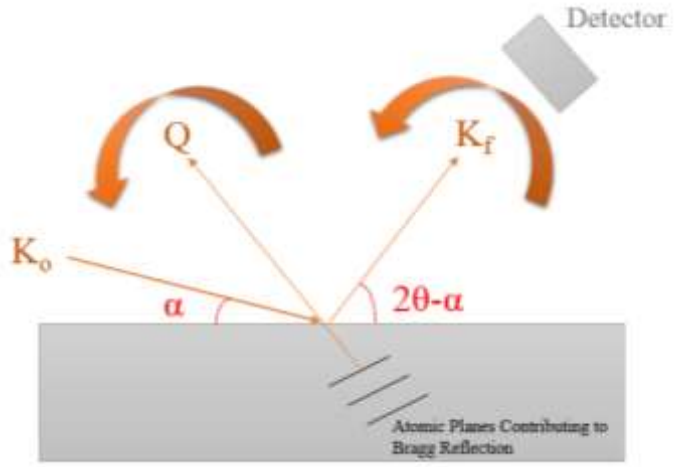

Figure 13 - Schematic representation of GIXRD analysis

For the energies usually utilized in X-ray diffraction, the index of refraction n of most materials is smaller than unity and it can be described as:

$$n = 1 - \delta - i\delta' \tag{2.6}$$

where δ and δ' represent the real and imaginary part of the dielectric susceptibility, which are given by:

$$\delta = \frac{Nre}{2\pi}\frac{Z}{A}\rho\lambda^2 \tag{2.7}$$

and

$$\delta' = \frac{\mu\lambda}{4\pi} \tag{2.8}$$

where N is Avogadro´s number, r_e is the classical electron radius, Z is the average atomic number, A is the average atomic mass, ρ is the mass density, μ is the linear absorption coefficient and λ the X-ray wavelength. The critical angle for total external reflection is given by Snell´s law and its value can be determined according to equation 2.9, if no absorption effects are considered.

$$\alpha_c = \sqrt{2\delta} \tag{2.9}$$

The X-rays penetration depth generally shows three different zones, which are determined by the critical angle: at $\alpha<\alpha_c$ total external reflection occurs and the X-rays propagate in the surface, being the penetration depth nearly constant, above $\alpha>\alpha_c$ the penetration depth increases sharply until absorption limited regime is achieved, above which the penetration depth increases at a slower rate for increasing incidence angle values.

The XRD line profile is a convolution of the instrumental and physical factors (crystallite size and microstrain); thus, in order to calculate those the experimental profiles must be corrected. The experimental profile can be fitted with a convolution of the instrumental and specimen functions. Different functions have been used for representing both the instrumental and physical parameters, namely Gaussian, Cauchy, Split Pearson and pseudo-Voigt. After correcting the instrumental broadening, the physical parameters can be extracted. In 1918 Scherrer[19] derived a formula for

determining the crystallite size through Bragg reflection width, which is presently widely used, and given by:

$$D_g = \frac{K\lambda}{B\cos\theta} \tag{2.10}$$

Where K is the Scherrer constant, which value is close to unity, λ the wavelength of the X-ray radiation, β is the FWHM entered in radians and θ is the Bragg angle of (hkl) reflection. The strain broadening caused by the displacement of the atoms from their reference lattice positions can be determined according to Williamson and Hall model or Warren and Averbach method, however, the use of these methods requires the analysis of line broadening from different reflections. In case of nanocrystalline thin films, generally the higher order reflections are too weak to be measured and, thus, the strain broadening is difficult to determine[18].

The XRD analysis is performed in a Philips X'Pert diffractometer, operating with CoKα radiation in grazing incidence mode with an angle of 2°. The GIXRD analysis is performed in ANalytical X´Pert PRO MPD diffractometer operating with CuKα, and the incidence angle is varied in the range from 0 to 0.8°, in order to evaluate the Ag size distribution across the coatings depth.

2.4 Mechanical and tribological characterization

Residual Stress

The total stress developed in a coating results from the sum of the thermal stress, which arises from the difference in the thermal expansion coefficient of the coating and the substrate, and the intrinsic stress, which results from the thin film growth process. In the particular case of amorphous carbon coatings, intrinsic stress is related with ion peening (energetic particle bombardment during film growth). Generally, the deposition of ceramic-type materials onto metallic substrates under energetic conditions leads to the development of compressive residual stresses which, in sputtered coatings, are very often in the order of some GPa. The presence of compressive residual stress causes the substrate bending (convex outward)[20].

The coatings residual stress can be determined from experimental measurements of the substrate deflection before and after coating and posterior application of the Stoney equation. The equation is given by:

$$\sigma = \frac{E_s}{1-\upsilon_s}\frac{t_s^2}{6t_c}\left(\frac{1}{r_c}-\frac{1}{r_{uc}}\right)$$

(2.11)

E_s, υ_s are the substrate elastic modulus and Poisson coefficient, t_s, t_c are the substrate and coating´s thickness, and r_c, r_{uc} the radius of curvature of coated and uncoated substrate, respectively. The substrates curvature radius can be determined by simulating the substrate profile before and after deposition using a second order polynomial function:

$$y(x) = a + bx + cx^2$$

(2.12)

Where y(x) is the substrate deflection along z direction. The radius of curvature is given by:

$$r = -\frac{1}{2c}$$

(2.13)

The substrates curvature radii are measured before and after deposition by measuring the substrate (stainless steel, diameter of 25 mm and thickness of 0.5 mm) profile in a high precision laser displacement meter (Perthometer S2 Perthometer) along two different directions[1,20,21].

Hardness

The coatings hardness is determined through depth indentation technique (nanoindentation). The technique is based on pressing a hard tip into the coating with a controlled load, which allows to determine the coatings hardness based on the

penetration depth. The coatings hardness is determined by the ratio of maximum applied load (P_{max}) divided by the displacement area[22].

The coting hardness are determined in a MicroMaterialsNano Test apparatus, which operates with a Berkovich indentor. In order to obtain a statistical analysis, 32 measurements are performed in each coating, in two different areas. The applied load is set to 5 mN in order to avoid the substrate influence.

Tribological performance

The coatings tribological properties (wear rate and friction coefficient) are determined in a pin-on-disk tribometer. A sample is positioned in a planar support which rotates around a single axis being the counterpart (usually with spherical geometry) mounted on a lever in contact with the sample´s surface. A controlled normal load is applied over the counterpart. The friction coefficient (μ) is determined by measuring the lever horizontal force, which is given by the ratio of frictional force (F_a) and normal load (F).

The coatings friction coefficient and wear rate depend on the contact pressure (Hertz stress) which depends on several parameters, such as, the applied normal load, the counterpart material and the pin geometry. In the particular case of two elastic spheres pressed in contact with a force F, the resultant circular contact area has a radius given by:

$$a = \left(\frac{3FR}{4E^*}\right)^{1/3} \tag{2.14}$$

being the reduced radius of curvature (R) similar to the counterpart radius since the sample is a plane surface with infinite radius. The term E* is the reduced contact modulus given by:

$$\frac{1}{E^*} = \frac{1-\nu_1^2}{E_1} + \frac{1-\nu_2^2}{E_2}$$

(2.15)

The maximum (p_0) and mean (p_m) Hertzian contact pressures are given by:

$$p_{o=}\frac{3}{2}p_m = \frac{3P}{2\pi a^2}$$

(2.16)

The coatings or counterpart wear rate can be determined according to the following equation:

$$k = \frac{V}{s.F}\left[\frac{mm^3}{N.m}\right]$$

(2.17)

Where V is the worn volume, s the total sliding distance and F the normal load. The worn volume is calculated through the measurement of four different cross-sections in the worn area by three dimensional optical profilometry, which allows to determine the average cross-sectional area. After, this value is multiplied by the length of the wear track. The total sliding distance is given by the perimeter of the wear track multiplied by the number of cycles in test[22,23,24].

The tribological tests shown in Chapter III are performed in Czech Technical University in Prague, in a CSM tribometer, while the tests performed in Chapter VI are performed in CEMUC in a home made tribometer. The main testing parameters used in both Chapters are summarized in Table 4. In order to obtain a statistical analysis, three tests were performed per sample. Circular samples with a diameter of 10 cm were used in the pi-on-disk tests.

In order to perform the tribological tests in simulated body fluids, an aluminum container is used, which was covered with a resin in order to avoid the release of aluminum corrosion products to the biological fluids.

Table 4 - Test conditions used in pin-on-disk

	Chapter III	**Chapter VI**
Equipment	CSM Tribometer	Home made
Counterpart	Zirconia	Alumina
Ball Diameter (mm)	6;10	10
Applied Load (N)	10;18	1
Pm (MPa)	690;1180	450
Linear speed (cm/s)	10	10
Number of Laps	20000	10000
Test Conditions	Dry at 25°C	Dry at 37°C
		HBSS* at 37°C
		HBSS+BSA** at 37°C

*Hank´s Balanced Solution
**Bovine Serum Albumin

2.5 Open Circuit Potential (OCP)

The electrochemical reactions involve the presence of an anodic reaction (electron producing reaction) and a cathodic reaction (electron consuming reaction). Each of these reactions are characterized by a specific Gibbs free energy which allow to predict the tendency for the metal to be oxidized or reduced. Let us assume a simple reduction reaction described by the following equation:

$$O + n\text{è} \Leftrightarrow R$$

(2.18)

Where O is the oxidized specie, R the reduced one and n the number of exchanged electrons, è. The relationship between the concentrations of reduced species [R], oxidized species [O] and Gibbs free energy ΔG is given by:

$$\Delta G = \Delta G° + RTln\frac{[R]}{[O]}$$

(2.19)

The Gibbs free energy is not a measurable property, however, one can experimentally measure the electrical potential and relate it with the Gibbs free energy through the Faraday´s Law:

$$\Delta G = (-nF_c)E \tag{2.20}$$

Where E is the electrical potential measured in volts and F_c the charge transported by one mol of electrons (96.494 C/mol). The E value is known as open circuit potential (OCP), which is measured when no external current or voltage passes through the electrochemical cell. The mathematical expression describing the correlation between potential and concentration for a cell reaction is known as the Nernst equation given by:

$$E = E^{\circ} + \frac{RT}{nF} ln \frac{[O]}{[R]} \tag{2.21}$$

It should be pointed out that in case of spontaneous reaction $\Delta G<0$ and thus the $E>0$, which means that all materials with positive OCP tend to be spontaneously reduced (act as electron acceptors). The measurement of OCP value allows to predict and compare different materials in relation to their tendency to be corroded. This analysis is the faster and easiest to interpret among different electrochemical measurements giving a good insight about the electrochemical behavior of different materials[25].

The analyses are performed with a saturated calomel (SCE) as reference electrode in 0.9 %NaCl solution.

2.6 Antibacterial performance

The antibacterial tests were performed in CEB, Center for Biological Engineering, LIBRO – Laboratório de Biofilmes Rosário Oliveira, University of Minho, by Dr. Isabel Carvalho.

The coatings antibacterial activity is tested against *Staphylococcus epidermidis* (*S. epidermidis*, IE186 strain, a clinical isolate belonging to the CEB Biofilm Group collection). Zone of inhibition (ZoI) tests, adapted from Kirby-Bauer test[26], are carried out to determine the diffusion of silver from the coatings surface. The halo size is used as a qualitative measure of the sample activity. *S. epidermidis* is stored at − 80 ^{0}C in Tryptic Soy Broth (TSB, Merck) containing 15% (vol/vol) glycerol. Cells were firstly grown for approximately 36 h in plates of Tryptic Soy Agar (TSA, Merck), and, then, incubated for 18 h in TSB, at 37 ^{0}C, under a constant agitation of 120 rpm. Afterwards, the resultant cell suspension was adjusted to an optical density (OD) of 1.0 at 640 nm and properly diluted in TSB to 1 x 10^{7} CFU.ml^{-1}. The incubation of the bacteria in the agar is performed with the addition of 1 ml of cells suspension to 14 ml of cooled (< 50 °C) Tryptic Soy Agar (TSA, Merck) and placed into sterile plastic petri dishes. After medium solidification, the coated coupon (previously sterilized by exposure of ± 1 h to UV light) are placed separately on the top of an agar plate, with the coated side in contact with the agar, and incubated for 24 h, at 37 °C. After the incubation period, the halo (zone of transparent medium, which means that there is no bacteria growth) formed around the sample was measured and photographed to record the results (images captured with Image Lab™ software). All experiments are carried out in duplicate per samples and repeated at least in two independent assays.

References

[1] Mattox D. in *Handbook of physical vapor deposition (PVD) processing*, Noyes Publications, New Jersey,1998.

[2] Ohring M. in *Materials science of thin films* 2nd Edition, Academic Press, U.S.A., 2002.

[3] Carvalho P. *Development of new decorative coatings based on zirconium oxynitrides*, PhD thesis, s.l. Universidade do Minho, 2008.

[4] Wasa K., Hayakawa S. in *Handbook of Sputter Deposition Technology: Principles, Technology and Applications*, Noyes, New Jersey, 1992.

[5] P. Sigmund, *Theory of Sputtering. I. Sputtering Yield of Amorphous and Polycrystalline Targets*, Physical Review, 184 (1969) 383.

[6] Dutka M. *Processing and structure of nanoparticles, Characterization and modeling*, PhD thesis, s.l. University of Groningen, 2014.

[7] Ibrahimkutty S. *Production, deposition and characterization of metal nanoclusters using a gas aggregation source*, PhD thesis, s.l. Ernst-Moritz-Arndt-Universität Greifswald, 2005.

[8] M. Villarica, M. J. Casey, J. Goodisman, and J. Chaiken, *Application of fractals and kinetic equations to cluster formation*, Journal Chemical Physics, 98 (6) (1993) 4610-4625.

[9] E.Kesala, A.Kuronen, K.Nordlund, *Molecular dynamics simulation of pressure dependence of cluster growth in inert gas condensation*, Physical Review B, 75 (2007) 174121.

[10] S. Yamamuro, K. Sumiyama, M. Sakurai, K. Suzuki, *Cr cluster deposition by plasma–gas-condensation method*, Supramolecular Science, 5 (1998) 239—245.

[11] M. Gracia-Pinilla, E. Martınez, G. Silva Vidaurri, E. Perez-Tijerina, *Deposition of Size-Selected Cu Nanoparticles by Inert Gas Condensation*, Nanoscale Research Letters, 5 (2010) 180–188.

[12] A.N.Banerjee, R. Krishna, B. Das, *Size controlled deposition of Cu and Si nano-clusters by an ultra-high vacuum sputtering gas aggregation technique*, Applied Physic A, 90 (2008) 299–303.

[13] Brundle C., Evans A., Wilson S. *Encyclopedia of Materials Characterization*, Reed Publishing, U.S.A. 1992.

[14] Wagner C.D. in *Handbook of X-Ray Photoelectron Spectroscopy*, Perkin Elmer Corporation, U.S.A., 1979.

[15] R.Escobar Galindo, R.Gago, D.Duday, C.Palacio *Towards nanometric resolution in multilayer depth profiling: a comparative study of RBS, SIMS, XPS and SIMS,* Analytical and Bioanalytical Chemistry, 396 (2010) 2725-2740.

[16] Nelis T., Payling R. in *Glow discharge optical emission spectroscopy: A practical guide*, The Royal Society of Chemistry, UK, 2003.

[17] Williams D.B., Carter C.B. *Transmission Electron Microscopy A textbook for materials science*, Springer, U.S.A., 2009.

[18] Birkholz M. in *Thin Film Analysis by X-Ray Scattering*, Wiley-VCH, Singapore, 2006.

[19] P.Scherrer, N.G.W.Gottingen, Math Phys. KI2 (1918) 96.

[20] J.A.Thornton, D.W.Hoffman, *Stress-related effects in thin films*, Thin Solid Films, 17 (1989) 5-31.

[21] E.Mounkier, Y.Pauleau, *Mechanisms of intrinsic stress generation in amorphous carbon thin films prepared by magnetron sputtering*, Diamond Related Materials, 6 (1997) 1182-1191.

[22] Pimentel J.V.B., *Adaptive self-lubricating low-friction coatings*, PhD thesis, s.l. Technical University in Prague, 2013.

[23] ASTM G 99-04 (2004) *Standard Test Method for Wear Testing with Pin-on-Disc Apparatus.*

[24] Williams J., Dwyer-Joyce R. in *Modern Tribology Handbook*, II, CRC Press, 2001.

[25] Zoski G., *Handbook of Electrochemistry*, Elsevier, 2007.

[26] J. Hudzicki, Kirby-Bauer Disk Diffusion Susceptibility Test Protocol, Available Online:http://www.microbelibrary.org/index2.php?option=com_resource&controller=article&article=3189&category_id=1&format=html&print=1&Itemid=73 1

Chapter III

Ag/a-C Nanocomposite Coatings

In this chapter the first results related with Ag/a-C nanocomposite coatings deposited by magnetron sputtering are presented particularly concerning their characterization with respect to their chemical composition, structure and tribological properties. At this stage the main objective is to analyze and understand the main fundamental properties of the Ag/a-C system. Subsequently the Ag/a-C nanocomposites deposited by magnetron sputtering are compared with the nanocomposites deposited by hybrid method (MS of a-C and PGC of Ag nanoparticles). Since the PGC was implemented in the scope of this thesis, fundamental studies regarding the influence of deposition parameters (Ar flow and current density applied to Ag target) on the Ag-NP size, as well as the way how Ag nanoparticles grow on the substrate along time, are performed. The comparison is based on the uniformity in Ag particles size distribution in the matrix and in Ag uniformity along different locations in the substrate holder. The main conclusions drawn in this chapter allowed to select the work methodology adopted for the thesis core work.

The work developed in this Chapter resulted in 2 papers:

- N.K. Manninen, F. Ribeiro, A. Escudeiro, T. Polcar, S. Carvalho, A. Cavaleiro, *Influence of Ag content on mechanical and tribological behavior of DLC coatings*, Surface and Coatings Technology 232 (2013) 440-446. I.F.: 1.998.
- N.K. Manninen, N.M. Figueiredo, S. Carvalho, A. Cavaleiro*, Production and Characterization of Ag Nanoclusters Produced by Plasma Gas Condensation*, Plasma Processes and Polymers 11 (2014) 629–638. I.F.: 2.964.

1. Ag/a-C nanocomposite coatings deposited by magnetron sputtering

1.1 Chemical composition and deposition rate

The coatings thickness and chemical composition are determined through 2D profilometry and EPMA, respectively. It should be pointed out that the presented thickness values are the sum of Ti/TiN/TiCN interlayer (450 nm) and Ag/a-C layer thicknesses. The coatings deposition rate is calculated taking into account the coatings thickness and the deposition time. The results are depicted in Table 5.

Table 5 - Ag/a-C coatings chemical composition, thickness and deposition rate

Coating	Erosion Area Ratio Ag/C	Ag Content (at.%)	Thickness (μm)	Deposition Rate (μm/h)
a-C	0	0	1.7	0.50
Ag1	0.01	1.3	1.5	0.51
Ag3	0.03	3.7	1.6	0.60
Ag6	0.06	6.1	1.4	0.61
Ag13	0.11	13.1	1.4	0.80

The EPMA analysis revealed that the amount of Ag increased from 0 (for reference a-C coating) up to 13.1 at.%, for the coating deposited with the highest Ag/C relative erosion area (0.11). Moreover, the amount of oxygen, resulting from target contamination and residual atmosphere, is below 2 at.%. The coatings thickness is kept approximately constant, with values in the order of 1.4 μm to 1.7 μm. The coatings deposition rate increases with the amount of Ag incorporated in the coating: reference a-C coatings shows a deposition rate of 0.5 μm/h, which increases up to 0.8 μm/h for the Ag/a-C coating with the highest amount of silver. This increase was somehow expectable taking into account the higher sputtering yield of silver in relation to carbon (3.12 and 0.12, respectively, when bombarded with Ar at 500 eV)[1]. The Ag pellets are distributed in the carbon target in order to minimize the differences along the vertical direction in the substrate holder. In fact, during deposition the substrate holder is in rotation, thus the coatings should be uniform along the rotation direction; however, in the vertical direction, differences could be expected depending on the distribution of Ag pellets. In order to evaluate the coatings uniformity along the vertical direction three

silicon substrates are placed in the center and extremities of the substrate holder and the coatings thickness is evaluated being found that no differences in thickness were found. Thus, it is assumed that the deposition method allows to obtain uniform coatings.

1.2 Coatings structure

The coatings crystalline structure is evaluated through XRD analysis and the results are depicted in figure 14.

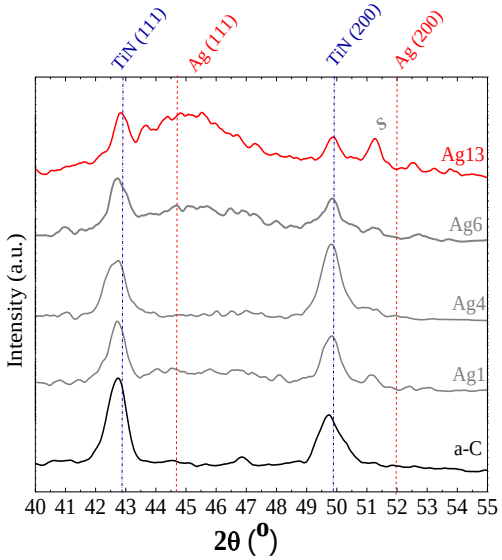

Figure 14 - XRD diffractograms of Ag/a-C coatings (preliminary results)

The main feature in XRD patterns are the peaks related with TiN (ICDD 01-087-0632) which represent the thicker component of Ti/TiN/TiCN interlayer. No other peaks are visible for a-C coating, which was expectable since carbon coatings form amorphous phases. The diffractogram of Ag/a-C nanocomposite coatings with Ag content below 6 at.% are similar to the reference a-C coating, while for the coating with 13.1 at.% Ag the presence of a broad peak located close to 45° is detected, which is related to the Ag phase (ICDD 181730). The grain size is determined through Scherrer method[2], which revealed the formation of nanocrystalline Ag with a grain size of about 2-3 nm. The absence of Ag peaks for lower Ag contents cannot exclude the presence of smaller Ag grains with sizes below 2 nm, which are not detectable by XRD analysis. As previously discussed in Chapter I, similar coatings also revealed the formation of nanocomposite coatings with nanocrystalline Ag phases dispersed in an amorphous

carbon matrix, which size increases with the amount of silver incorporated in the amorphous carbon matrix[3-5].

1.3 Coatings stability

The samples kept in atmospheric conditions (at about 25°C and relative humidity of about 40%); changed their color with time. A photograph of one as-deposited Ag/a-C nanocomposite is presented in figure 15 (a), which is compared with the same coating 6 months after deposition (see figure 15 (b)). The aged sample shows clearly a brighter color where the presence of a top dusty layer is observed. This feature only occurred in coatings with high Ag contents (6.1 at.% and 13.1 at.%). The Ag13 coating´s surface is analyzed by SEM/EDS-the SEM micrograph of the surface is presented in figure 15 (c). The coating's surface is covered by small particles combined with randomly oriented scratches originated by the sample handling. The EDS analysis performed inside and outside the scratched region (Z1 and Z2, respectively) suggests that the surface particles are Ag. In fact, an increase in silver content from 22 at.% to 30 at.% is found along with a decrease in the carbon content from 78 at.% down to 70 at.%. This changes suggest that Ag is segregating to coating´s surface, a phenomena already reported by several authors as reviewed in the state of the art, however, this process occurred at higher temperatures in the order of several hundred degrees centigrades[6-15]. In the case of the a-C matrix it seems that the surface segregation occurs even at room temperature.

Figure 15 - (a) as-deposited Ag/a-C coating,(b)Ag/a-C coating 6 months after deposition and (c) SEM micrograph of Ag13coating 6 months after deposition

1.4 Mechanical and tribological characterization

The coatings mechanical properties such as hardness and residual stress are determined and the results are plotted in figure 16.

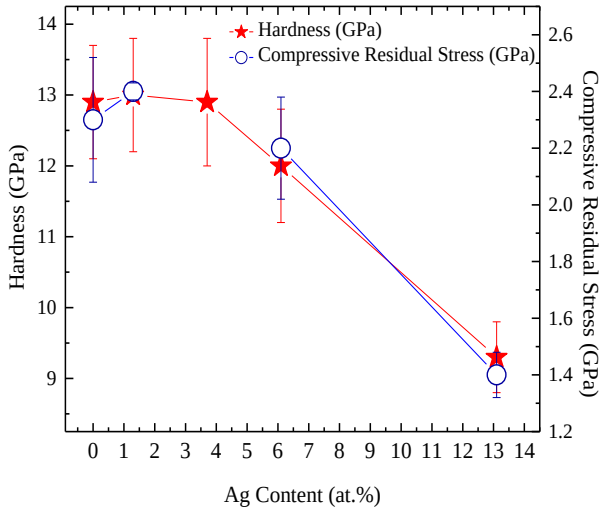

Figure 16 - Coatings hardness and residual stress state

The hardness and residual stress of a-C and Ag/a-C coatings with Ag contents below 13.1 at.% are almost identical showing values in the order of 12-13 GPa and 2-2-2.4 GPa, respectively; Ag13 coating showed a significantly lower hardness (9.3 GPa) and residual stress (1.4 GPa). The reduction in the coatings residual stress and hardness was previously reported by other authors for similar coatings, as reviewed in the state of the art[3,16,17]. These variations are well correlated with the coatings structure, where no evidence of crystalline Ag grains is detected for Ag contents below 13.1 at.%;, thus, the size of Ag clusters (if present) is too small to significantly affect the coatings mechanical properties. For higher Ag contents, a reduction in the coatings internal stress is clearly stated, related with either the decrease in the amount of sp^3 bonds and/or the relaxation induced by the presence of the metallic silver, as it was already reported to occur in Ag doped a-C coatings[3,4,5]. This reduction together with the presence of the soft Ag clusters promote a significant decrease in the coatings hardness.

The tribological tests are performed in dry sliding condition in a pin-on-disk tests against zirconia counterparts. Two different ball diameters and applied loads were tested, which results in different Hertzian contact pressures (Pm): 690 MPa and 1180

MPa. The friction curves are plotted in figure 17 (a) (for Pm=690 MPa) and (b) (for Pm=1189 MPa), together with the coatings wear rates in figure 17 (c).

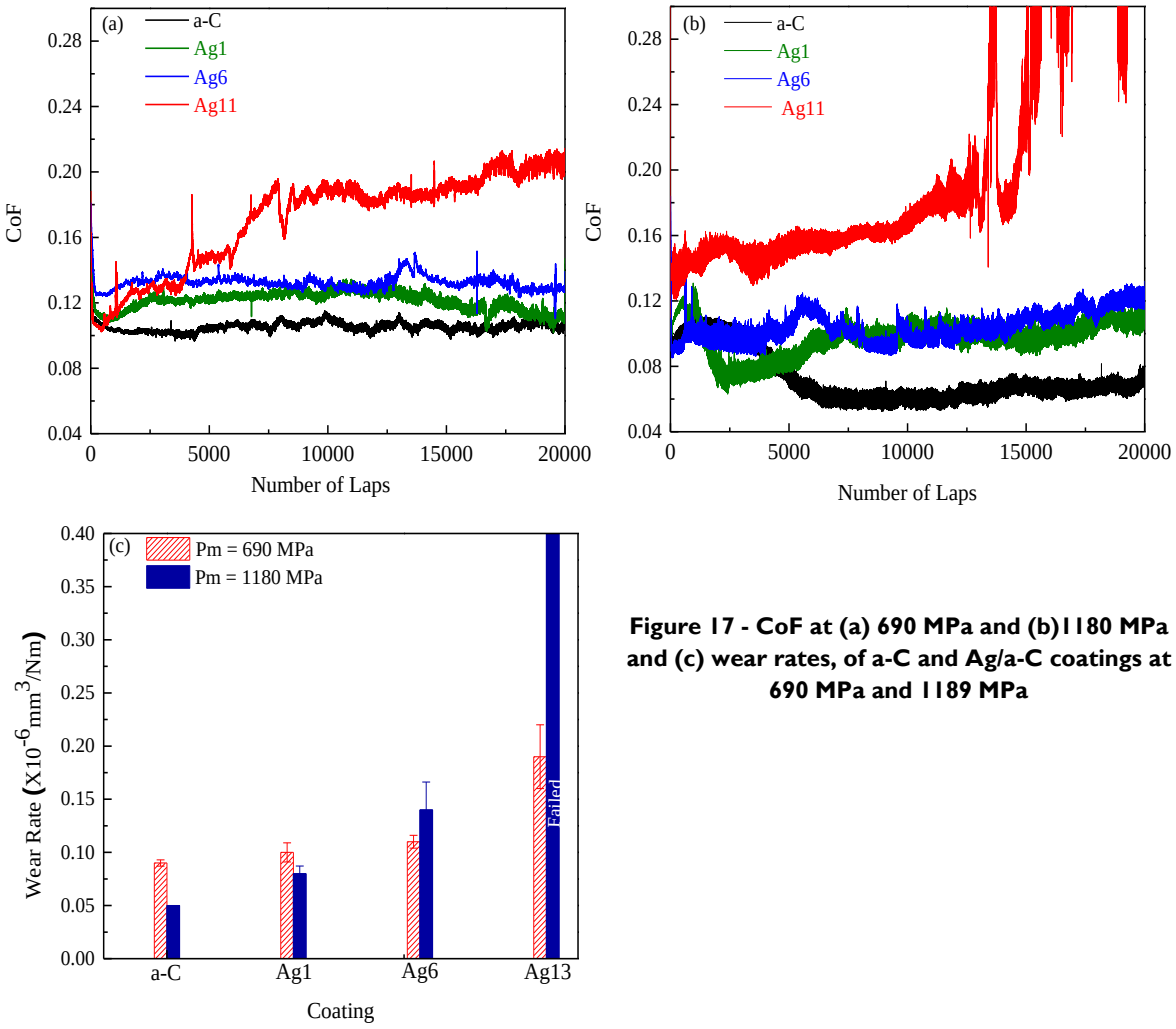

Figure 17 - CoF at (a) 690 MPa and (b)1180 MPa and (c) wear rates, of a-C and Ag/a-C coatings at 690 MPa and 1189 MPa

At lower Pm (690 MPa) the CoF values of a-C, Ag1 and Ag6 coatings are similar, in the range from 0.10 to 0.14, while the Ag13 coating starts at similar CoF values, but, after about 5000 laps, the friction coefficient increases up to about 0.2. At higher Pm (1180 MPa) a different trend is observed: (i) a-C and low Ag content coatings start with similar CoF values (about 0.10), which remain constant for Ag/a-C coatings along the 20000 laps, while for the a-C coating the friction coefficient decreases after about 5000 laps down to about 0.05 and (ii) the Ag13 coating shows again a higher CoF value in relation to the other tested coatings; however, after about 15000 laps the value increases continuously, which results in the total wear of the coating (see figure 17 (c)). The variation on coatings CoF values are well correlated with the coatings wear rate, being

observed that lower friction values result in lower wear rates, being the lowest wear rate obtained with a-C coating at higher Pm. This was somehow expectable since it is well established that the CoF and the wear rate of a-C coatings are lower at higher contact pressures and sliding velocities, which is attributed to the formation of a more compact transfer layer when testing conditions are more severe[18]. In fact, the lubricant properties of amorphous carbon coatings are attributed to the formation of carbon-carbon tribological pairs, where the presence of graphitic bonds promote the low friction[18]. In general, the friction and wear behavior of Ag/a-C coatings with low Ag content follow the same trend, although these values are slightly higher in silver containing coatings. The highest CoF and wear rate values are achieved for the Ag13 coating, which clearly indicates that the incorporation of high amounts of Ag degrades the tribological properties of amorphous carbon coatings. The degradation is more evident at higher Pm values, for which the a-C coating showed the lowest wear rates (below 0.05x106 mm^3/Nm) contrasting with Ag13 coating that completely failed. As reviewed in the state of the art, the degradation of the tribological properties of a-C coatings with the incorporation of high amounts of Ag (in the order of 5 at.% up to 11 at.%) had already been reported by Wu et al[19] and Dhandapani et al[20], as reviewed in the Chapter I. In relation to the incorporation of low amounts of Ag, both authors found improvements in a-C coatings tribiological behavior, which was not observed in our work.

In order to get more information about the frictional mechanisms which determine the tribological behavior of the Ag-containing coatings, the wear tracks of Ag6 and Ag13 coatings and the counterparts, when the sliding test was performed at 690 MPa, are detailed analyzed by SEM (figure 18). The micrographs of the transfer layer on the counterparts sliding against the Ag6 and Ag13 (figures 18 (a) and (b), respectively) coatings suggests relatively large areas rich in silver, which should appear much brighter than carbon in BSE mode, due to the higher atomic mass of Ag in relation to carbon. The wear track of Ag6 coating shown in figure 18 (c) is covered by Ag aggregates combined with smaller Ag clusters. The accumulation of Ag in the delamination zone is evident as well as the formation of Ag particles on the wear track borders, possibly due to their detachment from the delamination zone during the sliding process. It should be pointed out that the delamination zone is restricted to a local failure; however the clear observation of Ag accumulation in the wear track is clearly visible.

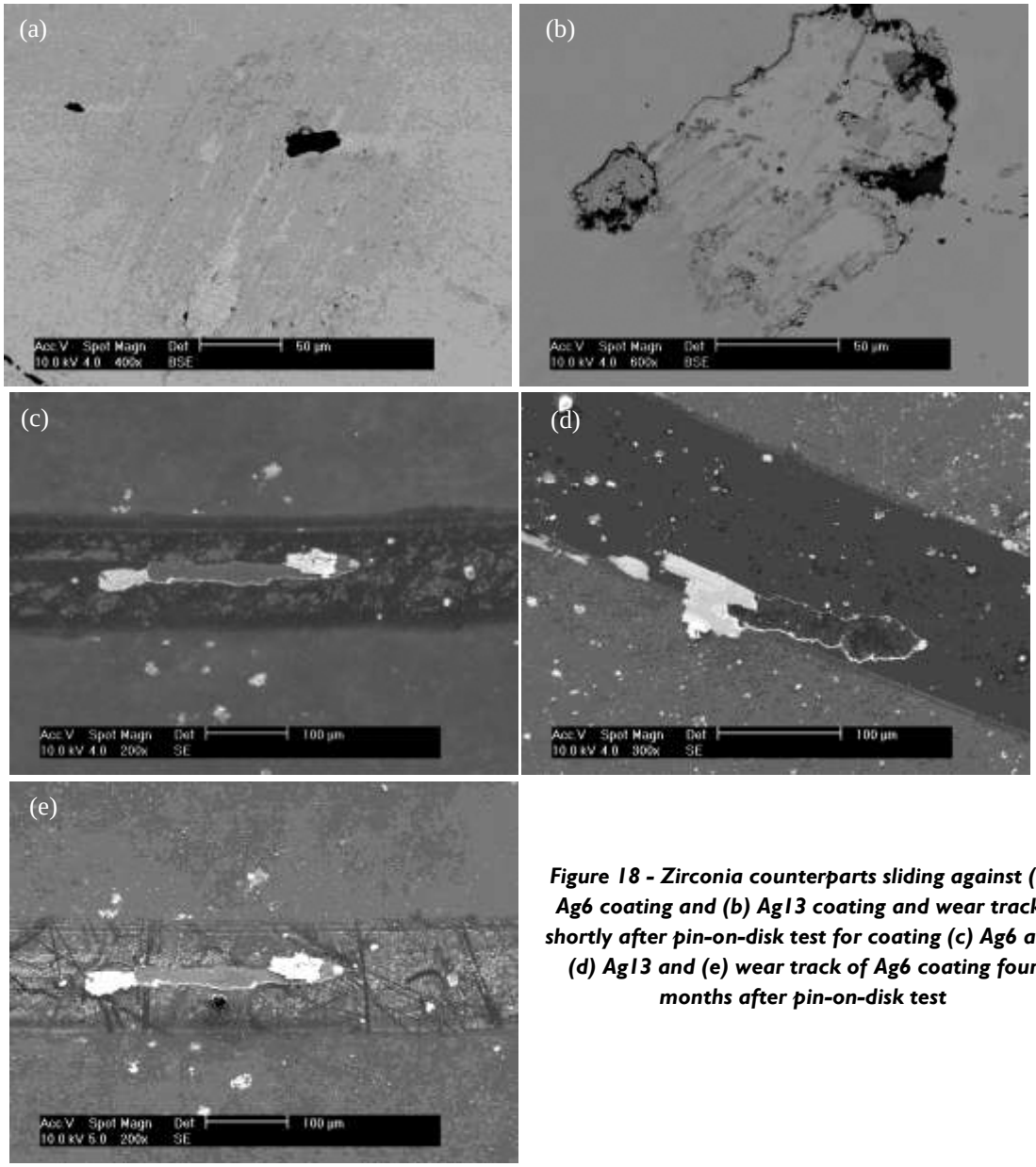

Figure 18 - Zirconia counterparts sliding against (a) Ag6 coating and (b) Ag13 coating and wear tracks shortly after pin-on-disk test for coating (c) Ag6 and (d) Ag13 and (e) wear track of Ag6 coating four months after pin-on-disk test

SEM analysis of the worn surfaces performed again, four months after the pin-on-disk test, reveal that the amount of Ag on the coating surface is enhanced (compare figures 18 (c) and e)). In fact, the wear track of Ag6 coating is totally covered by Ag, whereas other parts of the coating surface show only a small number of randomly distributed Ag particles (figure 18 (e)). The micrograph in the inset of figure 18 (c) is taken in the same zone in BSE mode, allowing stating that the bright aggregates found in the surface are related to Ag. Randomly oriented scratches on the surface are consequence of sample handling, which removed loosely adhered Ag particles. A similar behavior is found for coating Ag13, (see figure 18 (d)), where the accumulation of Ag in the delamination zone (not representative of the wear behavior for Pm = 690 MPa) is

observed, combined with silver aggregates at the wear track borders. According to the results obtained from SEM analysis, the formation of Ag rich transfer layer is observed as well as the accumulation of Ag in the wear track, which resulted in high CoF values when compared to the reference a-C coating. When incorporated into the matrix of hard coatings, such as TiCN[21], SiC and HfC[22], silver acts as a solid lubricant; however, hard nitride or carbide based coatings typically show much higher friction (typically 0.7–1) than the amorphous carbon coatings. In the latter case the friction is much lower (approx. 0.1) due to the formation of a graphite tribolayer. When the carbon-based tribolayer is replaced by silver, the friction inevitably increases. According to the results, it is presumed that Ag aggregates on the coating surface with time, due to the diffusion of silver atoms present either on the surface or at the first nanometers below the surface, as proposed in the scheme of figure 19. The variation on the worn surface with time indicates that Ag accumulates inside the wear track which, again should be associated to the diffusion of Ag from the layers below the surface (figure 19). From the SEM micrographs depicted in figure 18 (e), the amount of silver inside the wear track is higher in relation to the as deposited coating. However, since the coatings' surface was cleaned before the pin-on-disk test the segregated particles were removed, which explains the lower amount of silver outside the wear track.

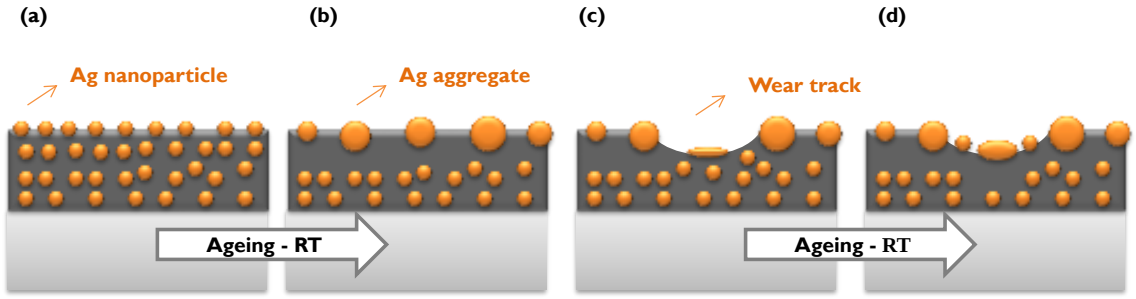

Figure 19 - Schematic representation of (a) as-deposited Ag/a-C coating, (b) Ag segregation with time, (c) Ag/a-C coatings structure after the wear test and (d) Ag surface segregation inside the wear track with time

2. Deposition of Ag nanoparticles by plasma gas condensation

Ag nanoparticles are deposited through the plasma gas condensation method. It should be pointed out that the nanoclusters source was implemented in the scope of this thesis; thus, the group had no previous experience with this technology, which means that the first objective of this thesis is to determine the most basic aspects related with this production technology. In this sense, several questions were risen:

i. What is the influence of the most relevant deposition variables on Ag particles size distribution?
ii. How does the Ag nanoparticles morphology and size vary with the increase of deposition time?
iii. Which are the oxygen contamination levels of the Ag nanoparticles produced by this method?
iv. How does Ag/a-C nanocomposite coatings grow when plasma gas condensation method is combined with magnetron sputtering of a-C coatings?

2.1 Influence of deposition parameters on Ag nanoparticles size distribution

In a first stage, the effect of two deposition parameters (Ar flow/pressure in the clusters source and current density applied to the Ag target, J_{Ag}) on the Ag clusters size distribution is analyzed. The TEM images are analyzed with the *ImageJ* software. The aggregates were left out of counting and only the dispersed NP with a circularity of 0.8–1 and sizes above 10 nm are considered. The mean nanoparticle size and standard deviation are also determined from the distribution of the measured diameters. NP diameter distribution is obtained by three micrographs for each sample. The TEM micrographs and histograms of Ag size distribution in the samples of first series are shown in figure 20. The variation of NP mean size with Ar flow is shown in figure 21 (a) while the variation of cluster source pressure and mean free path is shown in figure 21 (b).

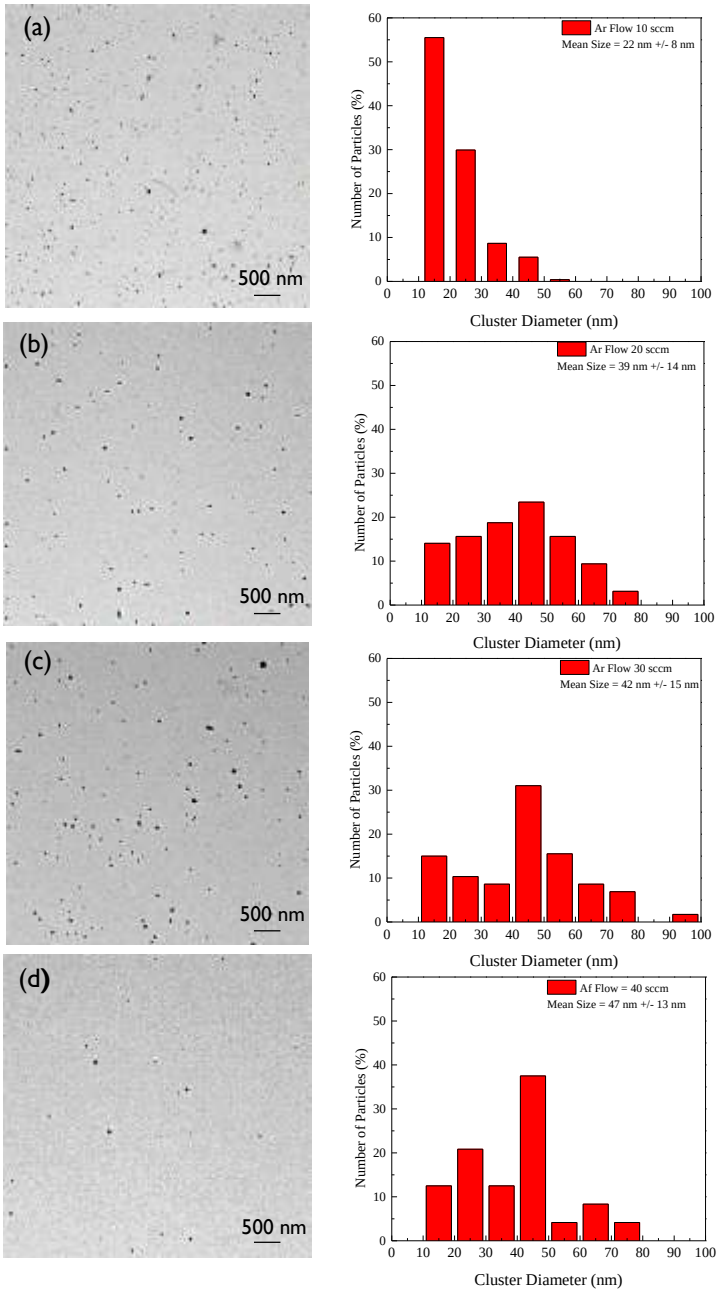

Figure 20 - TEM micrographs of Ag nanoclusters deposited with J_{Ag} = 7.6 mA/cm² and Ar flow of (a) 10 sccm, (b) 20 sccm, (c) 30 sccm and (d) 40 sccm

According to the results presented in figures 20 and 21 (a), the clusters size increases from 22 nm up to 39 nm when the Ar flow is increased from 10 to 20 sccm, while for higher Ar flows (20–40 sccm) the increase in clusters size is less pronounced. Similar sizes of Ag clusters were reported by Polonskyi et al.[23]. The role of argon in the clusters source is to sputter the metal target, which leads to ejection of metal atoms to the gas phase, as well as to participate in the condensation process. The clusters

nucleation and growth is mainly controlled by the collision probability, which is determined by the pressure inside the aggregation chamber and, also, by the clusters residence time[24]. When the argon gas flow is increased, Ar will remove the clusters faster, thus reducing their residence time in the aggregation chamber. Consequently, the interaction between Ar, clusters and metal atoms is reduced, which promotes a decrease in the clusters size[25]. Conversely, increasing the pressure will decrease the mean free path; thus, increasing the collision probability between Ar, metal atoms or clusters will result in an increase in the cluster size[26]. As previously mentioned, increasing the argon flow leads to an increase in the pressure inside the cluster source, as can be depicted in the inset of figure 21(b). Therefore, the variation of Ar flow and, consequently, both the cluster residence time and the mean free path of the gaseous species, leads to a competition between these two effects. According to figure 21(b), the variations in the cluster size are well correlated with the decrease in the mean free path. Thus, it might be concluded that the mean free path exerts a more pronounced effect on the cluster size than the residence time.

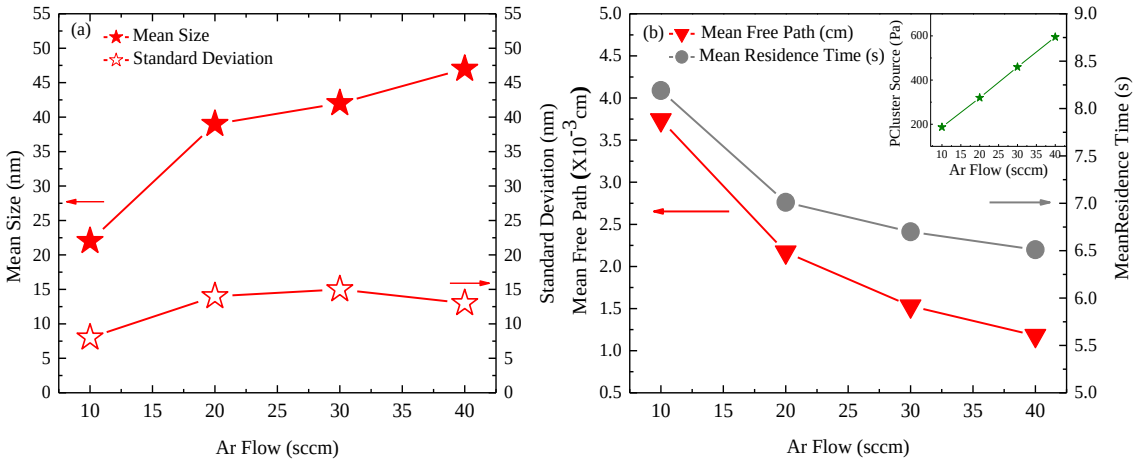

Figure 21 – (a) Variation of cluster mean diameter and standard deviation with Ar flow and (b) Variation of mean residence time and mean free path with Ar flow (the variation of pressure in cluster source with Ar flow is depicted in the inset)

The TEM micrographs and histograms of Ag size distribution in the samples of second series are shown in figure 22. The variation of NP mean size with applied current density (J_{Ag}) is shown in figure 23.

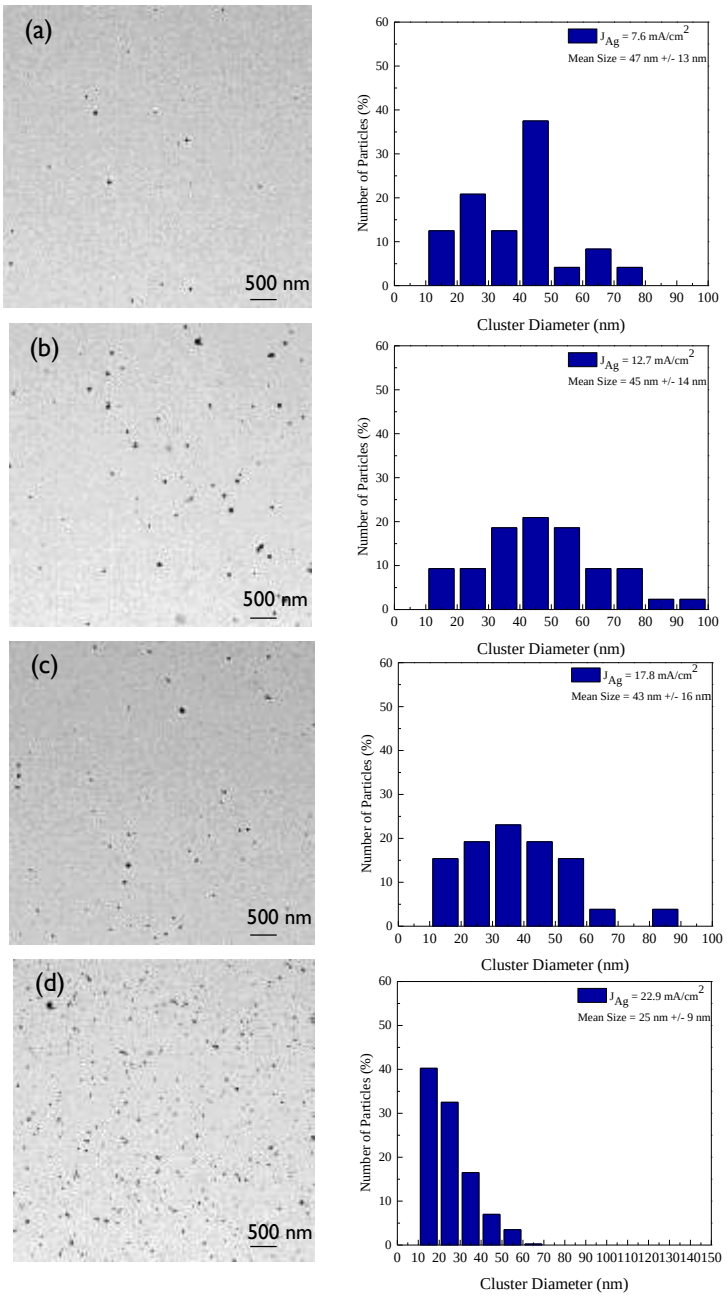

Figure 22 - TEM micrographs of Ag nanoclusters deposited with Ar flow of 40 sccm and J_{Ag} of (a) 7.6 mA/cm², (b) 12.9 mA/cm², (c) 17.9 mA/cm² and (d) 22.9 mA/cm²

According to the results depicted in figures 22 and 23, the increase of J_{Ag} between 7.6 mA/cm^2 and 17.8 mA/cm^2 leads to small variations in the clusters mean size, which varies from 47 nm down to 43 nm, while for higher J_{Ag} (22.9 mA/cm^2) the clusters mean size decreases down to 25 nm.

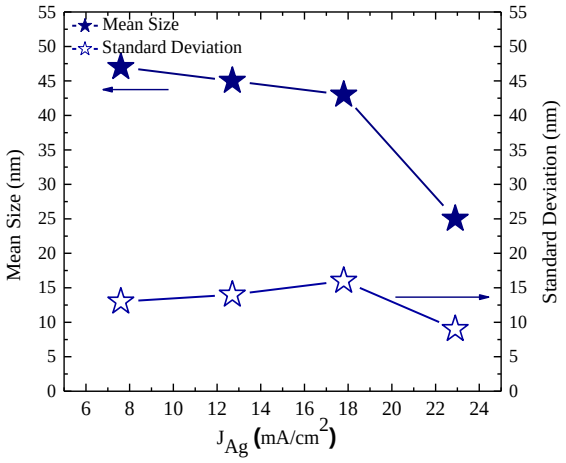

Figure 23 - Variation of the cluster mean diameter and its standard deviation as a function of the current density applied to the Ag target (J_{Ag})

Smirnov et al.[27] found that the average size of Ag clusters was independent of the discharge power; however, other works reported an increase in the cluster mean size with the increase of the current density/power density[24,27]. A similar trend to the one found in this work was previously reported by Drabik et al.[28] for titanium clusters. The increase of the discharge power reinforced the metal vapor density and, thus, the cluster growth should be favored. Nevertheless, the variation in the cluster size should be attributed not only to the clusters growth but also to the nucleation rate. The latter factor should play the major role in our case, helping explaining the inverse trend shown in figure 23. The increase in the metal vapor density may lead to an increase in the density of the nucleation sites, promoting the formation of a higher amount of clusters, with lower cluster mean diameter counterbalancing the effect of the high density on the clusters growth.

2.2 Nanoparticles growth on the substrate

Ag-NP are deposited in static mode with different deposition times in order to determine the evolution in nanoparticles size with time. For high current densities (J_{Ag} = 22.9 mA/cm^2) the deposition of individual clusters in static mode was performed in few seconds (about 3–4 s), which made difficult the control of the amount of deposited Ag clusters. In this sense, these depositions were performed at J_{Ag} 7.6 mA/cm^2 and Ar flow

of 30 sccm, due to the easier control of the deposition time. The TEM micrographs obtained for deposition times of 30 s, 1 min, and 3 min, are shown in figure 24 (a–c), respectively. The numbers of individual NP and Ag aggregates/islands, the ratio between these two numbers and the surface coverage (%) are presented in Table 6 as a function of the deposition time.

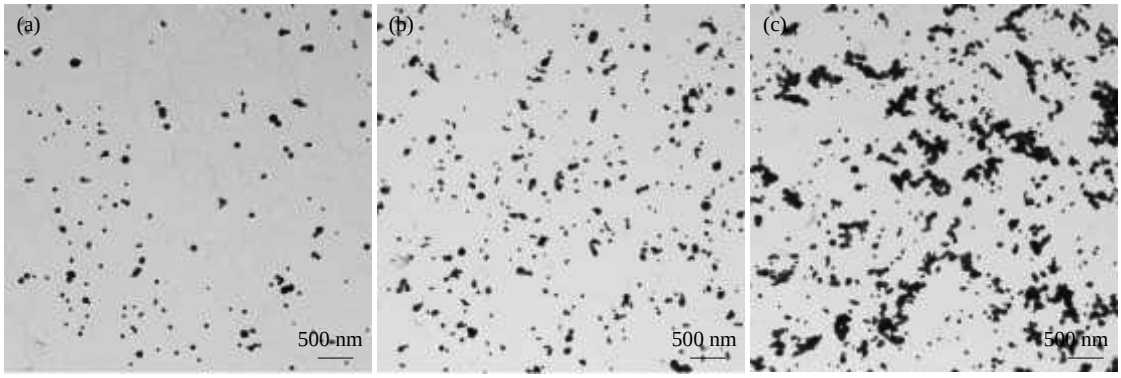

Figure 24 - TEM micrographs of Ag clusters deposited at an Ar flow of 30 sccm and J_{Ag} 7.6 mA/cm² with a deposition time of (a) 30 s; (b) 1 min. and (c) 3 min.

Table 6 - Evolution of the numbers of Ag-NP and Ag aggregates, the ratio between these two numbers and the surface coverage for different deposition times

Deposition Time (min.)	Number of NP´s	Number of Aggregates	Number NP´s/Number of Aggregates	Surface Coverage (%)
0.5	90	32	2.8	11
1	161	135	1.2	14
3	171	146	1.15	26

In figure 24 (a), only individual NP´s or small NP aggregates, containing about two individual nanoparticles, can be observed. Increasing the deposition time leads to an increase in the amount of both the individual NP´s and the aggregates (Table 6). However, the ratio between individual NP´s and aggregates decreases from 2.8 to 1.2 (see Table 6), meaning that some individual NP are aggregated and/or incorporated in existing aggregates, leading to the increase of their size, as can be depicted in figure 24 (b). The much higher global volume / area ratio of the NP´s in these conditions explains the small increase in the surface coverage (Table 6), in spite of the high increase in the total amount of NP´s. A further increase in the deposition time from 1 to 3 min leads to a constant number of individual NP´s and aggregates, despite the visible increase on

the surface coverage (%). Figure 24 (c) indicates the presence of individual nanoparticles, aggregates, and islands with irregular shapes. Therefore, it may be concluded that, at the first stages of the NP´s growth leads firstly to the formation of aggregates up to reach a density value which will remain constant with time. Then, the formation of bigger and bigger islands takes place with time. The mean size of the individual NP´s (with a circularity between 0.8 and 1), determined for each deposition time, is between 45 and 50 nm, which excludes the hypothesis of total coalescence. Previous studies[29,30] indicate that the growth mechanism in the substrate are controlled by (i) minimization of the system energy for low NP arrival rates, which favors the coalescence process and (ii) kinetic effects for high clusters arrival rates, which may favor the formation of aggregates. If the impinging NP interacts with an island or NP before the complete coalescence, it will freeze the coalescence process leading to the formation of islands. As reviewed in the theoretical background of the plasma gas condensation, the growth of islands with fractal like structures can also occur inside the clusters source, a phenomenon that was reported by M. Dutka[31]. In this work the results clearly indicate that the clusters growth inside the clusters source occurs only in stage 1 and 2 represented in figure 24, which leads to the formation of spherical and quasi-spherical NP.

2.3 Ag coatings structure and chemical composition

The coatings deposition time was further increased in order to produce Ag thin films from Ag nanoparticles. These are characterized with respect to their morphology, chemical composition and structure, through SEM, EDS and XRD analysis, respectively. The results for the Ag thin film deposited with a J_{Ag} of 7.6 mA/cm^2 and Ar flow of 40 sccm are presented in figure 25. It should be pointed out that similar results are obtained for thin films deposited with the other tested deposition conditions.

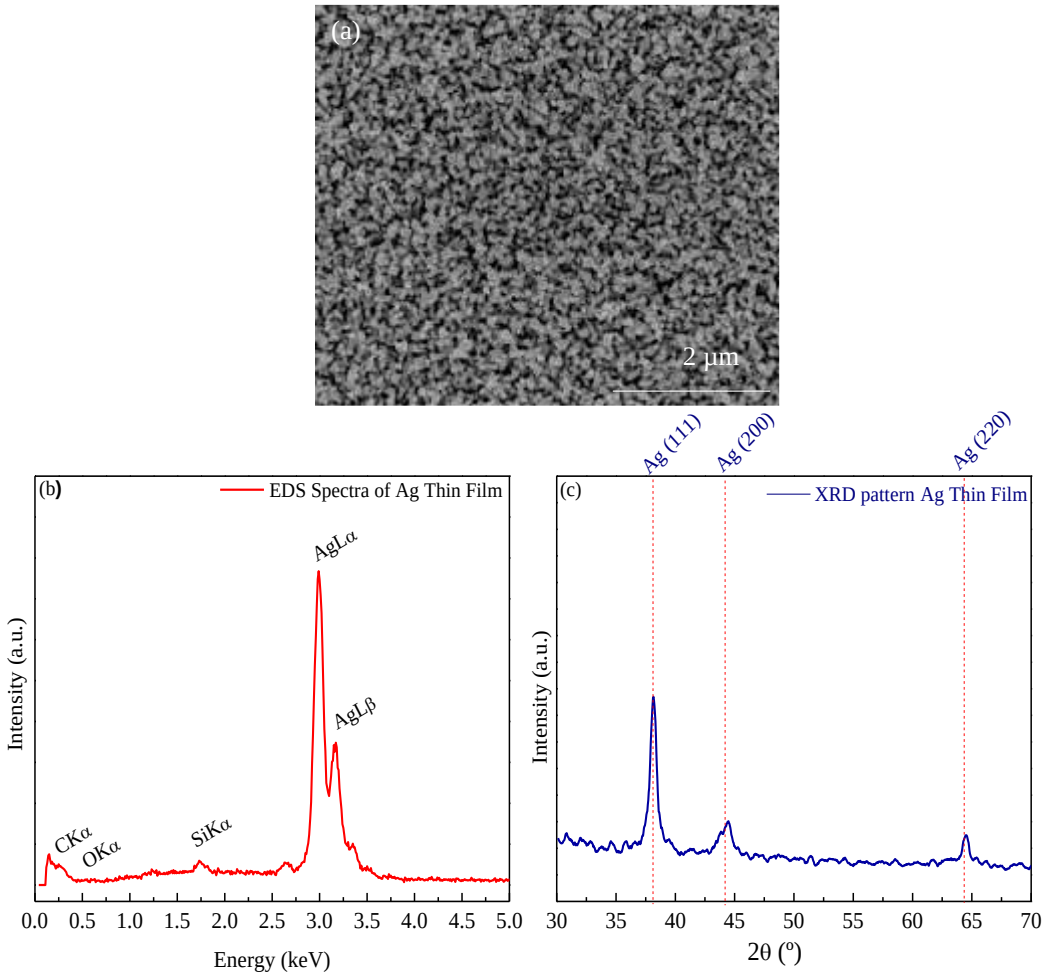

Figure 25 – (a) SEM top-view micrograph, (b) EDS spectra and (c) XRD diffractogram of the Ag coating deposited with J_{Ag}=7.6 mA/cm² and Ar flow of 40 sccm

SEM micrograph shows that a porous nanostructured thin film is obtained, with the typical morphology of clusters deposition in the soft landing mode. This kind of structures have high potential for several applications where high surface/volume ratio, and thus high reactivity, are required, such as for catalysis or antimicrobial surfaces. However, these films present very poor cohesive and adhesive strengths, being easily wiped out even during sample handling[26,29]. The EDS analysis reveals no presence of oxygen in the films, which indicates that the deposition system allows the deposition of Ag-NP with low levels of oxygen contamination, even without any direct pumping of the cluster source. The XRD diffractogram confirms the crystalline nature of the Ag-NP in agreement with the indexed fcc-Ag phase (ICDD card no 181730).

2.4 Ag/a-C nanocomposite coating deposited by hybrid deposition method (PGC+MS)

As previously mentioned, one of the major advantages of the plasma gas condensation method is the possibility to pre-form the clusters and combine their deposition with other thin film deposition process, such as the magnetron sputtering. Therefore, Ag/a-C nanocomposite coatings were deposited through the combination of Ag nanoparticles produced by plasma gas condensation with the a-C coatings matrix deposited by magnetron sputtering. The following fundamental issues learnt from the deposition of the Ag clusters in free surfaces, were taken into account for preparing the nanocomposite deposition:

i. The size distribution of the Ag nanoparticles is very broad;
ii. The variation of the deposition parameters leads to small variations in the clusters size distribution, being the mean size of the Ag nanoparticles close to 40 nm, for a large range of values of those parameters;
iii. If enough time is given in the deposition, the Ag nanoparticles can grow in the substrate leading to the formation of fractal like agglomerates.

Then, the deposition parameters were selected in order to achieve:

i. Individual Ag clusters: the main scope is to deposit a-C layers at a rate that enables to cover the individual Ag particles avoiding the particle agglomeration;
ii. Deposit the Ag nanoclusters and a-C coatings continuously. It should be pointed out that a-C layers and Ag nanoparticles could also be deposited in individual steps, resembling a multilayer deposition. However, since the deposition system does not allow the automatic control of multilayers deposition, such a deposition procedure could not be applied due to reproducibility problems, specially taking into account that, at high current densities, the Ag clusters cover the entire surface in few seconds, being difficult to avoid the formation of Ag agglomerates.

Another limitation of the deposition system is the gas line configuration. As previously mentioned in the experimental details, Ar is introduced through the clusters source into the main chamber of the deposition system, determining the pressures in both the clusters and deposition chambers. Therefore, the Ar flow should be selected in order to create the desired pressures which allow the proper Ag clusters production and the a-C thin films deposition. In this sense the Ar flow and the power density applied to the

carbon target are selected to be as similar as possible to those used in the deposition of the first a-C samples discussed in section 1. This was achieved with an Ar flow of 40 sccm. Regarding the Ag nanoclusters production, the lowest current density is used in order to avoid particles agglomeration in the substrate. Another important aspect in the coatings deposition is the uniformity expected for the samples in the covered space. Since the substrate holder is in rotation mode (18 rpm), the samples are uniform along the horizontal direction; however, due to the small size of the nozzle, the uniformity along the vertical direction has to be checked. In this sense, two silicon substrates are placed in two positions in the vertical direction in order to check the samples uniformity, one directly in front of the nozzle exit and the other 3 cm apart in the vertical direction (SEM top-view micrographs in figures 26 (a) and (b), respectively).

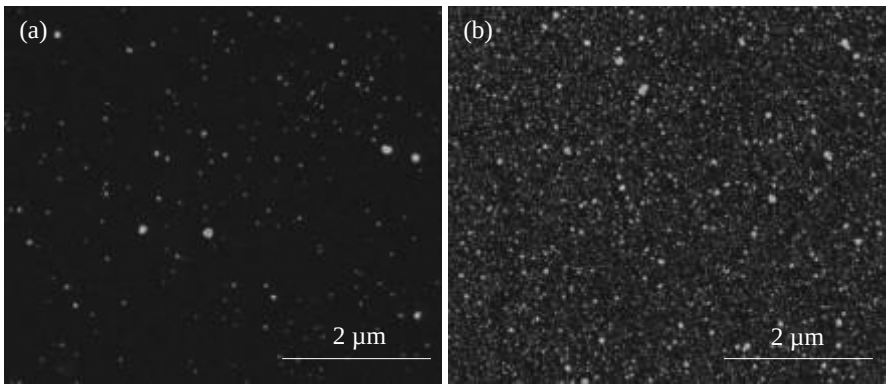

Figure 26 - SEM top-view micrographs of Ag/a-C nanocomposite coatings deposited by hybrid process with silicon substrates placed (a) 3 cm apart from the nozzle orifice in the vertical direction and (b) in front of the nozzle exit

The SEM micrographs clearly demonstrate the huge difference in the amount of Ag nanoparticles in both coatings, which means that the deposition method is not efficient for the production of large scale substrates. Moreover, the highest amount of Ag possible to be incorporated in the coating, even when placed in front of the exit orifice, is about 4 at.%.

In order to make the system more reliable for nanocomposite coatings production, several improvements are required:

i. Incorporation of two independent flowmeters, one for the main deposition chamber and the other for the nanoclusters source;

ii. Development of an automatic control for the coatings deposition, which allow to produce the coatings in multilayer configuration;
iii. Development of new nozzles which enable to increase the coatings uniformity in larger areas;
iv. Incorporation of a mass filter which enable to obtain the desired particle size with a much narrower distribution.

Due to the limitations inherent to the hybrid deposition method, in particular: (i) the large distribution of NP size, (ii) the low amount of Ag possible to incorporate in the coatings and (iii) the low coated area with uniform characteristics and properties, to achieve the initial objectives proposed in the aim of this thesis, the conventional magnetron sputtering method was mainly used for the production of the final nanocomposite coatings.

3. Selection of work methodology

The main goal of this thesis is the production Ag/a-C nanocomposite coatings for potential application as antibacterial surfaces. The preliminary work described above and performed with coatings deposited by the two methods, magnetron sputtering and hybrid process, allowed to draw some issues important for the further development of this study, as follows some fundamental conclusions in relation to the nature of this coatings and also in relation to the deposition methods:

i. Ag/a-C nanocomposite coatings are not stable at room temperature conditions. The work presented in section 1 is sum up with the scheme for Ag surface segregation presented in figure 19. However, a more detailed study in relation to the coatings stability is necessary in order to understand and control the process of surface segregation of silver. In fact, from the application point of view this is an essential point, since the knowledge of the coatings stability is fundamental for the development of new functional products requiring that either Ag is kept stable or is continuously controlled segregating with time.

ii. Conventional magnetron sputtering is a more suitable technique for Ag/a-C nanocomposite coatings production since it enables to get a better control of the Ag nanoparticles size distribution at microscopic and macroscopic scales and allows coating large areas, fundamental issue for producing samples in enough amount for electrochemical, biological and tribological characterization.

A schematic representation of the coatings developed in the thesis core work are shown in figure 27.

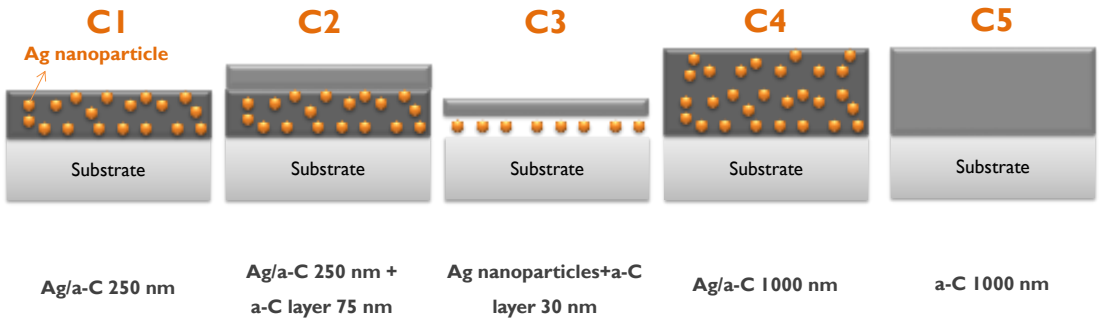

Figure 27 - Schematic representation of the coatings analyzed in the main thesis work

The designation Ag/a-C refers to nanocomposite layer while a-C refers to pure amorphous carbon coatings without silver. All coatings were deposited by magnetron sputtering with exception of coating C3 which was produced by combining PGC for clusters deposition and MS for a-C layer deposition. All Ag/a-C nanocomposite layers were deposited under similar conditions. The coatings thickness was selected by varying the deposition time; thickness values are given in the scheme of figure 27. In addition a 750 nm thick Ag/a-C layer is deposited over a polymer foil for TEM cross-sectional analysis. The work methodology adopted for the thesis core work is shown in Table 7.

Table 7 - Work methodology adopted for the thesis work

Question	Origin of Question	Coatings Characterization	Sample(s)	Chap.
How is Ag distributed in a-C matrix across the thickness?				
Ag distribution	State of the Art	SEM+TEM	C1 and C2	IV
Ag grain size distribution		GIXRD	C1 and C4	
How does the thickness influence the morphology?				
Ag/a-C cross-sectional morphology		SEM	C1 and C4	
How coatings thickness / morphology influence the segregation?	State of the Art			
Ag morphology with time		SEM	C1 and C4	V
From which depth Ag segregates?	Previous Work			
Ag in-depth distribution		GDOES		
Does Ag move through a-C matrix? Which is the diffusion mechanism?	State of the Art	*In-situ* TEM	C3	V
How does the atmospheric conditions influence the Ag stability?	Previous work + State of the Art	SEM	C4	V
What is the driving force for Ag segregation?	State of the Art	Substrate deflection SEM/EDS XPS GIXRD	C4	V
Are the coatings antibacterial? How does Ag particle size affects the antibacterial activity?	State of the Art	ICP Halo Inhibition Test	C4 and autoclaved C4, C5	VI
How is the Ag ionization rate with time?				
How does the lubrication with biological fluids influences the tribological behavior?	Previous Work + State Art	Pin-on-Disk	C4,C5	VI

3.1 Deposition method and parameters used in the thesis core work

As previously mentioned magnetron sputtering is the selected deposition method for the coatings production. The approach followed for the incorporation of Ag in the nanocomposite coatings is based on the use of a composite target consisting in Ag pellets inserted in the carbon target. This method has as major disadvantage: the poor reproducibility, associated with the differential erosion of the target material and the pellets, which leads to differences in the chemical composition with time. This problem is even more pronounced in Ag/a-C coatings, due to the huge difference in the sputtering yields of C and Ag. Thus, in order to allow a more precise control on the deposition process, the dual magnetron sputtering configuration is selected. In this method, two independent targets are used: one Ag target (purity of 99.99%, acquired from Testbourne) and one C target, both with similar dimensions. The first concern is to guarantee the deposition of nanocomposite coatings, i.e. to be sure that Ag is inserted forming nanoparticles instead of a continuous layer giving rise to a multilayer coating. Due to the huge difference in the C and Ag sputtering yields, maximum and minimum possible power densities are applied to the targets, respectively, to avoid that situation. The maximum power density possible to apply to the carbon target is 7 W/cm^2, which represents a total power of 1400 W, although the Advanced Energy Pinneacle Plus power supply allows 6 kW. However, as the maximum voltage in the source is limited to 800 V, only 1400 W can be applied since the target voltage is already at 780 V. Regarding the power density applied to Ag target, it is set at 0.09 W/cm^2, which represents the minimum power density at which plasma is formed. This value represents the breakdown voltage, where the transition to self-sustained discharge occurs.

The coatings were deposited in Ar atmosphere with substrates rotating at 8 cm from the target at a constant speed of 18 rpm. The base pressure in the deposition chamber was approximately 9×10^{-4} Pa; the pressure rose up to values of approximately 5×10^{-1} Pa during the deposition, after introduction of the discharge gas. The substrate holder is connected to a pulsed dc power supply and a bias voltage of -50 V is applied during the deposition, being the reverse time and frequency 0.5 μs and 250 kHz, respectively. The deposition parameters, namely, J_{Ag}, J_C, deposition time and deposition method used for the deposition of Layer I and Layer II are summarized in Table 8.

Table 8 - Deposition conditions used in Ag/a-C nanocomposite coatings deposition in main work

Coating	Layer I				Layer II		
	J_{Ag} (W/cm^2)	J_C (W/cm^2)	Time (min.)	Method	J_C (W/cm^2)	Time (min.)	Method
C1	0.09	7	25		-	-	-
C2	0.09	7	25	MS	7	9	MS
C3	2.6	-	10	PGC	7	4	MS
C4	0.09	7	120	MS	-	-	-
C5	-	7	165	MS	-	-	-

Previously to coatings deposition a sputter cleaning procedure is performed to both the targets and the substrates. The power densities applied to the C and Ag targets are 1.75 W/cm^2 and 0.25 W/cm^2, respectively. The substrate holder is connected to a pulsed dc power supply being the voltage fixed at 500 V; the reverse time and frequency are 1.6 μs and 250 kHz, resulting in a reverse phase of 40 %. The total etching time is 45 minutes.

The substrates used in this stage are: silicon, SS316L, TEM grids with carbon foil. Previously to the deposition process, the steel substrates are polished and all substrates are ultrasonically cleaned in acetone, ethanol and distilled water, for 10 minutes in each solvent, except TEM grids where no previous sputter etching nor washing procedures are performed.

In a first stage, C4 coating is deposited in order to determine the deposition rate and the chemical composition. EPMA indicates that the coating contains approximately 20 at.% Ag and 80 at.% C; the amount of oxygen is below 2 at.%. The thickness measured by SEM cross-sectional observation is 1 μm, which means that the deposition rate is close to 8 nm/min. This value allowed to adjust the deposition time in order to achieve the desired thicknesses. It should be pointed out that the deposition rate is determined for every coating, being possible to confirm that similar values are always achieved. However, for the chemical composition, only the thickest coating is analyzed since the depth of analysis by EPMA is higher than the thickness of the thinner coatings. Since the power densities applied to the targets are not changed, it is assumed that all of them have similar chemical compositions. A very thin Ag/a-C nanocomposite thin film is deposited in a TEM grid with carbon foil, which allowed to confirm the formation of a nanocomposite structure.

4. Conclusion

The work developed in the first stage of the PhD work allowed to set the guidelines for the work developed in the thesis core. In the first stage, the main goal is to study the structural, mechanical and tribological behaviors of Ag/a-C nanocomposite coatings deposited by magnetron sputtering. During this stage it is concluded that the coatings are not stable even in atmospheric condition (RT and relative humidity of 40%), which leads to the degradation of the tribological properties, when high amounts of silver are incorporated. In this sense, the main focus of this thesis is the analysis of Ag/a-C nanocomposites stability and its consequence on the coatings functional properties.

The deposition of Ag/a-C coatings is performed by two different approaches: magnetron sputtering and hybrid deposition method combining Ag nanoparticles formation by plasma gas condensation and a-C deposition by magnetron sputtering. The two methods are compared in relation to their ability to produce narrow Ag nanoparticle size distribution and large areas of coating with uniform properties. The results reveal that the Ag nanoparticle size distribution in PGC method is broader and its ability to give rise to uniform deposition in substrates, with dimensions suitable for the evaluation of the functional properties, is low. Therefore, to accomplish the major objective of the thesis, i.e. to get a better understanding about the Ag/a-C performance, dual magnetron sputtering method is selected.

References

[1] Vossen J.L., Kern W., *Thin Film Processes*, Academic Press, 1978.

[2] P.Scherrer, N.G.W.Gottingen, Math Physics KI2, (1918) 96.

[3] H. W. Choi, J.H. Choi, K.R. Lee, J.-P. Ahn , K. H. Oh, *Structure and mechanical properties of Ag-incorporated DLC films prepared by a hybrid ion beam deposition system*, Thin Solid Films, 516 (2007) 248 – 251.

[4] G. Matenoglou, G.A. Evangelakis, C. Kosmidis, S. FouliasD. Papadimitriou, P. Patsalas, *Pulsed laser deposition of amorphous carbon/silver nanocomposites*, Applied Surface Science, 253 (2007) 8155–8159.

[5] H.S. Zhang, J.L. Endrino, A. Anders, *Comparative surface and nano-tribological characteristics of nanocomposite diamond-like carbon thin films doped by silver*, Applied Surface Science, 255 (2008) 2551–2556.

[6] A.A. Voevodin, C. Muratore, S.M. Aouadi, Hard coatings with high temperature adaptive lubrication and contact thermal management: review, Surface and Coatings Technology, 257 (2014) 247-265.

[7] J.J. Hu, C. Muratore, A.A. Voevodin, Silver diffusion and high-temperature lubrication mechanisms of YSZ–Ag–Mo based nanocomposite coatings, Composites Science and Technology, 67 (2007) 336–347.

[8] C. Muratore, J.J. Hu, A.A. Voevodin, Adaptive nanocomposite coatings with a titanium nitride diffusion barrier mask for high-temperature tribological applications, Thin Solid Films, 515 (2007) 3638 – 3643.

[9] C.P. Mulligan, D. Gall, CrN–Ag self-lubricating hard coatings, Surface and Coatings Technology, 200 (2005) 1495 – 1500.

[10] C.P. Mulligan, T.A. Blanchet, D. Gall, CrN–Ag nanocomposite coatings: Effect of growth temperature on the microstructure, Surface and Coatings Technology, 203 (2008) 584–587.

[11] C.P. Mulligan, T.A. Blanchet, D. Gall, Control of lubricant transport by a CrN diffusion barrier layer during high-temperature sliding of a CrN–Ag composite coating, Surface and Coatings Technology, 205 (2010) 1350–1355.

[12] C.P. Mulligan, T.A. Blanchet , D. Gall, CrN–Ag nanocomposite coatings: High-temperature tribological response, Wear, 269 (2010) 125–131.

[13] C.P. Mulligan, T.A. Blanchet, D. Gall, CrN–Ag nanocomposite coatings: Tribology at room temperature and during a temperature ramp, Surface and Coatings Technology, 204 (2010) 1388–1394.

[14] C.P. Mulligan, P.A. Papi, D. Gall, Ag transport in CrN–Ag nanocomposite coatings, Thin Solid Films, 510 (2012) 6774-6779.

[15] P.A. Papi, C.P. Mulligan, D. Gall, CrN–Ag nanocomposite coatings: Control of lubricant transport by diffusion barriers, Thin Solid Films, 524 (2012) 211-217.

[16] C. Wang, X. Yu, M. Hua, *Microstructure and mechanical properties of Ag-containing diamond-like carbon films in mid-frequency dual-magnetron sputtering*, Applied Surface Science, 256 (2009) 1431–1435.

[17] Y. Wu, J. Chen, H. Li, L. Ji ,Y. Ye, H. Zhou, *Preparation and properties of Ag/DLC nanocomposite film fabricated by unbalanced magnetron sputtering*, Applied Surface Science, 284 (2014) 165-170.

[18] Donnet C. and Erdemir A. in *Tribology of Diamond-like carbon films*, Springer, New York, 2008.

[19] Y. Wu, J. Chen, H. Li, L. Ji ,Y. Ye, H. Zhou, *Preparation and properties of Ag/DLC nanocomposite film fabricated by unbalanced magnetron sputtering*, Applied Surface Science, 284 (2014) 165-170.

[20] V.Dhandapani, E. Thangavel, M. Arumugam, K. S. Shin, V. Veeraraghavan, S. Yau, C. Kim, D.-E. Kim, *Effect of Ag content on the microstructure, tribological and corrosion properties of amorphous carbon coatings on 316L SS*, Surface and Coatings Technology, 240 (2014) 128-136.

[21] J.C. Sánchez-López,, M.D. Abad , I. Carvalho, R. Escobar Galindo, N. Benito, S. Ribeiro , M. Henriques ,A. Cavaleiro, S. Carvalho, *Influence of silver content on the tribomechanical behavior on Ag-TiCN bioactive coatings*, Surface and Coatings Technology, 206 (2012) 2192-2198.

[22] J.E. Krzanowski, J.L. Endrino, J.J. Nainaparampil, and J.S. Zabinski, *Composite Coatings Incorporating Solid Lubricant Phases*, Journal of Materials Engineering and Performance, 13(4) (2004) 439.

[23] O. Polonskyi, P. Solar, O. Kylian, M. Drabik, A. Artemenko, J.Kousal, J. Hanus, J. Pesicka, I. Matolınov, E. Kolıbalov, D.Slavınska, H. Biederman, Nanocomposite metal/plasma polymer films prepared by means of gas aggregation cluster source, Thin Solid Films, 520 (2012) 4155.

[24] A. I. Ayesh, N. Qamhieh, H. Ghamlouche, S. Thaker, M. El-Shaer, *Fabrication of size-selected Pd nanoclusters using a magnetron plasma sputtering source*, Journal of Applied Physics, 107 (2010) 034317.

[25] A. N. Banerjee, R. Krishna, B. Das, *Size controlled deposition of Cu and Si nano-clusters by an ultra-high vacuum sputtering gas aggregation technique*, Applied Physics A, 90 (2008) 299.

[26] S. Yamamuro, K. Sumiyama, M. Sakurai, K. Suzuki, *Cr cluster deposition by plasma-gas-condensation method*, Supramolecular Science, 5 (1998) 239.

[27] B. M. Smirnov, I. Shyjumon, R. Hippler, *Flow of nanosize cluster-containing plasma in a magnetron discharge*, Physical Review E, 75 (2007) 066402.

[28] M. Drabik, A. Choukourov, A. Artemenko, J. Kousal, O.Polonskyi, P. Solar, O. Kylian, J. Matousek, J. Pesicka, I.Matolınova, D. Slavınska, H. Biederman, *Morphology of Titanium Nanocluster Films Prepared by Gas Aggregation Cluster Source*, Plasma Processes and Polymers, 8 (2011) 640.

[29] P.Jensen, *Growth of nanostructures by cluster deposition: Experiments and simple models*, Review in Modern Physics, 71 (1999) 1695.

[30] B. Yoon, V. M. Akulin, Ph. Cahuzac, F. Carlier, M. Frutos, A. Masson, C. Mory, C. Colliex, C. Brechignac, *Morphology control of the supported islands grown from soft-landed clusters*, Surface Science, 443 (1999) 76.

[31] Dutka M. *Processing and structure of nanoparticles, Characterization and modeling*, PhD thesis, s.l. University of Groningen, 2014.

Chapter IV

Structure and Morphology

Besides the specific properties of Ag and the matrix material, the performance of the nanocomposite thin films critically depends on the Ag nanoparticles size distribution and morphology as well as on the interfaces between the nanoparticles and the matrix. Accordingly, a careful characterization of the nanocomposite films morphology and nanostructure is the first step towards the understanding of the film properties evolution and the subsequent optimization for its performance. In this chapter, TEM, SEM and GIXRD techniques are used for accessing the size of Ag nanoparticles, their size distribution across the coatings thickness since, as previously reviewed in the State of the Art, it is reported to be non-uniform. According to the literature review, the most important aspect related to the Ag segregation is the morphology of the coating matrix; thus, the first step to control the nanocomposite stability is the control of the coatings structure and morphology. In order to deposit coatings with similar Ag filling factors and size distributions, the deposition parameters should be precisely selected.

In this chapter an overview of the basic concepts related with the coatings morphology is given, which allowed to set the basis for selecting the deposition conditions that allow to change the coatings morphology, while maintaining the Ag nanoparticle size and the filling factor constant. Afterwards, the Ag particle and grain size along the coatings depth is evaluated.

- The work developed in this chapter resulted in 1 paper: N.K. Manninen, J.C. Oliveira, S. Carvalho, A. Cavaleiro, *Characterization of surface Ag nanoparticles in nanocomposite a-C:Ag coatings by GIXRD at sub critical angles of incidence*, Submitted to Applied Physics A.

1. Morphology of thin films: Basic concepts

Along time different structure zone models (SZM) have been proposed for thin films deposited by PVD, which correlate the most relevant deposition parameters with the coatings morphology. In general the thin films growth involves several processes: (i) shadowing, (ii) surface diffusion and (iii) bulk diffusion[1]. The most popular SZM for sputtered thin films was developed by Thornton[2] and it accounts four different zones (1,T,2,3), represented in figure 28, which reflect the dependence of the coatings morphology on the inert gas pressure and the ratio between the substrate temperature(T_s) and the melting point of the growing film (T_m).

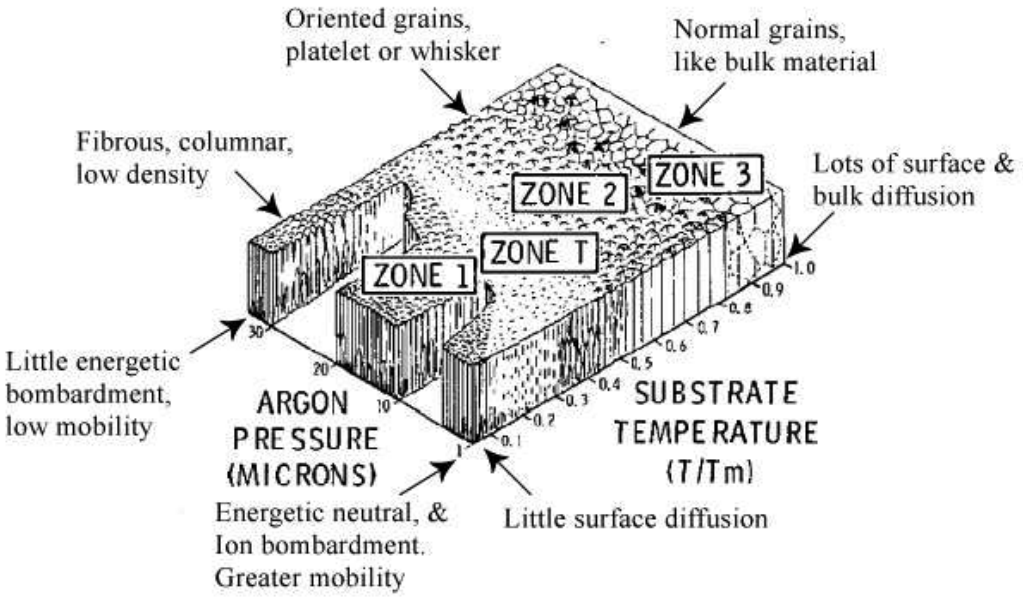

Figure 28 - The Thornton Structure Zone Model[1]

The Zone 1 growth mode is governed by shadowing effects, which arise from geometric constraints imposed by the roughness of the growing film and the line of sight impingement of the arriving atoms. The Zone 2 is governed by surface diffusion while zone T is an intermediate growth mode between Zone 1 and 2. In Zone 3, compact coatings are formed due to the high bulk diffusion. Other SZM have been developed, which have accounted with new variables introduced in the sputtering process. For example, the SZM proposed by Messier[3] considers the effect of the bias voltage applied to the substrate holder. In summary, the thin films growth mode depends mainly on the particles mobility, which is determined either by the substrate temperature or by the

energy delivered to the growing thin film, through energetic particle bombardment (bias voltage). The shadowing effect promoted by elevated pressures tends to randomize the direction of deposited atoms, through collisions with inert gas[1,2,3,4], also having impact in the final morphology.

The occurrence of columnar growth has been reported to occur either in crystalline and amorphous coatings[1]. In the crystalline coatings the columnar microstructure is described by the survival of crystallites which nucleate with the direction of the faster growth perpendicular to the substrate[5]. Bales et al[6] have developed a model for the growth of amorphous thin films which takes into account the surface diffusion and the geometrical shadowing effects. They reported that the columnar structure is mainly attributed to the survival of the fittest columns The origin of the columns is not simply a geometrical shadowing effect but also depends from the random walk nature of the diffusion process, which tends to move the particles to the top of the protruding columns rather than to the space between them. A comparative model between two similar growing surfaces, with different values of diffusion coefficient, showed that the column width as well as the height at which grooves start to appear depends on the diffusion coefficient (see scheme on figure 29).

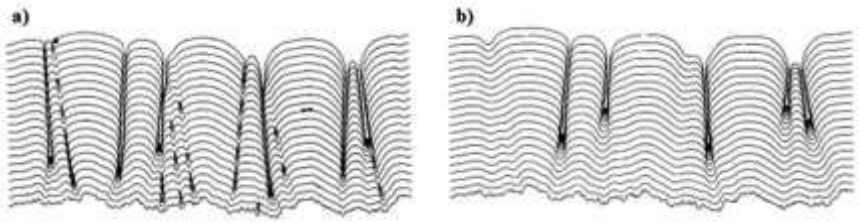

Figure 29 - Growth of amorphous films modeled by Bales et al[6], with different diffusion coefficients, (a) showing a higher D in relation to (b)

One of the main objectives of this thesis is the deposition of nanocomposite coatings with similar Ag particle size and contents, although with different morphologies, in order to understand the influence of the morphology on the coatings stability, which will be the scope of the next Chapter. The most common approach to change the coatings morphology is to vary the substrate temperature, the inert gas pressure or the bias voltage, although any variation can also change the Ag mobility with the consequent well known effect on the Ag particle sizes. In this sense, the variation of the coatings thickness was adopted as the method to vary the coatings morphology without changing the Ag particle size and content.

2. Ag distribution across the coatings thickness

2.1 Ag morphology

The Ag/a-C coating morphology is firstly determined by TEM analysis. This study also allows to confirm the formation of a nanocomposite structure and to analyze the size distribution of the Ag nanoparticles. In order to avoid time consuming sample preparation, a thin film with about 40 nm in thickness is directly deposited in a TEM grid covered with a carbon film, which allowed to perform directly TEM in-plane view imaging. A high magnification TEM micrograph is shown in figure 30.

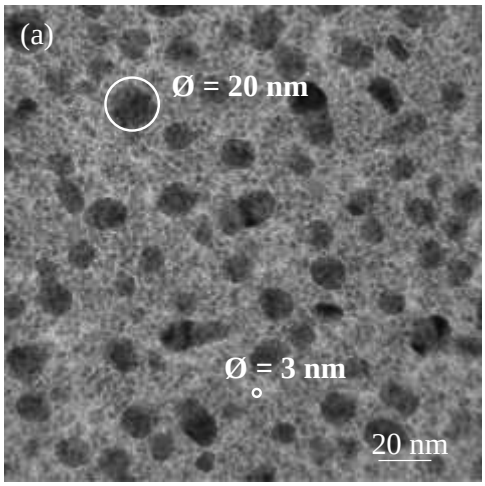

Figure 30 - TEM plane view micrograph of a 40 nm thick Ag/a-C coating

The Ag/a-C thin film has a nanocomposite structure with Ag nanoparticles embedded in an amorphous carbon matrix. A bimodal size distribution can be observed. In fact, the coating is composed by a high density of small Ag clusters with a size of about 2-3 nm, homogeneously distributed in the C- matrix, combined with a lower number but much bigger Ag nanoparticles with sizes of about 15 to 20 nm, which density is lower in relation to the density of the small clusters. From the TEM images, it is unclear how both particles groups are distributed in depth, across the coatings thickness.

SEM analysis is performed in the C1 and C2 coatings (samples nomenclature is provided in figure 27) to evaluate the clusters size distribution in the coatings. Therefore, cross-sectional and top view images are recorded either in secondary electrons (SE) and backscattered electrons (BSE) modes (in inset). The additional a-C layer on the top of

the Ag/a-C coating contributes for a better understanding of the Ag clusters growth on the coatings surface. The SEM cross sectional (Si substrates) and top view (SS316L substrates) micrographs of both coatings are presented in figure 31.

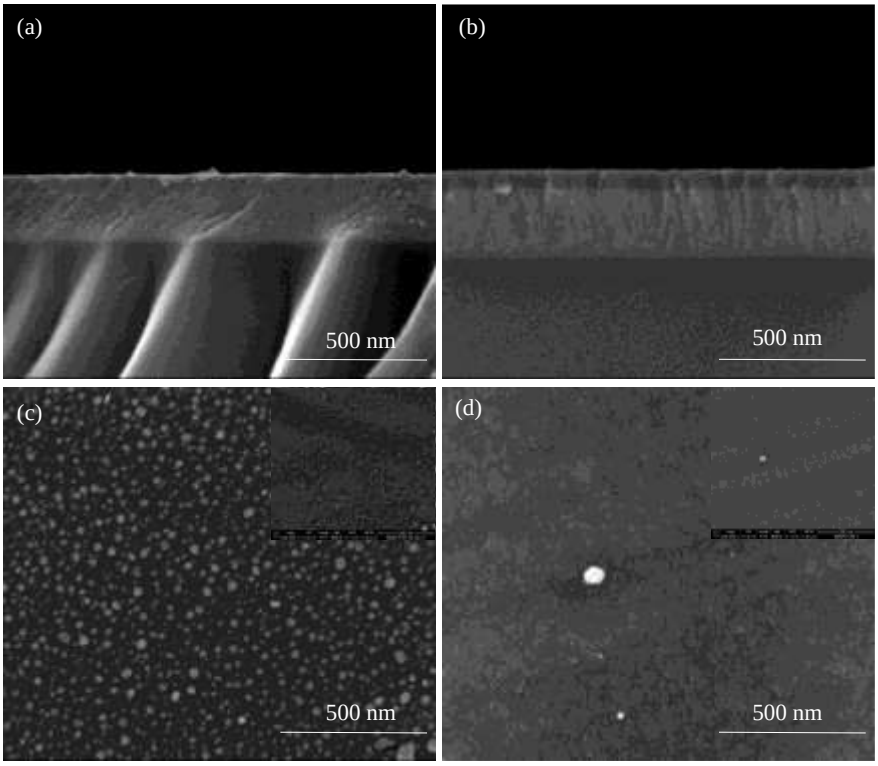

Figure 31 - Cross-sectional (a,b) and top view in SE and BSE in inset (c,d): (a,c) C1 and (b,d) C2

Regarding the cross sectional SEM micrographs of C1 and C2 coatings depicted in figure 31 (a) and (b), respectively, no evidence of Ag clusters is found, which suggests that the size of Ag clusters in the bulk is below the detection limit of SEM analysis. Conversely, the top view micrographs of the coating C1 (see figure 31 (c)) suggest the presence of silver nanoparticles. The SEM images recorded in SE mode allow to confirm that the nanoparticles are sitting in the coating´s surface, while the BSE images (inset of figure 31 (c)) allow to define these nanoparticles as Ag, due to their brighter appearance in relation to the darker, and consequently lighter, a-C matrix. The nanoparticles size distribution was evaluated by analyzing the SEM micrographs (figure 31 (c)) with *ImageJ* software; the major and minor dimensions were determined. Since the particles are not perfectly spherical the major and minor dimension are determined in the evaluation of the particles mean size. In the analysis only particles with a size above 10 nm are

considered, being determined that the mean size of Ag np is 19±6 nm (major dimension) and 14±4 nm (minor dimension). Since the top-view and the cross-sectional micrographs are performed with the same magnification (200,000×), it can be concluded that the particle sizes at the surface or in the bulk of the coatings are different. During the co-deposition of Ag and C, Ag atoms arrive to the growing film, being able to move in the surface, forming islands/clusters, until the surface is covered by the growing carbon matrix. However, in the end of the deposition, at the coating's surface, Ag growth is not restricted by any additional carbon layers and, thus, big clusters have time to be formed, a process which is thermodynamically favored by the reduction in the surface energy. This theory is well supported by the results achieved with the bilayer coating consisting of an Ag/a-C layer with 250 nm and an additional a-C layer of 75 nm. In this case, no Ag clusters are detected in the SEM top-view micrograph, meaning that the a-C layer deposited in the end of the Ag/a-C layer hindered the Ag atoms diffusion and clusters growing (see figure 31 (d)).

2.2 Ag grain size

Grazing incidence X-ray diffraction analysis is used for assessing the crystalline phases present in the coatings and also to determine the nanocrystals size across the coatings thickness. In order to obtain depth profile information, the grazing angle is varied between 0.1° and 0.7° and the results are depicted in figure 32 (a). The variation of X-ray intensity as a function of the grazing incidence angle is measured for two different values of scattering angles (2θ), 38.28° and 39.20° (figure 32 (b)). The standard value for the Ag (111) diffraction peak is 38.117° (ICDD 181730), thus, the value 38.28° allows to evaluate the evolution of Ag (111) diffraction from the entire range of Ag crystal sizes, while the peak at 39.20°, which only appears as a result of peak broadening associated with small crystallite size, allows to monitor the changes associated with small crystallite size. The analysis is performed on Ag/a-C nanocomposite coatings deposited on silicon substrate. Similar results were obtained for Ag/a-C coatings deposited with different thicknesses (250 nm and 1000 nm), being the results shown related with the C1 sample.

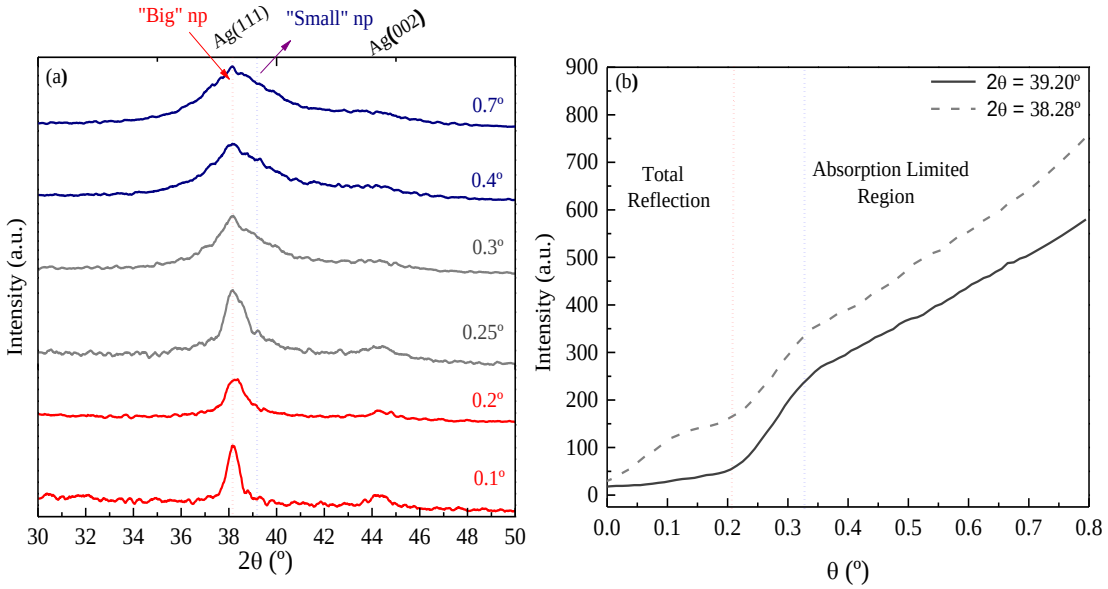

Figure 32 – (a) GIXRD patterns at different grazing angles and (b) variation of the diffraction intensity, at different grazing angles, for 2θ of 38.28° and 39.20°

The XRD patterns at different grazing angles show different structural features as follows: (i) at low incidence angles (0.1°-0.2°) the presence of narrow peaks is evident, (ii) at intermediate incidence angles (0.25°-0.3°) the peaks become broader and asymmetric, suggesting the overlapping of two diffraction peaks, one narrow as in (i) and another very broad placed on its right side, corresponding to bimodal size distribution and (iii) at high incidence angles (0.4°-0.7°) the peaks become broader and more symmetric , suggesting that the broad diffraction contribution becomes dominant and the information obtained from the pattern is mainly related to the small nanocrystals.

The XRD patterns are best fitted with pseudo-Voigt functions, which allow to correct the instrumental broadening and also to determine the FWHM caused by the crystallite size effects. The nanocrystals size for grazing incidence angles of 0.1° and 0.7° is determined according to Scherrer equation[7], giving values of 19 nm and 2 nm, respectively. It should be pointed out that besides the size effect the microstrains also contribute to line broadening; however, the higher order reflections are too weak to be measured, and, thus, the contribution of strain broadening could not be considered.

The variation of X-rays intensity at 2θ=39.20° as a function of α shows three different zones: (i) between 0° and about 0.2° (below the value of the critical angle of carbon (graphite) - 0.215°) the intensity is very low and almost constant, (ii) between 0.2° and 0.4° it increases sharply; (iii) for higher α angles, the intensity increases at a

lower rate. This trend has been reported being related with the penetration depth of X-rays at different grazing angles: at $\alpha<\alpha_c$ total external reflection occurs and the X-rays propagate in the surface, no diffraction takes place and only constant background intensity is detected; above $\alpha>\alpha_c$ the penetration depth increases sharply until the absorption limited regime is achieved (above 0.4°). The intensity variation is influenced by the penetration depth and also by the instrument configuration, for which the increase of incidence angle is accompanied by an increase in the density of photons per unit of area; thus, for higher incidence angles, the intensity is expected to increase due to the increase in photons density[8]. The graph of figure 2 (b) suggests a different behavior for the diffraction intensities at 2θ=38.28° and 2θ= 39.20° in total reflection regime (below the carbon critical angle). In fact, for 2θ= 38.28° the intensity has initially a much more pronounced increase in relation to the intensity at 2θ=39.20°. In the latter case only a very slight increase is observed attributed, as above mentioned, to the increase in the photons density with increasing α. This diverse behavior means that for 2θ=38.28°, absorption and diffraction are taking place even for incidence angles lower than the critical angle of carbon (0.2°). This behavior can only be explained if the diffraction activity is related to the Ag nanoparticles. However, the critical angle for Ag is about 0.4°. Then, this can only be interpreted if the Ag nanoparticles are sitting on the coatings surface. Assuming that Ag nanoparticles have a spherical shape, in spite of α<0.2° there are always incident X-rays with a wide range of angles in relation to the nanoparticles surface, giving rise to diffraction events. For α>0.2° information related with Ag-NP inserted in the coatings bulk starts to be detected. .Moreover, as previously mentioned the variation of 2θ =38.28° is related to all particle sizes, while the 2θ=39.20° is related to small crystallites.

The variation of intensity for different grazing angles together with the analysis of XRD patterns at different grazing angles allow to predict the Ag nanoparticles distribution along the coatings cross section, supporting the morphological results above presented. Hence, the Ag/a-C nanocomposite coating is composed of big Ag nanoparticles in the surface, with a mean size of 19 nm (as determined by Scherrer's formulae), which are the only visible for $\alpha<\alpha_c$ of carbon, and by smaller Ag nanoclusters with a mean size of 2 nm, which are present in the coatings bulk and, thus, only show their contribution for higher incidence angles (0.4° and 0.7°). The size of bigger nanoparticles is close to the size of the Ag-NP detected on the film surface by SEM, TEM

and GIXRD (about 19 nm) thus meaning that the bigger nanoparticles found in the surface are in fact single grains and not agglomerates. On the other hand, the size of the smaller nanoparticles is close to the size of the Ag-NP dispersed inside the carbon matrix already detected by TEM (about 2 nm). The bimodal size distribution of Ag nanoparticles was already observed by Chakravadhanula et al[9] in TiO_2 coatings studied with electron tomography. Conversely, the Ag nanocrystals distribution in a-C coatings determined by Matenoglou et al[10] through GIXRD analysis, with a similar methodology to the one used in the present work, showed that Ag was homogeneously distributed across the coatings thickness.

2. Coatings cross-sectional morphology

The morphology of C4 and C1 coatings deposited on silicon substrate is analyzed by SEM cross-sectional observation, (figures 33 (a) and (b) respectively).

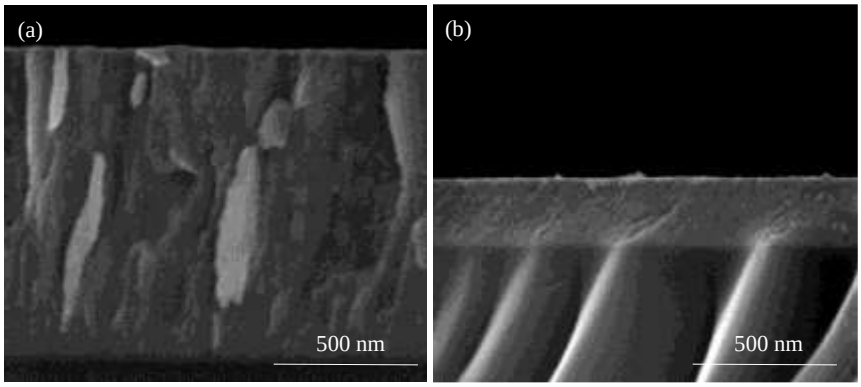

Figure 33 - SEM cross-sectional micrographs of coatings (a) C4 and (b) C1

Different morphologies are shown as a function of the coatings thickness: the thicker coating developed a columnar morphology, while the thinner one revealed a featureless morphology, typical of very dense coatings. Taking into account that both coatings are deposited with the same deposition parameters, excepting the deposition time, the differences in the coatings morphology can only be attributed to the coatings thickness. According to the model developed by Bales et al[6] (see figure 29) the height at which the "grooves" start to appear depend on the particles diffusion coefficient, which are determined by the deposition parameters, such as the temperature and the energetic particle bombardment. In fact the development of compact morphology in the thinner

coatings is somehow surprising if very low T_s/T_m is considered for a carbon coating, since the deposition was performed at RT and C has an extremely high T_m, close to 4300 °C (see sublimation point in figure 4). The variation of the coatings morphology with thickness has been previously reported[11,12] and it is mainly attributed to self-shadowing effects, which are enhanced as the film thickens. In fact, any small protuberance than can appear in the surface of the growing film is more exposed to the inclined flux of arriving atoms. If adatom diffusion is not very high, the adatoms will stay where they land, reinforcing the growing of the protuberance and promoting the development of a columnar morphology, a process which is as intense as the film is thickening.

3. Conclusion

The main goal of this chapter is the evaluation of the structure and morphology of the coatings, with the aim of determining the Ag distribution across the coatings thickness. The Ag morphology and particle distribution is accessed by TEM and SEM analysis, while the grain size distribution is determined through GIXRD analysis performed at different incidence angles. The size of Ag particles/grains in the surface and bulk of the coatings are summarized in Table 9.

Table 9 - Ag particle/grain size obtained by TEM, SEM and GIXRD in coatings bulk and surface

Characterization Technique	**Ag particle/Grain Size**	
	Bulk (nm)	**Surface (nm)**
TEM	20 + 2-3	
SEM	Not Detected	19±6 (major dimension) 14±4 (minor dimension)
GIXRD	2	19

The results obtained by the different techniques are consistent, being clear that the coatings show a bimodal size distribution with small Ag clusters (2-3 nm) embedded in the matrix and bigger Ag nanoparticles (about 20 nm) sitting in the coatings surface. Moreover, since XRD analysis allows to evaluate the crystal size, it was possible to conclude that the Ag surface particles visible in SEM are single grain. The GIXRD and

cross-sectional micrographs indicate that the variations in the coatings thickness do not influence the Ag particle size. The presence of bigger Ag surface particles is suppressed by the deposition of an additional carbon layer on the coatings top-surface, which suggests that the Ag growth in the bulk is restricted by the growing carbon matrix, while, at the surface, Ag particles are able to coalesce. Still, it remains unclear at which stage the surface particle growth occurs: after deposition or during coatings exposure to the atmosphere?

The SEM cross-sectional analysis of C1 and C4 coatings reveal that the coatings morphology changed by varying their thickness: the thinner coating is featureless while the thicker one shows a columnar growth. The differences are attributed to self-shadowing effects. The variation in coatings thickness allow to obtain Ag/a-C nanocomposite coatings with similar Ag particle size and contents and different morphologies.

References

[1] Ohring M. in *Materials science of thin films*, 2nd Edition, Academic Press, U.S.A.,2002.

[2] J. A. Thornton, *High rate thick film growth*, Annual Review in Material Science, 1 (1977) 239-260.

[3] R. Messier, A. P. Giri and R. Roy, *Revised Structure Zone Model for Thin Film Physical Structure*, Journal of Vacuum Science and Technology A, 2 (1984) 500.

[4] J.A. Thornton, D.W. Hoffman, *Stress-related effects in thin films*, Thin Solid Films, 171 (1989) 5-31.

[5] I. Petrov, P.B. Barna, L. Hultman, J.E. Greene, *Microstructural evolution during film growth*, Journal of Vacuum Science and Technology A, 21(5) (2003) 117-128.

[6] G.S. Bales and A. Zangwill, *Macroscopic model for columnar growth of amorphous films by sputter deposition*, Journal of Vacuum Science and Technology A, 9 (1991)145-149.

[7] P.Scherrer, N.G.W.Gottingen, Math.Phy 2 (1918) 96.

[8] Birkholz M. in *Thin film analysis by X-ray scattering*, Wiley-VCH, Weinheim, 2006.

[9] V. S. K. Chakravadhanula, C. K.T. Hrkac, V. Zaporojtchenko, T. Strunskus, F. Faupel and L. Kienle, *Surface segregation in TiO_2-based nanocomposite thin films*, Nanotechnology, 23 (2012) 495701 (7pp).

[10] G. Matenoglou, G.A. Evangelakis, C. Kosmidis, S. Foulias, D. Papadimitriou, P. Patsalas, *Pulsed laser deposition of amorphous carbon/silver nanocomposites*, Applied Surface Science, 253 (2007) 8155–8159.

[11] R. Messier and R.C. Ross, *Evolution of microstructure in amorphous hydrogenated silicon*, Journal of Applied Physics, 53 (1982) 6220-6225.

[12] M.K. Puchert, P.Y. Timbrell, R.N. Lamb and D.R. McKenzie, *Thickness dependent stress in sputtered carbon films*, Journal of Vacuum Science and Technology A, 12 (1994) 727-732.

Chapter V

Stability

The preliminary work developed under the scope of this thesis allowed to observe that Ag/a-C nanocomposite coatings are not stable even in atmospheric conditions, being found that Ag tends to segregate to the coatings surface. The coatings thermodynamical stability is one of the most important requirements in any functional application, thus, the understanding of the coatings stability is a fundamental aspect that must be precisely controlled in order to guarantee the applicability of these nanocomposites. Therefore, the evaluation of the coatings stability, as one of the major concerns of the thesis, is the core of this Chapter.

The first concern was to understand the mechanism of Ag mobility in the a-C matrix. The work developed in Chapter III allowed to draw a model which predicts the depth from which Ag nanoparticles move towards the coatings surface (see figure 19). It is proposed that only Ag nanoparticles from a few nanometers below the surface are responsible for the formation of the Ag rich surface layer. Nevertheless, a more detailed study is necessary. Firstly, we wanted to understand if Ag nanoparticles really diffuse from the entire coating thickness or only from the first nanometers below the surface. For this study, two different nanocomposite coatings with different thicknesses / morphology (C1 and C4) are stored in atmospheric conditions and their surface is monitored by SEM analysis along time, while the chemical composition depth profiles are accessed by GDOES analysis. Other important question is to understand if Ag moves in free spaces inside the coating, such as column boundaries, or if the Ag nanoparticles would be able to move through the carbon matrix. In order to clarify this aspect, a compact a-C layer was deposited over Ag nanoparticles, deposited by PGC (sample C3), and the sample is monitored in a TEM apparatus during an *in-situ* heating experiment.

After understanding the fundamental aspects about the Ag mobility in a-C coatings, the study is focused on the driving force for the occurrence of this process. The particles agglomeration or coalescence is driven by several external factors, namely the temperature and the humidity, as reviewed in this chapter´s introduction (section 1). Since the envisaged final application for these coatings is antibacterial surfaces, e.g. medical devices, indwelling implants, food packages, working at room or body (about 37°C) temperatures, this factor is not critical. Conversely, humidity can play an important role since all those devices work in environments with some degree of humidity. In this sense, taking into account that Ag was found to be unstable even in room temperature conditions, the influence of humidity in Ag particles mobility was accessed. The sample C4 is stored at different levels of humidity ranging from values below 20% up to 100%. As reviewed in the thesis State of the Art, a phenomena known as metal whiskering has been observed for more than 50 years although not completely understood until now. Several models have been proposed for explaining the whiskering phenomenon, being the most consensual the one based on the reduction in the stress state. Stresses can exist as residual, due to the processing method of the material, or developed due to phase transformations, as for example the oxidation. In this sense, the influence of humidity on the coatings oxidation was accessed by XPS and EDS analysis, while the changes in the residual stress are qualitatively measured by comparing the changes in the curvature of the coated substrates after having been submitted to ageing tests. In order to determine if Ag growth occurred through coalescence or agglomeration, GIXRD and TEM analyses of Ag fibers are performed. A schematic representation of the work flowchart adopted in this Chapter is shown in figure 34.

The selection of GDOES technique for depth profiling analysis is based on the previous experience acquired during the analysis of Ag-TiCN coatings by different depth-profile techniques, namely XPS, Rutherford Backscattering (RBS) and GDOES, which allowed to determine the chemical composition across the coatings depth. GDOES showed a very good resolution in the first nanometers. The good depth resolution combined with a fast analysis, made GDOES the selected technique for depth profiling analysis.

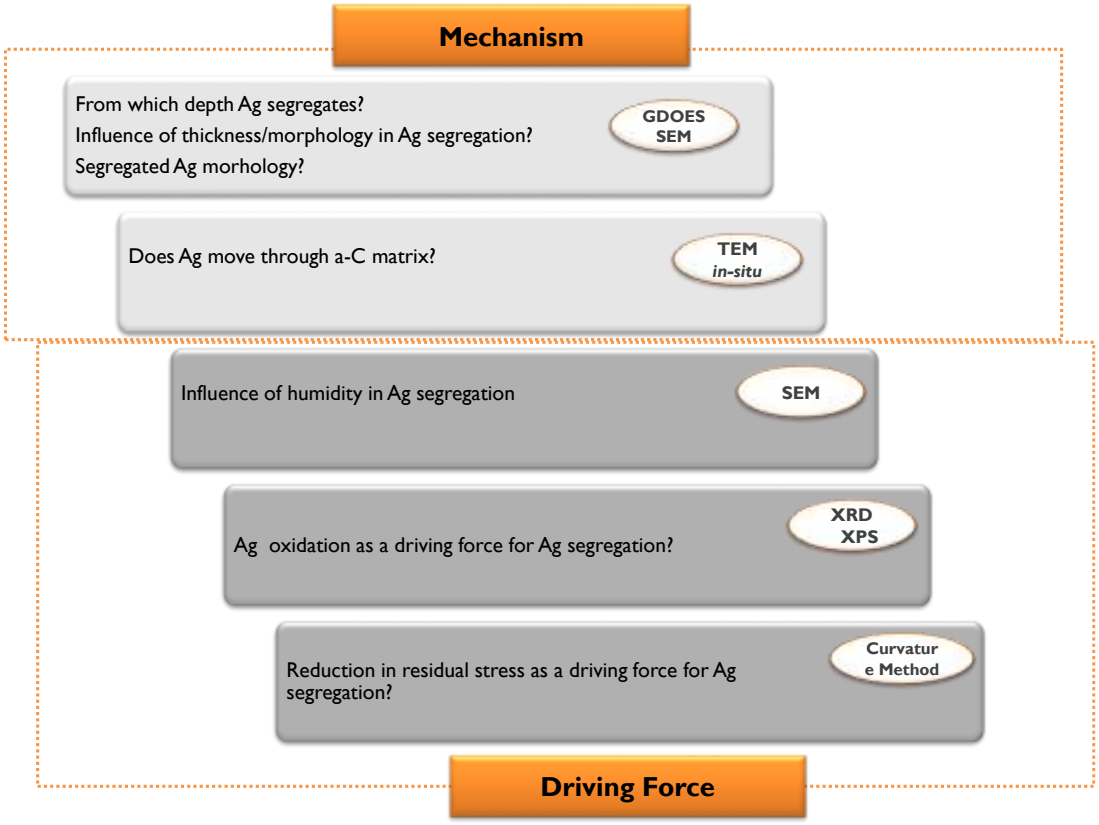

Figure 34 - Work-flowchart for Chapter V

The work developed in Ag-TiCN coatings depth profiling resulted in one published paper, prepared during this PhD work:

- R. Escobar Galindo, N.K. Manninen, C. Palacio and S. Carvalho, *Advanced surface characterization of silver nanocluster segregation in Ag–TiCN bioactive coatings by RBS, GDOES, and ARXPS*, Analytical and Bioanalytical Chemistry (2013) 405:6259–6269. I.F. 3.436.

The work developed in this Chapter resulted in one published paper:

- Noora Kristiina Manninen, Ramon Escobar Galindo, Sandra Carvalho, Albano Cavaleiro, *Silver surface segregation in Ag-DLC nanocomposite coatings*, Surface and Coatings Technology 267 (2015) 90-97. I.F. 1.998.

1. Nanoparticles growth mechanisms and kinetics

1.1 Particles growth mechanisms

Surfaces are characterized by several physical properties namely surface energy (Gibbs free energy per unit area) which is a direct consequence of the presence of dangling bonds which results in inwardly directed force that reduces the bond distance of surface and sub-surface atoms in relation to the bulk atoms. The surface energy is defined as the energy required to get the atoms back to its original position, which is given by:

$$\gamma = \frac{1}{2} N_b \varepsilon \rho_a \tag{5.1}$$

where N_b are the number of broken bonds, ε the bond strength and ρ_a the density of surface atoms. As the surface energy is proportional to the density of surface atoms, it increases as the particle size decreases; in case of nanoparticles with sizes below 5 nm the percentage of surface atoms is above 50%; thus, a huge increase in the surface energy is observed as the nanoparticles size is decreased. The surface chemical potential is influenced by either the surface energy or the particle curvature, being the value for spherical particles given by.

$$\Delta\mu = 2\gamma \frac{\Omega}{R} \tag{5.2}$$

where $\Delta\mu$ is the chemical potential of an atom in a spherical surface of radius R with respect to a flat surface; Ω is the atomic volume and γ the surface energy. The above equations allow to comprise the increase of nanoparticles surface energy and chemical potential with the reduction of particles size, which results in a higher instability. Several mechanisms allow for the reduction of surface energy, namely: the physical and chemical adsorption on solid surfaces; the restructuring of the crystalline structure (facets with low index are exposed to the outer surface in order to reduce the surface energy, according to Wulff construction) and the reduction of the overall surface area[1,2].

The particles agglomeration is commonly observed in powder technology, which was introduced as a field of science in 1957 by Ralph Rumpf, and largely studied ever since[3,4]. This phenomena is of great importance for powder technology and nanotechnology, since the agglomeration or binding between solid particles assume a great importance during the production and usage of solid particles, strongly influencing the functional properties. The binding mechanisms between solid particles were firstly classified and divided by Rumpf and co-workers; five major groups were identified and divided in several sub-groups, as summarized in Table 10 and figure 35.

Table 10 - Agglomeration mechanisms[3]

Group		Sub Groups	
I.	Solid Bridges	1.	Sintering 2. Partial melting 3.Chemical reaction 4. Hardening binders 5. Drying (recrystallization of dissolved substances or deposition of colloidal particles)
II.	Adhesion and Cohesion Forces	1.	Viscous binders 2. Adsorption layers
III.	Surface Tension and Capillary Pressure	1.	Liquid bridges 2. Capillary pressure
IV.	Attraction Forces between Solids	1.	Molecular forces 2. Electric forces 3. Magnetic forces
V.	Interlocking Forces		-

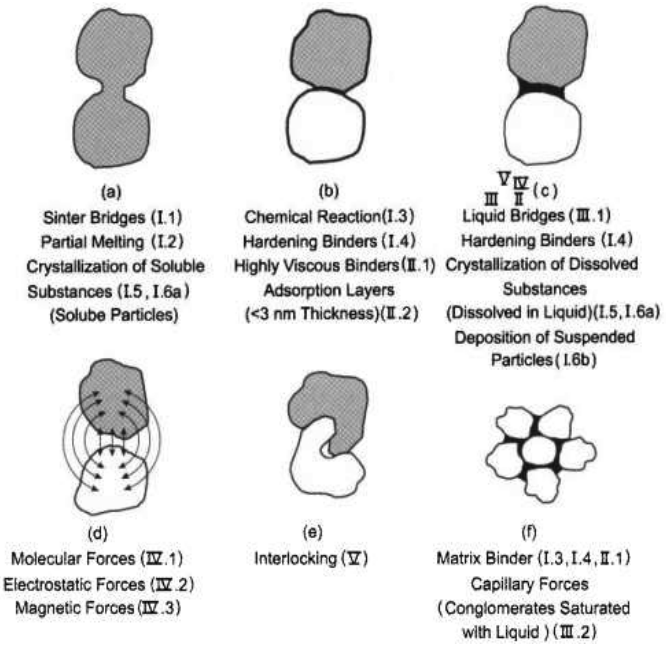

Figure 35 - Representation of binding mechanisms of agglomeration[3]

The binding mechanism may lead to the combination of individual nanoparticles into larger particles (coalescence) or the formation of larger entities associated by chemical bonds and physical attraction forces (agglomeration), which are schematized in figure 36.

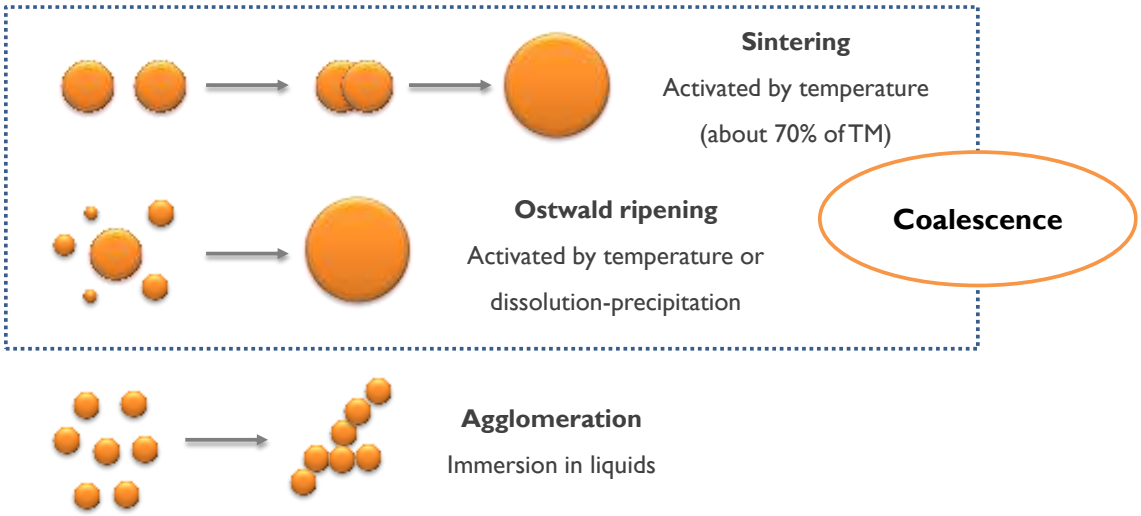

Figure 36 - Particles growth mechanisms and summary of required conditions

The coalescence process occurs mainly through two different processes: (i) sintering, which generally occurs at high temperatures (about 70% of materials melting point) and (ii) Ostwald ripening, which occurs at a wide range of temperatures or at low temperatures if particles are immersed in a solvent where they can be partial or totally dissolved. The sintering process can be easily avoided provided that the processing and usage temperature is low. This process involves several mechanisms, such as: (i) solid state diffusion (surface diffusion at low temperatures, volume diffusion at intermediate temperature and cross-grain boundary diffusion at high temperature); (ii) evaporation-condensation when the vapor pressure is appreciable and (iii) dissolution-precipitation when the solid is dispersed in a liquid where it is partially soluble. Sintering does not require the presence of particles with distinct sizes and it occurs through the particles approximation followed by neck formation and growth until the particles are completely coalesced forming a unique entity. Ostwald ripening process involves the growth of larger particles at the expense of smaller ones in a process where atomic diffusion from smaller particle to the larger one is present. Smaller particles have higher solubility and lower vapor pressure, thus, they tend to dissolve (in liquids) or evaporate (when exposed to higher temperatures) more easily than larger ones. In the case of heating or

immersion in solutions there will be a net flux of atoms from the smaller particles to the larger ones[1,2].

When nanoparticles are immersed in liquids they easily agglomerate forming weak van der Waals chemical bonds, which are only significant at small distances. The Brownian motion ensures that particles collide. Therefore, the combination of Brownian motion and van der Waals forces result in the agglomeration of nanoparticles. Nevertheless, it should be pointed out that when particles are immersed in liquids they tend to generate surface charges through different mechanism: surface ionization (metallic nanoparticles) or adsorption of ions (ceramic nanoparticles). The presence of the surface charges results in the segregation of opposite charged species (designated as counter ions) forming a double electric layer, generating an electric potential in the particles surface (where the outer layer´s (slip plane´s) potential is known as zeta potential) dependent on the valence state and the concentration of ions in the solvent. The presence of this electrical double layer generates a repulsive force, which prevents the particles agglomeration. Hence, the particles agglomeration in liquids is a balance between attractive and repulsive forces. This mechanism is very common when nanoparticles are immersed in solutions and the prevention of the particles agglomeration represents one of the main concerns related with nanoparticles production through chemical methods[1,5].

Another important agglomeration mechanism is associated with the capillary forces which arise from the presence of liquid bonds between two particles. The condensation of water vapor present in the air is enough to create liquid bridges. This phenomenon, known as capillary condensation, has been studied by Lord Kelvin to explain the moisture retention in vegetables, oatmeal or biscuits. Another important parameter is the wettability, since more hydrophilic surfaces retain more condensed liquid. The capillary forces increase the cohesion between the particles at the point of contact promoting their agglomeration. Then, the formation of solid bridges can take place (mechanism I.6) if the recrystallization of the dissolved particles occurs during drying. It can also be observed in the case of colloidal particles drying, where the reduction of liquid bridges and the pressure caused by the liquid´s surface tension compacts the colloidal particles[1,2,3,4].

1.2 Diffusion

Adolf Fick introduced the concept of diffusion coefficient and suggested a linear response between the concentration gradient and the diffusion based on the idea that diffusion is a process that leads to the equalization of concentrations. Fick´s Laws were then created. These laws were built based on empirical facts, although they continue to be widely used presently and, possibly, the first idea that comes up to our minds when the subject is diffusion is that concentration equalization is the driving force for the diffusion processes. Nevertheless, the thermodynamically correct driving force is the chemical potential gradient. In fact, not all thermodynamically stable diffusion processes lead to concentration equalization. For example, this phenomenon is commonly observed in metallic materials, where the diffusion of solute atoms occurs from sites of uniform composition to the interfaces, such as free surfaces, grain boundaries and defects, leading to the reduction of the total Gibbs free energy of the system. This process is named as segregation.

Einstein related the particles displacement to their diffusion coefficient based on the Brownian motion, a phenomena characterized by the random walk of particles which is dependent of their Boltzmann distribution of energy. Therefore, the particles are always subject to thermal motions of a statistical nature. The Einestein-Smoluchowski relation for one dimensional diffusion is given by:

$$D_x = \frac{x^2}{2t} \tag{5.3}$$

Where D_x is the diffusion coefficient along x direction, x the particles displacement and t the time associated with the displacement x.

The diffusion processes are thermally activated and the temperature dependence of diffusion coefficients is frequently found to obey the Arrhenius formula given by:

$$D = D^0 exp\left(-\frac{\Delta H}{k_B T}\right) \tag{5.4}$$

where T denotes the absolute temperature k_B the Boltzmann constant, D^0 the diffusivity pre-factor and ΔH, also represented by Q or E_a, the activation energy, being the later ones known as activation parameters. The physical interpretation and values of the activation parameters depend on the diffusion mechanism, type of diffusion and lattice geometry[6].

1.3 Ag nanoparticles growth mechanism and kinetics in free surfaces activated with temperature

In his PhD work, M. Asoro[7] determined the mechanisms and the kinetics for sintering and coalescence of Ag and Pt nanoparticles deposited in free carbon surface through *in-situ* TEM analysis. The effect of the particle size, the sintering temperature and the presence of carbon coatings in the nanoparticles surface on those processes were evaluated. Two main sintering mechanisms were found to occur: (i) surface Ostwald ripening, at high temperatures and (ii) particle migration and coalescence. The initial contact between particles, which represents the initial stage of coalescence, was mediated by different process: (i) movement of the particles towards each other, (ii) migration of single atoms and small clusters on the substrate towards the neck region and (iii) substrate motion promoted by the differential heating caused by the electron beam. A sequence of *in-situ* TEM heating micrographs obtained by the author are shown on figure 37, where the sintering of two 15 nm Ag nanoparticles was monitored.

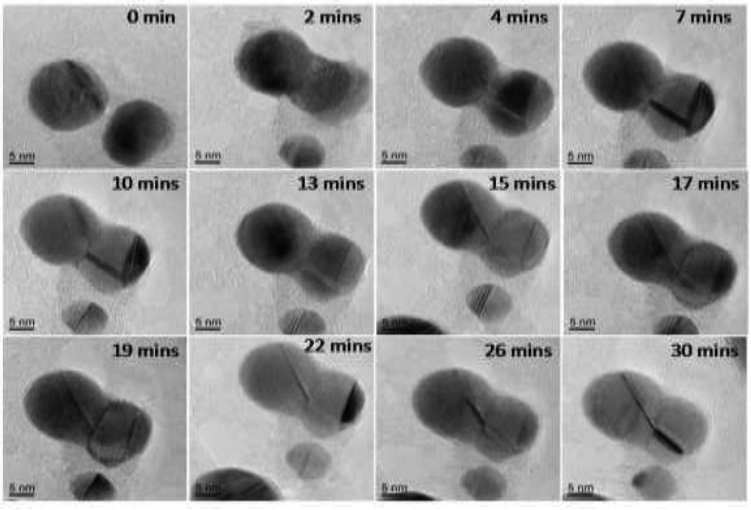

Figure 37 - Sequence of in-situ TEM micrographs of two 15 nm Ag nanoparticles sintering at 200°C[7]

Two Ag np with 15 nm, at a distance of about 2-3 nm, were initially observed as well as a third Ag np located at about 5 nm. The neck formation was observed only 2 minutes after the heating at 200°C. The live FFT´s (not shown) suggested that the diffraction spots changed from frame-to-frame, which indicated that particle rotation was mediating the particles movement, during the sintering. However, the occurrence of mass transfer by diffusion of atoms or small clusters could not be detected due to resolution limitations. Still, during the PhD work developed by M. Asoro, the author performed *in-situ* heating in STEM where evidence of mass transfer was found to occur[7].

The Ag diffusion coefficient (D) has been determined in several experimental and theoretical works. The reported values show a huge discrepancy, which are attributed to the influence of different parameters on this constant, namely:

i. Diffusion mechanism;
ii. Interaction with substrate;
iii. Presence of contamination in the nanoparticles surface;
iv. Atmosphere composition;
v. Nanoparticles size;
vi. Temperature.

As previously mentioned the nanoparticles diffusion mechanism can occur through Oswald ripening, which involves atoms motion from smaller to bigger particles or cluster migration, which involves the particles movement as a "whole", induced by particle internal vibrations or substrate vibration. This mechanism depends on the interaction with the substrate, as previously mentioned. For instance, Jensen and co-workers have evaluated the growth of metallic clusters on different substrate materials, with diverse roughness and surface finishing states. The diffusion coefficients reached values in the order of 10^{-8} cm^2/s at room temperature, when clusters sited on perfect substrates (with no defects or roughness) with high misfit (generally carbon). However, the same clusters showed a D several orders of magnitude lower (~10^{-15} cm^2/s) when they epitaxially accommodated to the substrate. The presence of defects could trap the clusters, lowering their diffusion coefficient. The diffusion mechanisms were also different in both cases, in carbon layers particle migration was likely to occur, while in substrates made of the same metal that nanoparticles, Oswald ripening was more likely to occur[8].

Asoro et al[7,9] has demonstrated also by *in-situ* heating TEM experiments that the presence of a carbon layer on the Ag nanoparticles surface decreases their diffusivity; thus, the sintering environment played a very important role, since the presence of oxides or adsorbed species on the nanoparticles surface could retard the sintering process. The diffusion coefficient of 12 nm – 40 nm Ag nanoparticles between 200°C and 400°C was evaluated to be in the range from $4.2x10^{-16}$ cm^2/s down to $1.1x10^{-20}$ cm^2/s, clearly below other reported values. This effect was attributed to the presence of the carbon layer in the nanoparticles surface. In fact, in another experience[7] the diffusion coefficient of the Ag nanoparticles without stabilizers on their surface, deposited in an Ag wire, was also evaluated, being found a decrease of two orders of magnitude in the case of 40 nm sized particles.

The temperature dependence of the diffusion coefficient is frequently found to obey to the Arrhenius formula given in Equation 5.2. Nevertheless, it should be pointed out that the activation parameters strongly depend on the diffusion mechanism; for instance, Papanicolaou et al[10] determined the activation parameters for Ag single adatoms on Ag (100) and Ag (111) surfaces by molecular dynamic simulations, and they found that for (100) surface the diffusion mechanism below 600K occurred through bridge hopping, with activation parameters of $D^0=1.4x10^{-3}$ cm^2/s and $\Delta H=0.43$ eV, while above 600 K the diffusion occurred through an exchange mechanism with $D^0=40x10^{-3}$ cm^2/s and $\Delta H=0.59$ eV. These values are well consistent with the experimentally determined activation parameters at low temperatures reported by Antczak[11]. The activation parameters and the transition temperatures were found to be quite different in (111) surfaces. If these values are extrapolated to room temperature conditions, then, the D_s values are in the order of $8.83x10^{-11}$ cm^2/s, a value much higher than the surface diffusivities reported by Pai et al[12]. The authors determined experimentally the diffusion coefficient of electron beam deposited Ag islands on sputtered Ag (100) surfaces, by scanning tunneling microscopy (STM) at room temperature, and the reported D_s was 3-$6x10^{-18}$ cm^2/s. A similar study was performed by Wen et al[13], where they reported a value of $D=10^{-17}$ cm^2/s.

In this sense, both activation parameters and diffusion constants must be very carefully used and preferentially measured for specific types of materials and atmospheric conditions, whenever possible

2. Mechanism of Ag diffusion through Ag/a-C coatings

2.1 Evolution of Ag/a-C coatings morphology with time

The coatings surface is monitored monthly during a period of 5 months by SEM top-view analysis. The SEM micrographs of C4 and C1 coatings, deposited on SS316L substrates, recorded 2 weeks (named as "as-deposited") and 5 months after the deposition process are shown in figures 38 and 39, respectively.

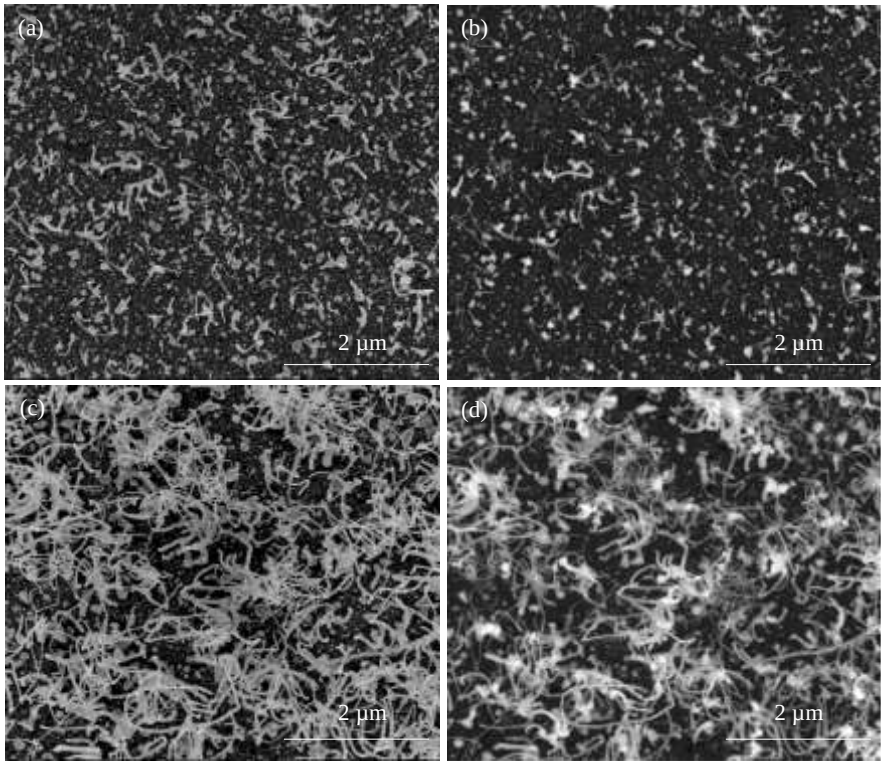

Figure 38 - SEM top-view micrographs of coating C4 recorded shortly after deposition in (a) SE mode, (b) BSE mode and 5 months after deposition in (c) SE mode and (d) BSE mode

The coating surface shown in figures 38 (a) and (b) is composed of (i) spherical Ag clusters, (ii) Ag aggregates and (iii) Ag nanofibers with a thickness of about 10 nm. The SEM micrograph of the same sample recorded after 5 months revealed that the coating´s surface is mainly composed of Ag fibers, although some clusters and aggregates could still be found below the fibers (see figure 38 (c) and (d)). Since the information obtained in SE mode is related to the first nanometers below the surface, the results suggest that silver is segregating to the coatings surface forming Ag fibers. The brighter appearance of the fibers in BSE micrographs suggest that they are composed, in fact, by silver. It should be pointed out that the first SEM micrographs were recorded 2 weeks

after coatings deposition, thus, the fibers visible in the "as-deposited" coating might be associated with the coatings ageing and not to the growth of Ag fibers during the deposition process itself. This topic will be discussed later in the section 3.

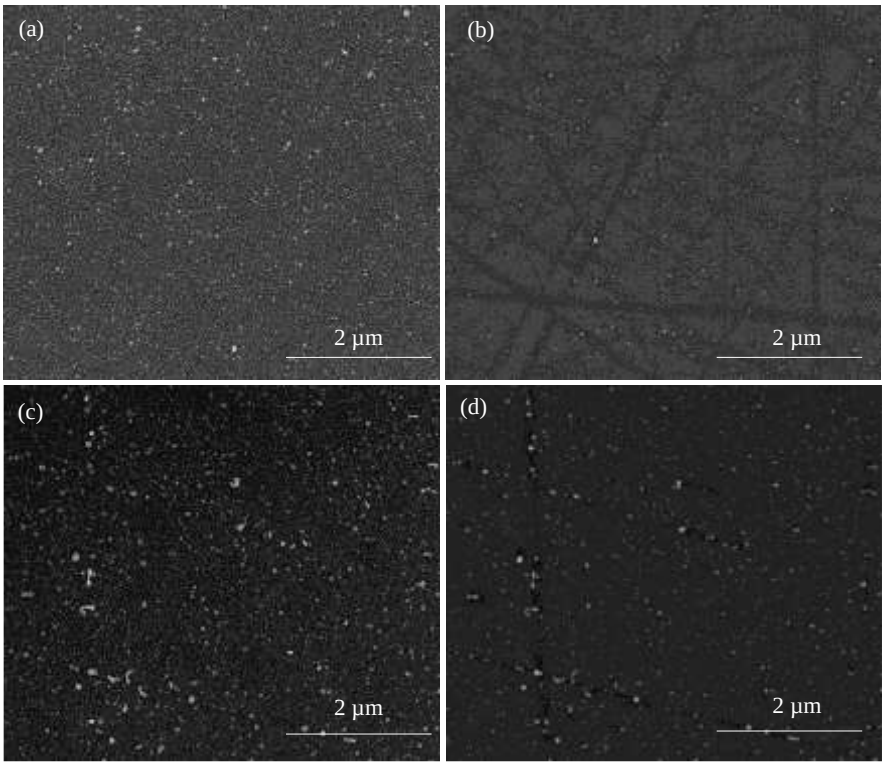

Figure 39 - SEM top-view micrographs of coating C1 recorded shortly after deposition in (a) SE mode, (b) BSE mode and 5 months after deposition in (c) SE mode and (d) BSE mode

As previously shown (figure 30) the surface of C1 coating is composed by Ag nanoparticles with mean size of 19±6 nm (major dimension) and 14±4 nm (minor dimension). The analysis of SEM micrographs of the as-deposited (a), (b) and aged surface (c), (d) showed that this coating is more stable with time in relation to the thicker nanocomposite. In fact, only small variations could be observed after 5 months, as follows: (i) the number of Ag aggregates increased with time and (ii) a few Ag fibers are merging from the bulk, but in a much lower extension than in the C4 coating.

The variation of area coverage over time for both coatings is shown in figure 40 (a), together with the statistical analysis of Ag nanoparticles area variation for the C1 coating. Both analyses were carried out on the SEM top-view micrographs with *ImageJ* software.

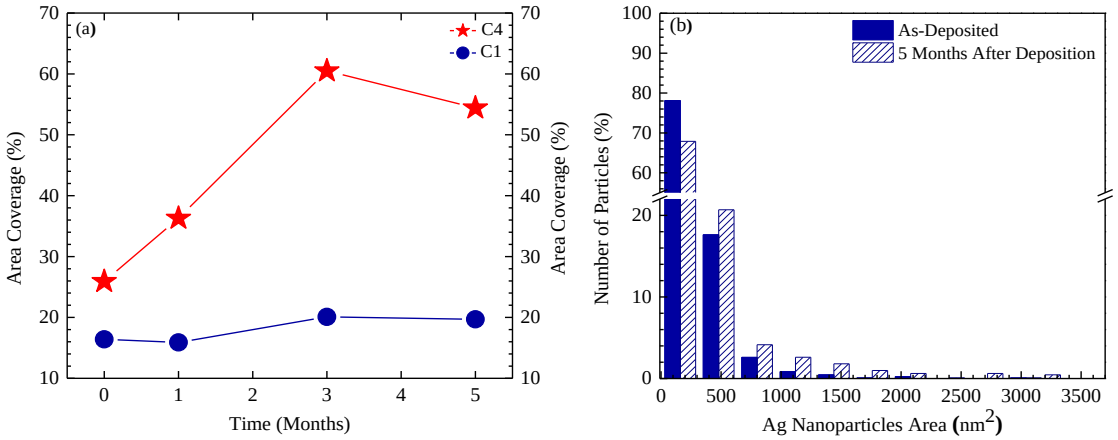

Figure 40 – (a) variation of area coverage with time for coatings C4 and C1 and (b) variation of Ag-NP size distribution in C1 coating

The area coverage variation suggests that the amount of Ag in C4 coating´s surface increases with time (figure 40 (a)) with an increase from 26 % to 60 % for the first 3 months, remaining constant thereafter. Regarding the thinner Ag/a-C coating, the area coverage remains approximately constant with time, showing a value of about 18 %. The mean particle size remains constant with time for the C1 coating, although the size distribution got wider, as can be shown in the histogram of figure 40 (b), which may be attributed to the coalescence of surface Ag nanoparticles.

GDOES is performed to analyze the changes in the chemical composition depth profile with time of the coatings aged in atmospheric conditions during a period of 6 months (figure 41 (a) for C4 and (b) for C1). It should be pointed out that, once again, the "as-deposited" coatings correspond in fact to the coatings analyzed 2 weeks after deposition.

Both as deposited C4 (see figure 41 (a)) and C1 (figure 41 (b)) coatings show an enrichment of Ag in the top surface (first 10 nm – see the insets of figures 41 (a) and (b)) followed by a constant Ag content along the coatings depth, with an average value of 18 at.%. Since no depletion zone is observed below the silver rich surface the Ag enrichment cannot be attributed to silver surface segregation as previously reported by Escobar Galindo et al[16] in AgTiCN coatings. This Ag surface layer should be related to the presence of Ag nanoparticles on the surface which, during the GDOES analysis, are preferentially sputtered / analyzed before the Ag/a-C coating.

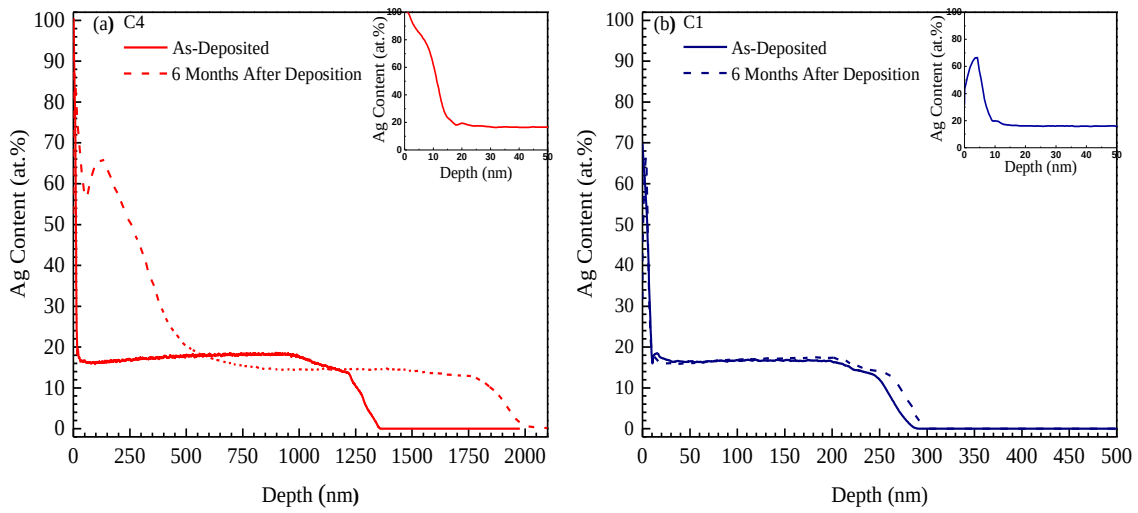

Figure 41 - GDOES Ag depth profiles of as-deposited coatings and coatings aged in atmospheric conditions during 6 months (a) C4 and (b) C1; in inset the first nanometers from the surface are shown

Regarding the GDOES depth profile of C4 coating, the depth profile changed with time: (i) an Ag rich surface layer was formed and (ii) the Ag content in the bulk decreased from 18 at.% to 14 at.%. This decrease is uniform across the entire coating thickness which suggests that Ag is segregating to the surface from the entire coating thickness. A different behavior was observed in C1 coating, which revealed to be stable along time, as suggested by the depth profiles shown in figure 41 (b).

It should be pointed out that the GDOES technique estimates the thickness taking into account the theoretical density of the elements[15]. In case of the Ag/a-C sputtered coatings, several factors can introduce errors in the thickness estimative, as follows: (i) it is well established that densities of sputtered coatings do not correspond to the theoretical ones; (ii) a-C coatings present a very complex structure (which consists of a mixture of sp^1, sp^2 and sp^3 bonds), with the accurate density being very difficult to be calculated[16]; (iii) after Ag segregation, the top layer consists of silver with a high number of holes and pores (nanoparticles + whiskers), being the global density far from Ag density. Therefore, the thickness given in GDOES analysis can show strong discrepancies in relation to the real analyzed thickness. This is the reason why the thickness of both C4 and C1 coatings is different from the one measured by SEM. Moreover, the errors associated with the evaluation of thickness by GDOES also explains why the integrated amount of Ag is different in C4 coating in the as-deposited and aged states. Nevertheless, the GDOES combined with the SEM analyses allow to

prove either the Ag surface segregation in thicker nanocomposite coating or the fact that Ag is segregating from the entire coatings thickness and not only from the first nanometers below the surface, as proposed in the first developed model discussed in Chapter III (see figure 19).

The different behaviors observed for thick and thin coatings are attributed to the coatings morphology, according the SEM cross-sectional micrographs presented in Chapter IV, with the thicker coating showing a columnar appearance while the thinner one is featureless and compact. Therefore, the Ag surface segregation is related with the coatings and diffusion barrier layers morphology, as reviewed in the State of the Art, being found that Ag diffuses through open spaces, like column boundaries. However, the Ag surface segregation was found to occur at several hundred degrees and not at room temperature conditions as in the present work.

2.2 Ag mobility in a-C matrix

In order to get a better understanding about the influence of a-C layer on the Ag nanoparticles mobility, an Ag nanoparticle layer is deposited by PGC on a TEM grid with a carbon foil, which is thereafter covered with a sputtered thin a-C layer with a thickness of about 30 nm, to evaluate its effect on the Ag mobility. The sample is analyzed by TEM with an *in-situ* heating experiment. The a-C layer morphology/topography was analyzed through atomic force microscopy, being the AFM 2D and 3D images depicted in figure 42 (a) and (b), respectively.

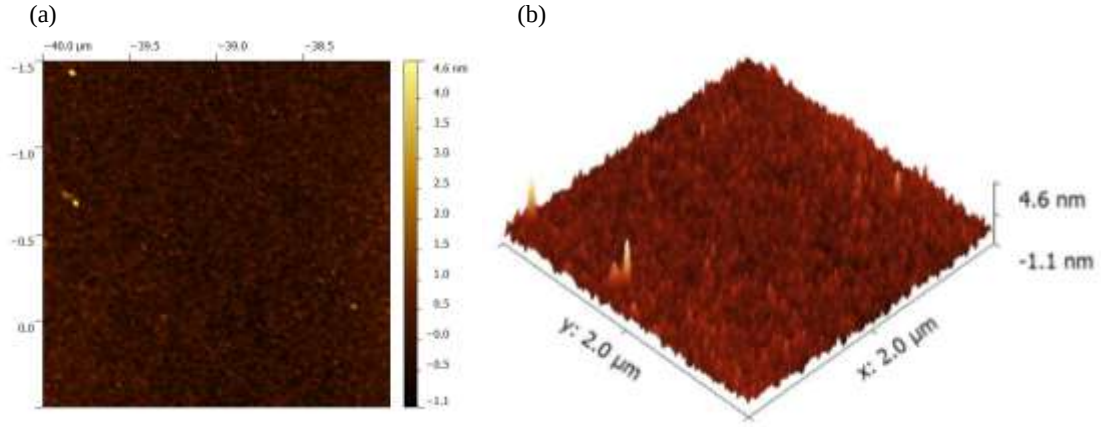

Figure 42 – a-C (30) layer topography obtained in AFM (a) 2D view and (b) 3D view

The AFM images indicate that the coatings present very smooth surface with an average roughness of 0.4 nm. The presence of some higher protrusions is also find, which might be related to the presence of surface contaminations in the silicon substrate. The presence of smooth surface indicates that the coating grows featureless with a very compact morphology[17]. This was expectable taking into account the discussion provided in the previous Chapter. The heating cycle for the TEM *in-situ* experiment is plotted in figure 43 and the sequence TEM micrographs recorded at different times and temperatures provided in figure 44.

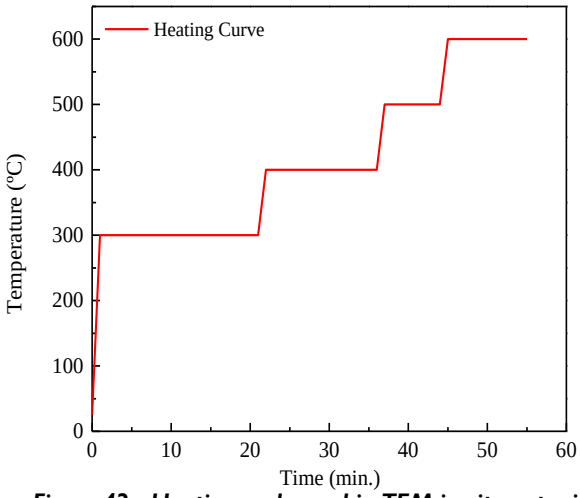

Figure 43 - Heating cycle used in TEM in-situ experiment

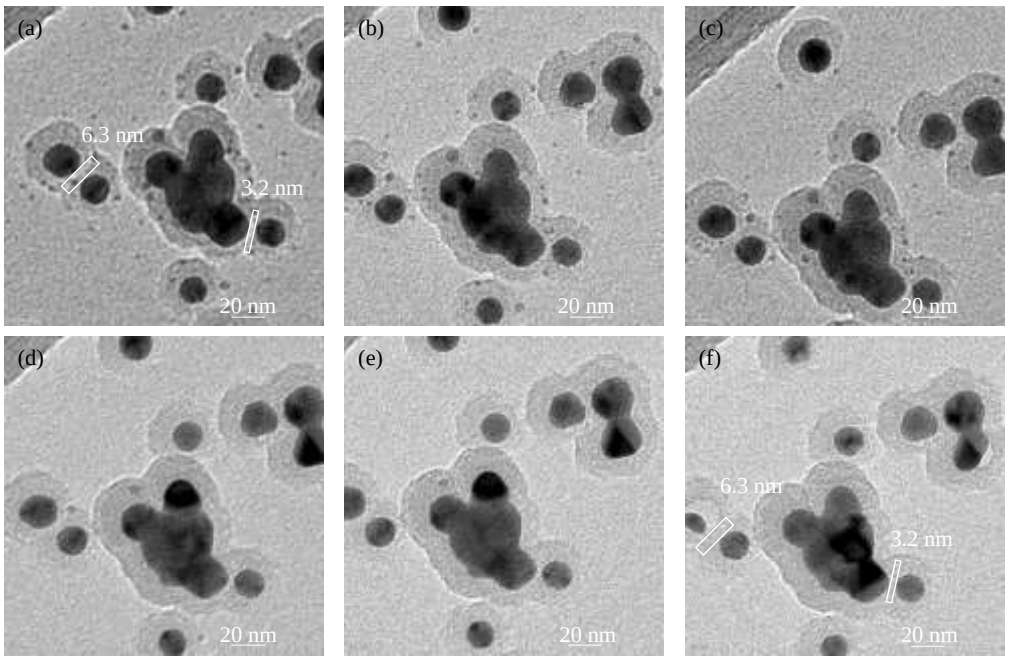

Figure 44 - TEM micrographs recorded at (a) 3min at 300°C, (b) 7 min at 400°C, (c) 14 min at 400°C, (d) 3 min at 500°C, (e) 5 min at 500°C and (f) 11 min at 600° (the distance between adjacent particles is provided)

In the first TEM micrograph Ag agglomerates with several hundreds of nanometers are observed, combined with Ag nanoparticles with 15 nm to 20 nm, separated by a distance of about 6 nm. A smaller Ag nanoparticle with about 15 nm is find close to the Ag aggregate at a distance of 3 nm. In addition numerous Ag nanoparticles 1-5 nm size are observed around the Ag agglomerate. The evolution of the micrographs clearly demonstrates that no particle coalescence is occurring. This is completely different from what was observed by Asoro[7] in free Ag nanoparticles deposited in carbon layers without additional barrier layers, as previously described. As it was referred, Ag nanoparticles 15 nm of diameter, separated by a distance of 2-3 nm, started to coalesce at 200°C only after 2 minutes, and one Ag particle located at 5 nm, also started to move towards the coalesced particles. Although, the initial size and separation of the particles studied by Asoro[7] were different from those of this study, it can be clearly observed that the particles remain completely immobile when an a-C layer is added.

The only visible change is the particles sublimation, occurring at 500°C (see figure 44 (d)) for the small particles surrounding the bigger ones, while these only started to sublimate at 600°C. It should be pointed out that the occurrence of Oswald ripening cannot be discarded since the performed analysis does not have atomic resolution; moreover, if this mechanism is present it would lead to an increase in the bigger Ag particles size and the reduction of smaller particles; nevertheless, if the amount of diffusing atoms is low the changes should not be visible at these magnifications. In conclusion, the comparison of free Ag nanoparticles studied by Asoro, with those covered with an a-C layer, clearly demonstrates that the presence of this layer is inhibiting the particles coalescence.

In-situ TEM experiments have shown that Ag nanoparticles sublimate at temperatures below the Ag melting temperature (about 1000°C), depending on the nanoparticles size, smaller Ag nanoparticles were found to sublimate at lower temperatures[18]. This behavior has been proven to be correlated with the Kelvin equation which was used in combination with kinetic theory by Sambles et al[19] to predict the process kinetics. The main goal of this study is to evaluate the influence of the amorphous carbon layer on Ag mobility; thus, the experiments are conducted in a simple radiation heating holder, which means that the measured temperatures do not correspond to real temperatures; moreover, the heating is not instantaneous. In this

sense, in order to perform more detailed and accurate kinetic measurements more sophisticated heating holders would be required (namely, Aduro heating stage). In addition the evaluation of the beam heating on the particles real temperature would be required. It would be interesting to evaluate the influence of a-C layers on the Ag nanoparticles sublimation temperature, in order to get a better understanding about the sublimation or melting temperatures of silver in ceramic matrixes, specially taking into account the large number of potential applications of Ag nanocomposites to work at temperatures up to 700°C. As reviewed in the State of the Art, the reported works in Ag diffusion at several hundred degrees, do not consider the hypothesis of Ag melting, which cannot be discarded, as shown in the TEM *in-situ* heating experiments presented above.

2.3 TEM cross-sectional analysis

In order to obtain a more detailed view of the coatings cross-sectional morphology and to get a better understanding about the possible Ag diffusion mechanism through a-C coatings, a TEM cross-sectional micrograph of Ag/a-C nanocomposite coating with a thickness of 750 nm is recorded. The coating is deposited in a polymer foil in order to enable its preparation through ultramicrotomy. The TEM micrographs recorded in Jeol 2010F at different magnifications are presented in figures 45 (a) and (b), in bright field mode (BF), whereas figure 45 (c) represents a HRTEM image recorded inside of a column.

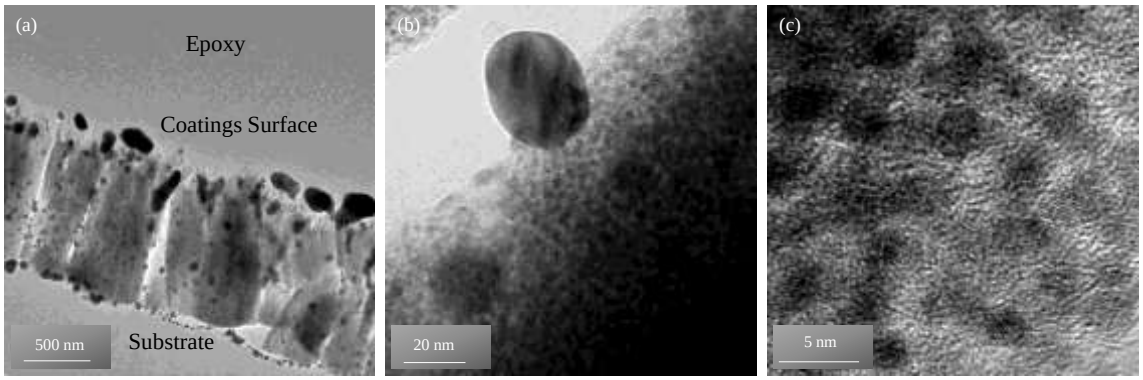

Figure 45 - TEM cross-sectional micrographs of Ag/a-C(750) coating deposited in polymer foil recorded at (a) BF mode representing the entire coatings cross-section, (b) BF mode representing a column boundary and (c) HRTEM mode representing the interior of a column boundary

The TEM cross-sections confirm the morphological features predicted from the previous analysis performed in Chapter IV, namely: (i) the Ag size distribution along the coatings depth and (ii) the columnar growth mode. The observation of the coatings entire cross-section (see figure 45 (a), where the substrate and surface side are identified, as well as the epoxy used in sample preparation) allow to confirm the columnar morphology, with the formation of columns with a width in the order of several hundreds of nanometers. Regarding the Ag distribution along the coatings cross-section, different features can be identified: (i) the surface is composed by big Ag particles with dimensions in the order of hundreds of nanometers, whit a non-spherical shape, (ii) the presence of smaller Ag particles with a spherical shape and size of about 20 nm are detected in the coatings bulk, mainly between the column boundaries, (iii) the Ag particles siting in the coating-substrate interface have higher dimensions in relation to the ones inserted in the bulk, (iv) the presence of smaller clusters with dimensions in order of 2-3 nm, which are found to be located in the a-C columns, being found that their density is much higher in relation to the that of the bigger particles. The coatings morphology suggested by previous analysis was somehow different: formation of small Ag nanocrystals in the coatings bulk (with dimension of 2 to 3 nm) and formation of bigger Ag grains on the surface (with dimensions of 20 nm). It should be pointed out that SEM, TEM and GIXRD analyses in Chapter IV are very consistent in relation to the in depth size distribution of Ag nanoparticles. The difference for the TEM cross-sectional micrographs is that additional trends are shown. These differences may arise from either the type of substrate or the coatings ageing. The main features observed by the different techniques are summarized in Table 11.

The big particle size of Ag nanoparticles observed in the surface of the coated polymeric foil by TEM analysis should be related, as already described before and in agreement with the changes occurring in the C1 sample with time, with a coalescence process induced by the coatings ageing, which in this case leads to the formation of non-spherical particles. The presence of big Ag-NP in the bulk, with sizes of about 20 nm, should be related to the more open columnar morphology associated with the coatings growth onto polymeric substrates.

Table 11 - Ag particle size along coatings depth achieved with different techniques, substrates used and coatings ageing state

Characterization Technique	Thickness (nm)	Substrate	Time after deposition	Surface Size (nm)/Shape	Bulk Size (nm)/Shape
TEM – top-view	40	TEM grid	Few Days	20 + 3	
SEM	250 1000	Si/ SS316L	15 Days	~20 ~20+hundred nm height nanofibers	Not visible
GIXRD	250 and 1000	Si	Few Days	20	3
TEM cross-section	750	Polymer Foil	2 months	Hundred nm (not spherical)	20 nm in column boundaries (spherical) >20 nm 3 nm inside columns (spherical) >20 nm In the coating-substrate interface

The coalescence of Ag particles in free surfaces (which represent the case of column boundaries) has been previously reported, thus being the explanation for the nanoparticles growth between columns also consistent with the formation of aggregates in between the column boundaries, which are clearly visible close to the coatings surface. Regarding the growth of Ag particles at the substrate-coating interface, this might be related to the deposition process. As described in the experimental details, before deposition during the ion etching of the substrates, low powers are applied to both C and Ag targets (1.75 and 0,25 W/cm^2, respectively). Immediately before deposition, the shutter is removed from the front of the targets, being initiated the process of adjusting the powers in each target, decreasing in the case of Ag target (down to 0.09 W/cm^2) and increasing for the C target (up to 7 W/cm^2). Therefore, there is a short time where the numbers of arriving Ag and C atoms to the substrate are much higher and much less,

respectively, in relation to the steady state of the deposition run. Then, there is enough time for Ag adatoms and clusters to diffuse and to coalesce, before they are covered by the C-matrix, giving rise to higher clusters sizes in that zone.

Taking into account the thickness / morphology and the ageing state of the Ag/a-C coating deposited on the polymeric foil, it would be expected that the coatings surface would be already covered with Ag fibers. However, the features observed by TEM and SEM top – view (figure 46) do not reveal the presence of Ag fibers. The TEM cross-sectional micrograph is presented again in order to support the discussion.

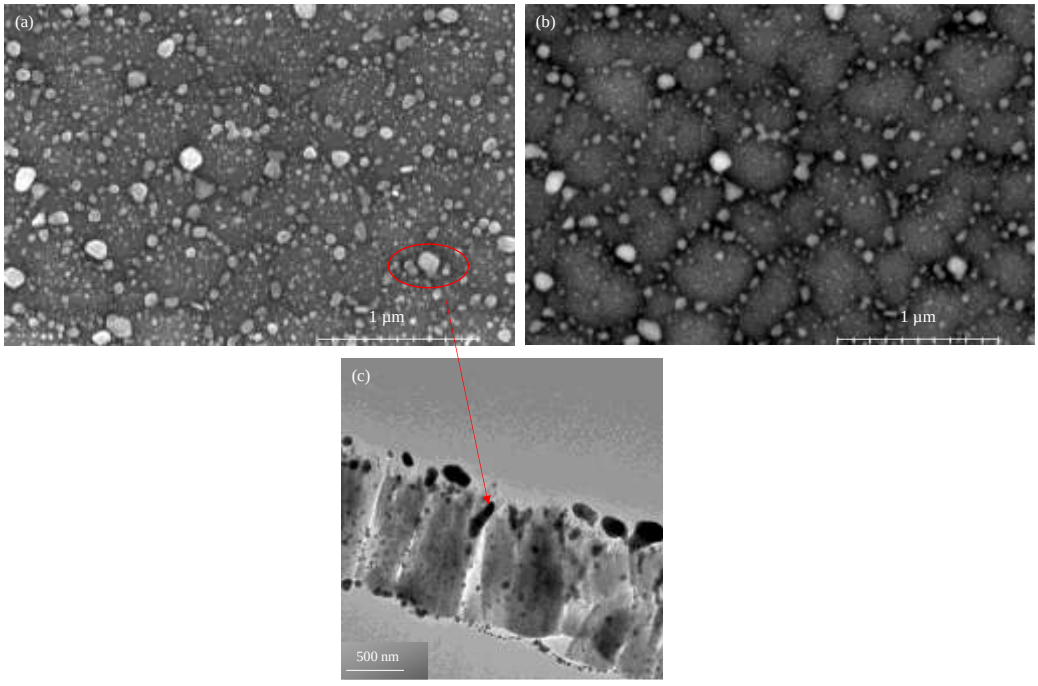

Figure 46 - SEM top-view micrograph of Ag/a-C (750) coating 3 months after deposition

The SEM top-view images allow to observe the presence of a wide Ag size distribution, with the majority of Ag particles located at the top of columns showing dimensions in the order of 10-20 nm. In addition, bigger Ag particles, with non-spherical shape, are observed, mainly located in the column boundaries. The bigger particles show diameters up to 100 nm (marked with a red circle in SEM top-view micrograph), which should correspond to the Ag aggregates observed in the column boundaries in the TEM micrograph (indicated by the red arrow). The shape and morphology of Ag observed in the Ag/a-C (750) deposited in the polymer foil seems quite different from the Ag/a-C (1000)/C4 deposited on SS316L; nevertheless, some conclusions may be drawn:

- Ag grows in between a-C column boundaries forming Ag agglomerates, which final shape and diameter should depend on the size of the voids between the column boundaries,
- The possible reason for the differences found in coated polymer and SS316L samples, should be related with the morphology developed during the coating growth; the latter shows narrower column boundaries, which lead to the formation of fibers with diameters in the order of 10 nm, while in the coated polymer the agglomerates are clearly formed in between column boundaries, showing diameters of about 100 nm, but with a much lower length; in both cases the volume of Ag might not be quite different.

One of the main objectives of this section 2 is to determine the Ag diffusion mechanism through the a-C coating. The possible mechanisms regarding the Ag diffusion pathway are schematically represented in figure 47.

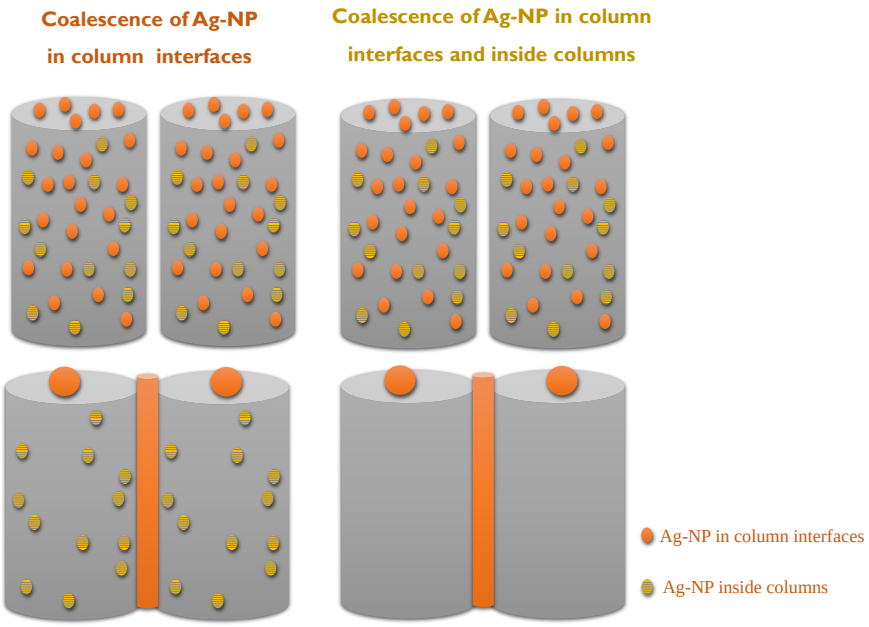

Figure 47 - Models for Ag diffusion through a-C layer and formation of Ag fibers

According to the results of TEM *in-situ* heating experiments, the presence of a compact carbon matrix completely inhibited any Ag particle movement. However, it should be noted that in this experiment bigger Ag nanoparticles were studied and it cannot be unequivocally stated that the a-C matrix of the nanocomposite (figure 45) is

as compact as the a-C layer deposited above the Ag nanoparticles. In fact, the co-deposition of C with Ag can somehow influence the a-C matrix growth. Nevertheless, assuming that the a-C matrix is really compact inside each individual column, it can be predicted that Ag nanoparticles only can move on free surfaces/column interfaces, as: (i) the nanocomposite top-surface in the interface with air and (ii) the column boundaries, which leads us to believe that the model presented in figure 47 right side is more reliable to explain the fibers formation or the Ag agglomeration between the columns boundaries. This model assumes that the Ag-NP embedded in a-C matrix, sitting inside the columns are immobile and thus, do not contribute to the fibers formation. In order to understand if this hypothesis is reliable in terms of mass conservation, a simple model based on a geometrical approach was built. The detailed calculations are provided in the Annex I. The fundamental results obtained in the calculations are summarized in Table 12.

Table 12 - % of Ag particles in column boundaries and fibers length for different column diameter values

	Polymer Foil		**SS316L**	
% of Ag particles in column boundaries	3.37		8.57	
Fiber Ø	85	150	18	24
Fiber heigth	158	51	1709	961

This method allowed to confirm two fundamental aspects: (i) Ag-NP must be present inside the column boundaries due to space restrictions and (ii) in term of mass conservation it is possible to form Ag fibers with a heigth/length in the micrometer range if considering that only the Ag-NP present in column boundaries are mobile and thus able to form nanofibers. It should be noted that by changing the coatings morphology (column boundary diameter and spacing between two adjacent columns) the Ag fibers length is strongly influenced. In fact, in case of polymer and SS316L coated samples the fibers length show extremely different lengths/heights due to the differences in intercolumnar spacing. This calculations allow to understand the formation of long Ag fibers in SS316L coated substrate and the formation of shorter agglomerates in polymer coated sample.

3. Driving force for Ag segregation

3.1 Influence of relative humidity on Ag morphology

C4 nanocomposite coating is deposited onto SS316L substrates. In order to evaluate the effect of humidity in the Ag stability, four different samples are stored in different relative humidity (RH) atmospheres: (i) stored in a glove box containing silica salts (the glove box was closed and, afterwards, the air was removed with a rotary vacuum pump), thus, leading to a RH below 20 %; (ii) stored in atmospheric conditions, RH about 40%, (iii) stored in a glove box with potassium sulphate salts, at a RH of 90% and (iv) immersed in mili-q water, RH of 100%. The coating´s surfaces are analyzed by SEM 10 days after exposure to different humidity conditions and the SEM micrographs are shown in figure 48 (a) to (d) at a magnification of 10 kX and (e) to (h) at magnification of 50 kX.

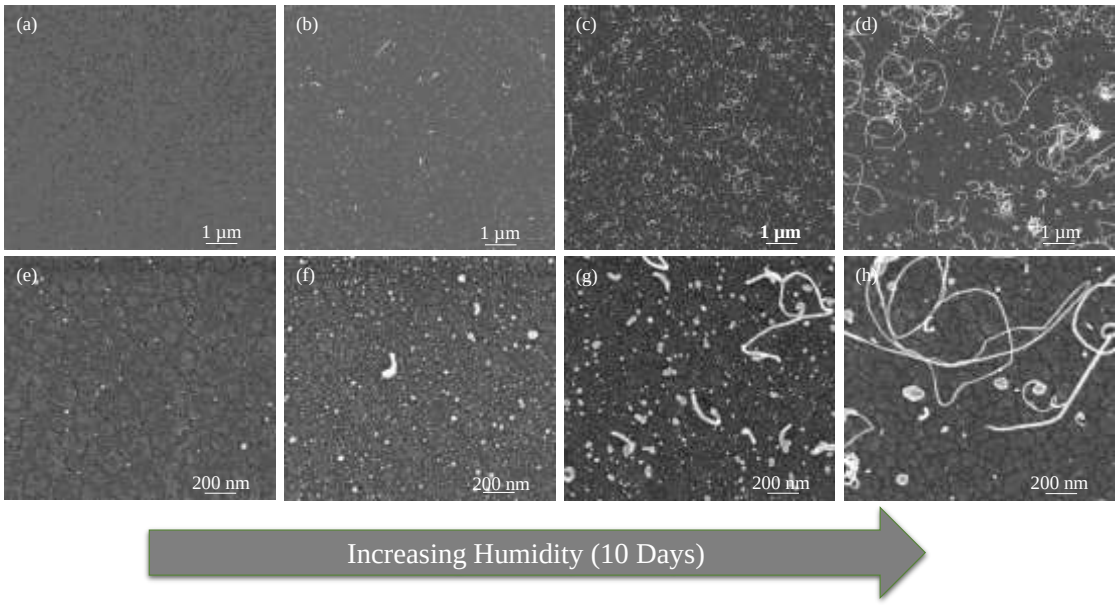

Figure 48 - SEM micrographs of C4 submitted to different relative humidity conditions during 10 days (a),(e) RH below 20%, (b),(f) RH about 40%, (c),(g) RH of 90% and (d),(h) RH of 100%

The SEM micrographs presented in figure 48 clearly demonstrate that the humidity has a strong influence on the agglomeration of surface particles and also on the formation of Ag nanofibers/nanowhiskers. The surface of C4 coating stored at RH = 20% revealed a large amount of small Ag nanoparticles, which size and amount is clearly higher in the coatings stored at RH~40%. Increasing the relative humidity up to 90%,

promotes an increase in the NP/agglomerates size along with the formation of Ag nanowhiskers. The immersed coating does not show evidence of Ag NP, being found that the surface is composed by a small amount of agglomerates and Ag nanowhiskers.

These results clearly show that the presence of humidity is a necessary condition for promoting either the growth of surface Ag particles as well as the formation of Ag fibers. Above, the presence of surface Ag nanoparticles was detected; nevertheless, it remained unclear if these particles were formed during the deposition process or due to surface diffusion of the Ag particles. The results presented in figure 48 clearly show that the Ag particles grow in surface as a consequence of the humidity present in the air. Thus, it would be expectable that during the deposition the size of Ag particles would be about 2 – 3 nm, which is the size of the Ag particles detected in the bulk. The presence of bigger particles in the samples stored at lower relative humidity might be a consequence of some residual humidity and also due to the exposure of the coating to atmospheric conditions during 1 day previously to its storage in vacuum conditions.

3.2 Ag nanowhisker´s chemical composition

So far it seems clear that humidity is a prerequisite for Ag whiskering and growth of surface Ag particles. The formation of metal whiskers has been reported for different metals as discussed in the State of the Art, being the exact mechanism still unclear despite many decades of studies devoted to the understanding of this phenomenon. In the particular case of Ag whiskers, their formation is attributed to the formation of silver sulphides[20,21], which cannot explain the phenomena observed in this work, since the coatings are not exposed to hydrogen sulfide containing atmospheres. Other proposed mechanisms include the relaxation of residual stress[22,23], which cannot explain the differences in the different relative humidity conditions. Other hypothesis is related with the oxidation of Ag or the matrix coating[22,25], which could lead to an increase in the stress state due to the expansion promoted by the formation of oxides. In order to get analyze the possibility of the matrix or Ag oxidation, SEM/EDS analysis is performed in the coating after immersion in mili-q water. The results are presented in figure 49, where the SEM image with the analyzed areas are identified, being the chemical compositions at the site of an Ag nanoparticle and in the matrix depicted in the Table.

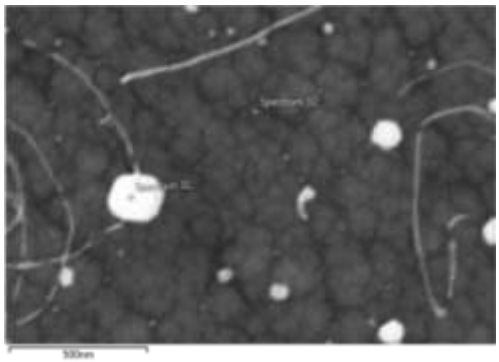

Spectrum	Ag (at.%)	C (at.%)	O (at.%)
Matrix	16	82	2
Ag aggregate	30	65	5

Figure 49 - SEM micrograph of the areas analyzed by EDS and chemical composition of the Ag nanoparticle and the nanocomposite area

The EDS analysis reveals that the amount of oxygen in the Ag nanoparticle (5 at.%) is higher in relation to the matrix nanocomposite coating (2 at.%). The increase in the oxygen content might be associated with the oxidation of Ag nanoparticles; nevertheless, the amount of oxygen is only about 1/6 of the amount of Ag. If Ag oxidation would occur it would be only in the first outside layers of the Ag nanoparticles. EDS analysis usually shows quite poor quantitative analysis and does not allow the analysis of shallow depths. This explains the presence of 65 at.% of C, even in the punctual analysis over the Ag nanoparticle, since the analyzed depth is in the order of 1 μm for the energy used in the analysis (10 keV). Regarding the oxygen content in the matrix coating, it´s content is very low (2 at.%), which is similar to the oxygen content in the as-deposited coatings, thus indicating that the carbon matrix is not being oxidized.

In order to get a better understanding about the possibility of Ag oxidation XPS analysis is carried out in a reference Ag sample, and the samples submitted to the three different humidity levels (20%, 90%,100%). The chemical compositions are depicted in Table 13, while the Ag3d core level and X-ray excited Ag Auger spectra are shown in figure 51 (a) and (b).

The level of oxygen in reference Ag foil is low (below 2 at.%), which may be attributed to the presence of a surface oxide layer, with very low thickness. Regarding the Ag/a-C coatings, they show higher amounts of oxygen in relation to the reference foil, with atomic contents in range of 9 at.% up to 14 at.%, being found that the amount of oxygen slightly increases as the coatings are exposed to higher levels of humidity. The O/Ag atomic ratio ranges between 0.8 to 2.23 in the tested coatings, which is related to the increase in humidity, in case of coatings exposed to RH~20% and 90%, since both

show very similar Ag contents, while in case of immersed coating the increase in O/Ag ratio is mainly due to the decrease in Ag content from about 10% down to 7 at.%.

Table 13 – Chemical composition obtained in XPS analysis

	O (at.%)	Ag (at.%)	C (at.%)	O/Ag
Reference	1.67	98.33	0	0.017
RH~20 %	9.22	11.33	79.45	0.8
RH~90%	11.17	11.97	76.86	0.98
RH~100%	14.73	6.59	78.69	2.23

As previously shown the increase in the humidity level promotes an increase in the Ag trend to grow in the surface and also at 90% and 100% the Ag whiskers start to appear, which according to the previous results found in section 2 are formed due to growth of Ag nanoparticles which segregate to the surface. Thus, it would be expected that the amount of Ag in coatings immersed in mili-q water (RH 100%) would be higher in relation to other samples. Nevertheless, this reduction might be associated with some loss of Ag nanoparticles or Ag ions to the mili-q water.

In order to clarify if Ag nanoparticles form silver oxides, the Ag3d and O1s core level binding energy as well as X-ray excited Ag Auger MNN are analyzed (see figure 50).

Regarding the reference sample, the only visible peak at Ag3d core level is located at 368.4 eV, which is attributed to the presence of metallic silver[26-28]. The O1s spectra suggests the presence of O-Ag bonds located at about 531 eV, nevertheless, the peak intensity is very low, which is related with the very low amount of oxygen present in the sample (below 2 at.%); the low amount of oxygen explains the absence of Ag-O peaks in the Ag3d core level spectra, which should appear at lower binding energies in relation to the Ag-Ag peak (around 357.4 eV)[29,30].

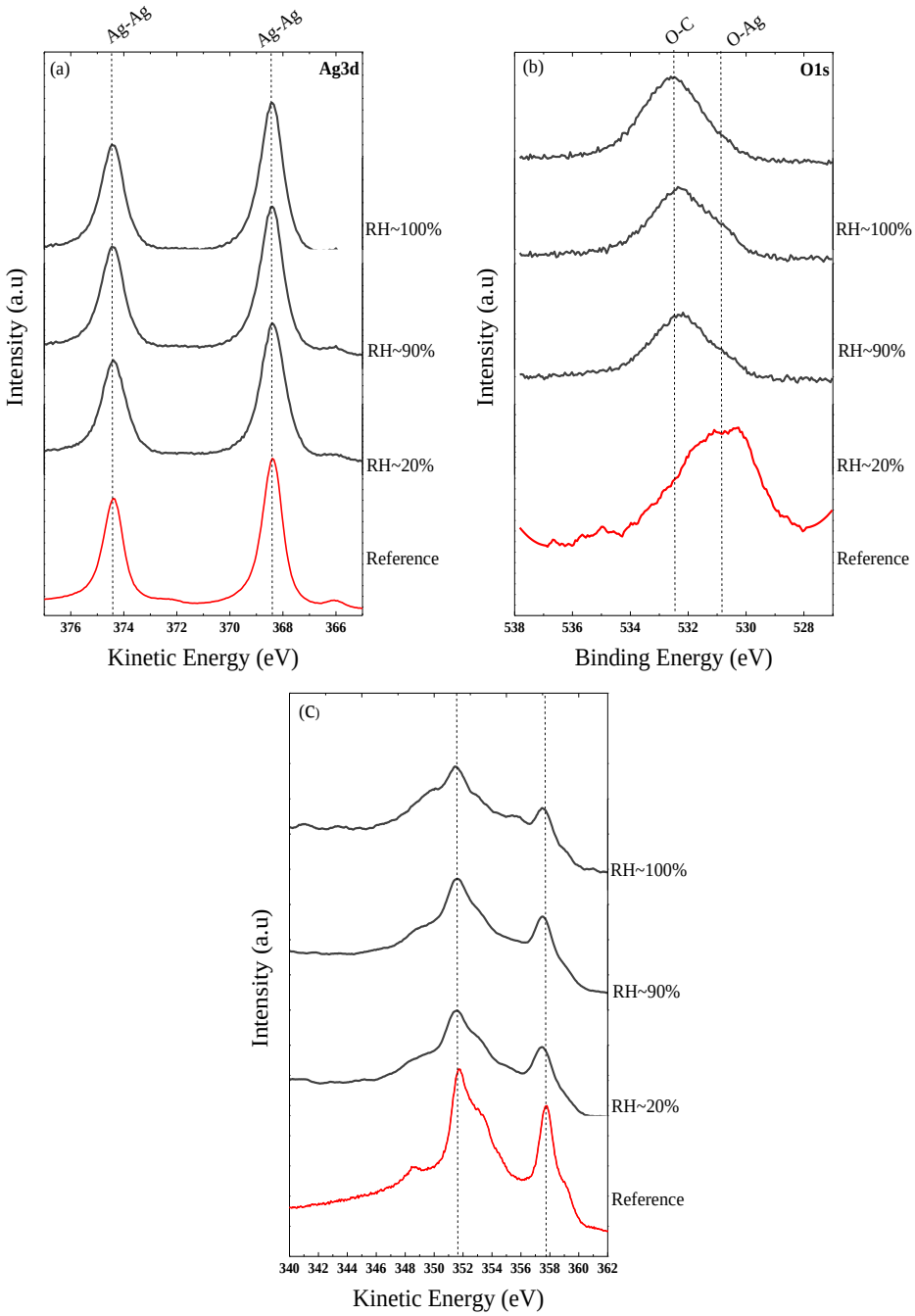

Figure 50 - XPS spectra of (a) Ag3d core-level, (b) O1s core-level and (c) X-ray excited Ag MNN Auger spectra of reference Ag foil and C4 nanocomposites exposed to different humidity levels

The presence of low amounts of oxygen combined with the presence of O-Ag bonds suggest that, possibly, the dangling bonds of Ag surface atoms are bonded with oxygen. The changes in Ag3d core level as well as the presence of O-Ag peaks are very difficult to identify due to either the small changes in the Ag3d peak position (below 1 eV or the presence of surface contaminations, such as O-C bonds and hydroxyl groups located at around 532 eV in O1s spectrum). Therefore, if Ag-O bonds exist in very low

amounts they are easily masked in both Ag3d and O1s peaks. Waterhouse et al[30] found that the metallic Ag peaks are located at a kinetic energy of 358.1 eV in the Auger spectra and the formation of Ag-O bonds leads to a shift down to 357.3 eV. The spectrum in figure 50 (c) shows that for the reference sample the peak is located at around 358 eV, then corresponding to metallic Ag. It is not possible to clearly distinguish any shoulder at the Ag-O position confirming the low or even absence of the oxide bond. Regarding the Ag/a-C coatings, both Ag3d core level and Auger spectra show similar peaks in relation to the reference sample, being also dominated by the metallic Ag-Ag bonds. In relation to the O1s, only one peak is visible, located around 532 eV and attributed to the surface contamination. Although, the presence of O-Ag peaks cannot be discarded, as explained above, even if the bonds are occurring their amount has to be very low, in relation to the Ag-Ag bonds, and of the same level in the metallic Ag foil used as reference.

3.3 Residual stress evaluation in different relative humidity conditions

As above mentioned, soft metal whiskering is generally attributed to stress relaxation, which can be originated from two sources: (i) residual stress generated during the sample preparation and (ii) stresses generated from phase transformations, such as oxidation. In order to clarify if the coatings stress evolve with time in different environments, SS disks of 25 mm are stored in RH~20% and RH~90%, during 20 days and 50 days and the samples curvatures recorded in 2D Profilometer and compared with the uncoated and as-deposited sample, are shown in figure 51.

The results in figure 51 suggest that, after the coatings deposition, the samples curvature becomes more convex, which means that the coating is under compressive residual stress state. The residual stress state is measured in the as-deposited coating, in 3 different samples along two directions by applying the Stoney equation; the measured value was -1.20 ± 0.06 GPa. The profiles shown in figure 51 suggest that no changes occurred along time in any of the coatings submitted to different humidity levels.

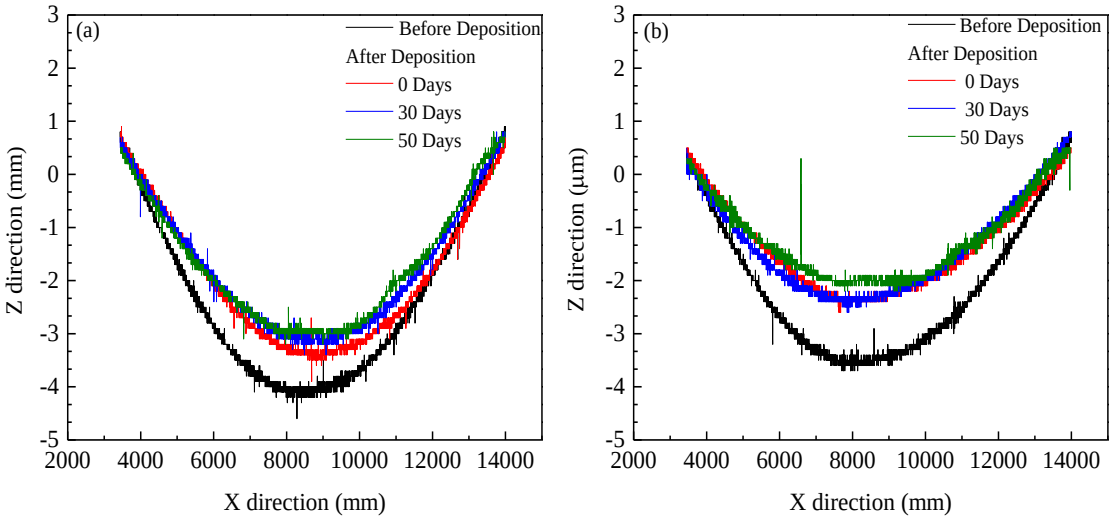

Figure 51 - Changes in the curvature of SS disks coated with C4 with time in different RH conditions (a) 20% and (b) 90%

So far, the XPS and EDS results did not revealed any Ag or carbon matrix oxidation and no significant variations in the stress state were observed for any humidity conditions. Thus, none of the mechanisms proposed for the metal whiskering can be adopted to explain the formation of whiskers in the Ag/a-C coatings. Moreover, even if any of these mechanisms could explain the formation of the Ag nanofibers, it could not explain the growth of Ag nanoparticles in the coatings surface. Therefore, an alternative mechanism undelaying either the growth of Ag nanoparticles at the surface or the formation of whiskers should be considered.

3.4 Mechanism of Ag growth

As reviewed in section 1 of this chapter the agglomeration process can occur through different mechanisms, as shown in Table 10 and figure 34. However, if humidity should be considered a compulsory condition in this process, only two mechanisms could explain the agglomeration of the Ag particles: (i) solid bridges formed due to the precipitation of dissolved particles and (ii) capillary forces. The phenomenon of capillary condensation explains the formation of liquid bridges between particles, even in atmospheric conditions, leading to particles agglomeration. On the other hand, mechanism (i) forming solid bridges, leads to particles coalescence. Therefore, to select the mechanism underlying the Ag particle size growing, it is important to understand if

the particles are agglomerates or if they are formed by single crystals resulting from coalescence. SEM top-view analysis does not allow to determine if the surface particles are agglomerates or coalesced particles; nevertheless, GIXRD method described and applied in Chapter IV, can shed some light on which growth mechanism is taking place: agglomeration or coalescence. The GIXRD diffractograms taken from the samples stored in RH~20% and RH~100% are depicted in figure 52.

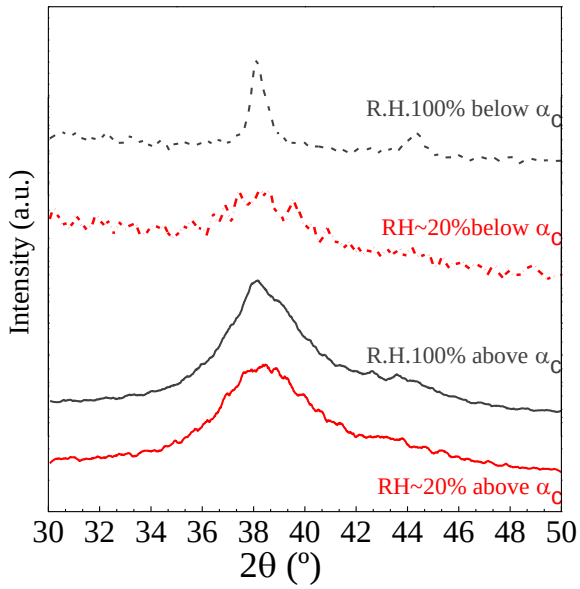

Figure 52 - GIXRD analysis of C4 coating exposed to RH of ~20% and 100%, below and above the carbon critical angle, α_c

Above the carbon critical angle (at 0.7°), both coatings show similar XRD patterns, where the presence of crystalline fcc-Ag phase is detected. The results confirm the presence of the metallic Ag as suggested by XPS analysis even in the coating immersed in mili-q water. Regarding the Ag grain size, the Scherrer method allowed to determine that both coatings are composed of Ag nanoparticles 2-3 nm size. The analysis performed below the carbon critical angle (0.1°) suggested different trends for both coatings: (i) the sample stored at low humidity conditions shows a very broad peak with a low intensity, while (ii) the immersed coating shows a narrower and more intense Ag (111) peak. The grain size of the Ag surface nanoparticles in the coating stored at RH~20% is similar to the grain size found in the bulk of the coatings, while in the other coating the grain size increased up to about 20 nm. In conclusion, the results obtained by GIXRD analysis suggest that the particles grow through a coalescence mechanism

instead of by agglomeration. In this sense, the most likely mechanism for the particles growth should be through a dissolution-precipitation process.

4. Conclusion

The main objective of this chapter is to analyze fundamental aspects of the Ag/a-C nanocomposite coatings stability, namely:

- From which depth the Ag is segregating to the coatings surface?
- How the nanocomposites morphology influences the Ag segregation?
- Is Ag able to move through the a-C matrix?

The Ag stability along time at room temperature and humidity conditions is accessed by SEM analysis and the depth from which Ag is diffusing towards the surface is evaluated by means of GDOES technique. In a first stage, two different Ag/a-C nanocomposite coatings with 20 at.% of Ag are monitored during a period of 6 months: one 250 nm and the other 1000 nm thick. As previously found in Chapter IV, the thinner coatings shows a compact morphology, while the thicker one is columnar. The results suggested that the C4 coating changes gradually with time forming Ag nanofibers/nanowhiskers on the coatings surface. GDOES performed 6 months after deposition indicate the formation of an Ag rich surface layer along with a decrease in the Ag content from 18 at.% down to 14 at.%, across the entire coating thickness. The C1 coating is quite stable with time and the only observed change is the agglomeration of the Ag nanoparticles at the surface. The GDOES analysis of the as-deposited and 6 months aged coatings show similar depth profiles, thus suggesting that no Ag surface segregation is occurring. These results allow to conclude that the presence of a columnar morphology is a required condition for the occurrence of Ag diffusion and the consequent formation of nanowhiskers.

In order to clarify the effect of a compact a-C layer in the Ag mobility a TEM *in-situ* heating experiment is performed in Ag nanoparticles deposited by PGC and covered with a very compact a-C layer, to be compared with free Ag clusters, already reported in literature. The presence of the compact amorphous carbon layer completely avoided

the particles sintering, inversely to what was reported in the literature for free Ag nanoparticle's.

A comparison between Ag/a-C coatings deposited onto different substrates - SS316L and polymer foil- showed the occurrence of different morphologies, with separation between columns of about 10-20 nm and 100 nm, respectively. Consequently, the shape and diameter of Ag features in the surface was different: in the first case Ag nanowhiskers with a diameter of about 10-20 nm and length of several hundreds of nanometers were formed, while in the coated polymer foil Ag agglomerates / coalesces with dimensions that can be bigger than 100 nm and heights of tens of nanometers. Simple calculations based on a geometrical approach and on the Ag content and Ag particle diameter allow to show that the amount of Ag in the free spaces at the column boundaries is enough to provide the formation of Ag nanoswhiskers with the above pointed dimensions.

Nanoparticles agglomeration or coalescence are very likely to occur due to the high energy of a small particle with high % of dangling bonds. Humidity can enhance this process, and its influence on the stability of the C4 nanocomposite. After the deposition process this coating is stored in four different atmospheres with relative humidity's of: (i) 20%, (ii) 40%, 8iii) 90% and (iv) 100% - immersed in mili-q water. The SEM top-view micrographs recorded 10 days after exposure confirmed that the humidity plays the major role in the Ag stability. The sample stored at 20% of RH shows a small number of Ag nanoparticles, at least in the resolution limit of SEM analysis. Conversely, the coating stored at 40% RH shows a large number of Ag nanoparticles and agglomerates, while the coatings stored at higher RH are covered with Ag nanowhiskers and agglomerates. EDS analysis shows a slightly higher level of oxygen in the Ag agglomerates in relation to the matrix coating; nevertheless, no signs of Ag-O bonds are found by XPS analysis, which only reveals the presence of metallic Ag-Ag bonds. Thus, the Ag whiskering promoted by soft metal oxidation is not likely to occur in this case, as reported in the literature for other systems. The substrate curvature profiles, for evaluating the coatings residual stress, prove that no changes occurred with time in any of the samples exposed to different levels of humidity. In this sense, the hypothesis of stress relaxation to explain the nanowhiskering phenomena found in Ag/a-C nanocomposite coatings is not viable. The interpretation for the Ag whiskering was achieved by GIXRD analysis performed in the Ag/a-C nanocomposites stored at RH of 20% and 100%. The presence of a narrow

diffraction peak (related with an Ag crystalline phase) for angles of incidence below the carbon critical angle in the coating stored in mili-q water, while a broader peak occurs for the coating stored in low humidity atmosphere, allowed to confirm that the Ag particles grow in surface through a coalescence process and not through agglomeration. Therefore, considering the mechanisms proposed by Rumpf and co-workers for agglomeration and coalescence processes, it could be concluded that the Ag nanoparticles growth is mediated by a dissolution- precipitation (Oswald ripening) process.

References

[1] Cao G. in *Nanostructures and Nanomaterials, Synthesis, Properties and Applications*, Imperial College Press, U.S.A., 2004.

[2] Butt H.J., Kappl M. in *Surface and Interfacial Forces*, Wiley-VCH, Germany, 2010.

[3] Pietsch W. in *Agglomeration Processes – Phenomena, Technologies, Equipment*, Wiley-VCH, Germany, 2020.

[4] Sigmund W., El-Shall M., Shah D.O.,Moudgil B.M. in *Particulate systems in nano and biotechnologies*, CRC Press, 2009.

[5] J. Jiang, G. Oberdrster, P. Biswas, *Characterization of size, surface charge, and agglomeration state of nanoparticle dispersions for toxicological studies*, Journal of Nanoparticle Research, 11 (2009) 77–89.

[6] Mehrer H, in *Diffusion in Solids Fundamentals, Methods, Materials, Diffusion-Controlled Processes*, Springer, U.S.A., 2007.

[7] Asoro M., *Coalescence and Sintering in Metallic Nanoparticles: In-situ Transmission Electron Microscopy (TEM) Study*, PhD thesis, s.l. University of Texas, 2012.

[8] P. Jensen, A. Clement, L. J. Lewis, *Diffusion of nanoclusters*, Computational Materials Science, 30 (2004) 137–142.

[9] M. A. Asoro, D. Kovar, P. J. Ferreira, *Effect of surface carbon coating on sintering of silver nanoparticles: in situ TEM observations*, The Royal Society of Chemistry DOI: 10.1039/c4cc01547.

[10] N.I. Papanicolaou, G.A. Evangelakis, G.C. Kallinteris, *Molecular dynamics description of silver adatom diffusion on Ag(100) and Ag(111) surfaces*, Computational Materials Science, 10 (1998) 105-110.

[11] G. Antczak, G. Ehrlich, *Surface diffusion: metals, metal atoms and clusters*, Cambridge University Press, 2010.

[12] W. W. Pai, A. K. Swan, Z. Zhang, J. F. Wendelken, *Island Diffusion and Coarsening on Metal (100) Surfaces*, Physical Review Letters, 79(13) (1997) 3210.

[13] J.-M. Wen, James W. Evans, M. C. Bartelt, Joseph W. Burnett, Patricia A. Thiel, *Coarsening Mechanisms in a Metal Film: From Cluster Diffusion to Vacancy Ripening*, Physical Review Letters, 76(4) (1996) 652.

[14] R. Escobar Galindo, N. K. Manninen, C. Palacio, S. Carvalho, *Advanced surface characterization of silver nanocluster segregation in Ag – TiCN bioactive coatings by RBS, GDOES, and ARXPS*, Analytical and Bioanalitycal Chemistry, (2013) 405:6259 – 6269.

[15] Nelis T., Payling R. in *Glow discharge optical emission spectroscopy: A practical guide*, The Royal Society of Chemistry, UK, 2003.

[16] J. Robertson, *Diamond-like amorphous carbo*n, Materials Science and Engineering R, 37 (2002) 129-281.

[17] Y.T. Pei, D. Galvan, J.Th.M. De Hosson, *Nanostructure and properties of TiC/a-C:H composite coatings*, Acta Materialia, 53 (2005) 4505–4521.

[18] M. A. Asoro; J. Damiano ; P. J. Ferreira, *Size effects on the melting temperature of silver nanoparticles: In-situ TEM observations*, Microscopy and Microanalysis, 15 (2009) 706-707.

[19] J. R. Sambles, L. M. Skinner and N. D. Lisgarten, *An electron microscope study of evaporating small particles: the Kelvin equation for liquid lead and the mean surface energy of solid silver*, Proceedings of the Royal Society, 318 (1970) 507-512.

[20] B.H. Chudnovsky, *Degradation of power contacts in industrial atmosphere: silver corrosion and whiskers*, Proceedings of the 48th IEEE Holm Conference on Electrical Contacts, 2002.

[21] M.A. Rivera, *Design considerations for reliable electrical, control and instrumentation systems in geothermal power plants with emphasis on hydrogen sulphide related problems*, Geothermal Training Programme, 20 (2007).

[22] Crandall E. *Factor governing tin whisker growth – Springer Theses*, PhD thesis, s.l. Auburn University, 2013.

[23] E. Chason, N. Jadhav, F. Pei, E. Buchovecky, A. *Bower, Growth of whiskers from Sn surfaces: Driving forces and growth mechanisms*, Progress in Surface Science, 88 (2013) 103-131.

[24] Metal Whiskers, NASA Tin Whisker (and Other Metal Whisker) Homepage, Accessed in July 2015. Available online: http://nepp.nasa.gov/whisker/

[25] T. Takahashi, A. Abdulkadhim, D. Music, J. M. Schneider, *Spontaneous Formation of In-Whiskers on YIn3 Thin Films Deposited by Combinatorial Magnetron Sputtering*, IEEE Transactions on Nanotechnology, 10(5) (2011) 1202-1208.

[26] N. K. Manninen, R. Escobar Galindo, N. Benito, N N.M. Figueiredo, A. Cavaleiro, C. Palacio, S. Carvalho, *Ag–Ti(C, N)-based coatings for biomedical applications: influence of silver content on the structural properties*, Journal of Physics D: Applied Physics, 44 (2011) 375501 (8pp).

[27] S. Calderon V, R. Escobar Galindo, N. Benito, C. Palacio, A. Cavaleiro, S. Carvalho, *Ag^+ release inhibition from ZrCN–Ag coatings by surface agglomeration mechanism: structural characterization*, . Journal of Physics D: Applied Physics, 46 (2013) 325303 (10pp).

[28] Wagner C.D. in *Handbook of X-Ray Photoelectron Spectroscopy*, Perkin Elmer Corporation, U.S.A., 1979.

[29] Y. Abe, T. Hasegawa, M. Kawamura, K. Sasaki, *Characterization of Ag oxide thin films prepared by reactive RF sputtering*, Vacuum, 76 (2004) 1–6.

[30] G.I.N. Waterhouse, G.A. Bowmaker, J.B. Metson, *Oxidation of polycrystalline silver foil by reaction with ozone*, Applied Surface Science, 183 (2001) 191-20

Chapter VI

Functional Properties

The main goal of this thesis is the development of Ag/a-C nanocomposite coatings with potential application as antibacterial surfaces. Over the past years the surface modification of materials with Ag nanoparticles for different applications, such as food packages (which are already available in the market), medical devices including surgical instruments or indwelling devices, has been intensively studied by many companies and research groups. The aim of this Chapter is to evaluate the functional properties of the developed nanocomposite coatings, namely, the antibacterial activity and the tribological behavior in biological fluids. For this propose, three types of coatings were studied: an a-C layer (C5), as a reference sample, and two C4 coatings either in the as-deposited state or after ageing. The selection of the C4 coating, despite of its non-stable behavior, is based on its columnar morphology which allows either a higher contact area with the biological medium, condition necessary for achieving antibacterial activity, or a continuous Ag surface segregation which can keep this activity along the time. Since the antibacterial tests need to be performed simultaneously in all samples, an ageing treatment (at a pressure of 3 bar and temperature of 130°C) was performed in an autoclave allowing the comparison of the C4 coating in the as-deposited state and after ageing.

The tribological tests are performed in dry-sliding conditions, in Hank´s Balanced Salt Solution (HBSS) and HBSS containing bovine serum albumin (BSA), which are the commonly studied media for the evaluation of the biotribological properties of materials used in joint prostheses. As discussed in Chapter III, the presence of Ag and, particularly, its accumulation in the coatings surface degrade the tribological properties of the a-C/Ag coatings in dry sliding conditions. Nevertheless, the presence of lubricants can change

the nature of the tribological pairs in contact, i.e. it can prevent the contact between Ag-Ag, which would avoid the degradation of the tribological properties. As one of the potential applications of the coatings is for joint prosthesis, the evaluation of the biotribological properties is, thus, mandatory.

1. Ag antibacterial activity and ionization

The spread of nanosilver based products in the market made that Ag nanoparticles are, presently, the most commercialized in the World. According to the Project in Emerging Technologies inventory on nanotechnology based products the number of nano-Ag products is presently around 383, being most of their applications related with health and fitness products as well as food and beverage[1]. Despite some controversial issues related with the toxicity of these metal nanoparticles, the only reported side effect caused by the consumption of dietary supplements containing silver (mainly based on Ag colloidal suspensions) is argyria, a permanent discoloration of the skin, nails and gums. In fact, Food and Drug Administration (FDA) has reported a consumer advice related with the consumption of these products where the chronic oral reference dose (RfD) of 5 micrograms of silver per kilogram of body weight per day is pointed to cause argyria, according to the tests performed by the Environmental Protection Agency (EPA)[2,3]. Thus, taking into account this reference value, the limit of toxicity is quite high, but still, needs to be taken into account in the development of devices to be placed within the human body. Over the past years many research works have focused on the implementation of Ag nanoparticles in indwelling devices as a strategy to combat the biofilm formation, which results in surgical implant infections, pointed as the main cause of failure of different biomedical devices[4,5]. Nevertheless, in the Project in Emerging Technologies inventory no indwelling devices containing Ag nanoparticles are referred[1]. The acceptance of Ag nanoparticles and nanoparticles in general is presently a very controversial issue due to the possible toxic or side effects caused by the nanoparticles either when placed within the human body, or in their release to the environment with possible side effects which are still not very well understood[6,7].

Despite the large number of commercially available consumer products and the huge number of research studies in Ag nanoparticles, their mechanism of actuation against bacteria, as well as their behavior in different biological medium, are still under intensive study. Several mechanisms have been pointed to explain the antimicrobial activity of Ag nanoparticles, in particular: (i) release of Ag^+, (ii) generation of free radicals and (iii) direct physical contact between the nanoparticles and the bacterial cells which causes structural damage to their wall[1,8,9,10]. Among the different proposed mechanisms

the Ag ions are pointed to be the most effective route for the bacteria destruction[8,9]. Thus, in order to achieve the desired bactericidal effect it is necessary to guarantee that the Ag based products are somehow transformed into Ag^+. Then, as Ag is in the metallic state, electrochemical reactions able to promote silver oxidation are required to promote silver ionization.

The basic electrochemical processes are generally represented by a simple wet corrosion cell which contains four fundamental elements:

i. Anode – works as the electron producing electrode. The simplified half reaction that occurs in the anode is represented by the equation 6.1

$$Me(s) \rightarrow Me^{x+}(aq) + \text{è} \tag{6.1}$$

ii. Cathode - works as the electron acceptor electrode. The simplified half reaction occurring in the cathode is represented by the equation 6.2:

$$Me^{x+}(aq) + \text{è} \rightarrow Me(s) \tag{6.2}$$

iii. Electrolyte – electrical conducting solution

iv. Electrical connection – physical contact between the anode and the cathode able to allow the electrons flow.

It should be pointed out that the half reactions represented by equation 6.1. and 6.2 are over simplified, in fact, the metals oxidation is not a one step process, conversely it evolves numerous steps with formation of intermediate components (namely adsorbed $Me(H_2O)$, $MeOH^-$,$MeOH^+$), which strongly depend on the elements/ions present in the electrolyte[11]. In silver case, the release of Ag ions in simple solutions containing no other oxidants or reductants, besides oxygen and hydrogen, is described by the global reaction:

$$2Ag(s) + \frac{1}{2}O_2(aq) + 2H^+(aq) \longleftrightarrow 2Ag^+(aq) + H_2O(l) \tag{6.3}$$

Where $\Delta G°$ value is -91.3kJ/mol at 298 K[12].

Liu et al.[13] have evaluated the effect of oxygen and pH on the silver ion release from 1.9 nm sized Ag nanoparticles in different aqueous medium: (i) air saturated water, (ii) deoxygenated water and (iii) both solutions (i) and (ii) at different pH values ranging from 4 to 9. The authors found that removing the dissolved oxygen completely, the silver release was inhibited (indicating the essential role of Ag surface oxidation initiated by O_2) and, also, that the Ag^+ release is strongly dependent of the pH (H^+ concentration), being the higher ionization rates achieved with lower pH values. Thus, the Ag^+ release was found to be a cooperative oxidation process requiring both protons and dissolved O_2. Moreover, the addition of Ag nanoparticles to the solution promoted a decrease in the free [Ag^+], which was attributed to the adsorption of Ag ions in nanoparticles surface or reduction of Ag^+. Therefore, the authors suggested that the colloid solution contains three forms of silver: Ag, Ag^+ and adsorbed Ag^+. An ion release mechanism in water was, then, proposed, where the formation of intermediate peroxides could occur. The oxidation of nano Ag to Ag^+ is not likely to take place through a four-electron transfer process that reduces O_2 directly to water but, rather, through simpler redox reactions that produce peroxide intermediates, which were detected in the nano Ag containing solutions. In this process, H_2O_2 is a more powerful oxidant than O_2. The complete electrochemical process was not described, although the essential pathway could be described by the equation 6.4:

$$O_2 + H^+ \xrightarrow[AgO]{} Ag^+ + H_2O_2 intermediates \xrightarrow[AgO]{} Ag^+ + H_2O \quad (6.4)$$

where the first reaction occurs slowly, while the second one is fast due to the higher oxidative power of H_2O_2.

As previously mentioned, the Ag oxidation mechanism is strongly dependent on the electrolyte properties such as the pH value and the chemical composition. Recently, a few reports have presented the silver nanoparticles ionization rate in different electrolytes[14,15]. Loza et al[14] evaluated the nano Ag dissolution in different solutions: (i) water containing 10 Mm H_2O_2; (ii) argon saturated water, (iii) 0.9% NaCl and (iv) phosphate buffered saline solution (PBS), (v) 1g/L glucose and (vi) cysteine as a model for sulphur containing proteins. The presence of oxygen is fundamental since the dissolved oxygen is responsible for the metallic silver dissolution, being the Ag^+ ionization increased with the addition of H_2O_2, known as a fast oxidant. Moreover, the

dissolved NaCl and PBS solutions showed a lower ionization rate (4 wt.% and 2 wt.%, respectively) in relation to the pure water, where 50 wt.% of Ag was ionized. Cysteine inhibits the Ag dissolution, while glucose showed a decelerating effect, still showing a similar final dissolved fraction. Similar studies have been performed by other authors and the main conclusion is that the presence of different elements and chemical compounds in the biological fluids tends to reduce the Ag ionization rate, through different mechanisms, which are summarized in figure 53.

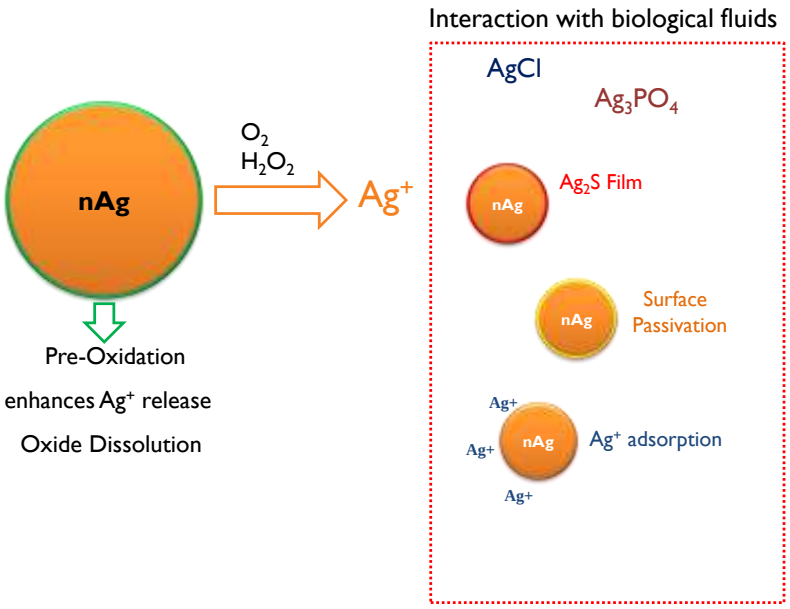

Figure 53 - Possible interactions between Ag ions and compounds present in biological media

The presence of chloride (Cl^-) or phosphate is responsible for the precipitation of AgCl or Ag_3PO_4, being the lately formed only if no chlorides are present. Other observed trend in every paper related with the evaluation of Ag ionization with time in different liquids is related with the stabilization of the Ag ionization after a certain period of time, being the time dependent either on the biological medium or on the stabilizers used in the Ag nanoparticles surface or matrix coating where they are incorporated. In fact, from an application point of view this can somehow constrain the Ag applicability since the Ag stabilization will result in the loss of the antibacterial activity along the time. The exact mechanism underlying this stabilization is still not understood and some of the possible explanations include the silver nanoparticles agglomeration or the surface passivation during immersion[14-18].

2. Coatings antibacterial activity

2.1 Electrochemical behavior of Ag and a-C

As previously mentioned, the antibacterial activity of silver- based nanocomposite coatings is dependent on the Ag ionization, which is determined by the nanoparticles size[19-21] and the electrolyte[14,15]. Another important factor for Ag ions release is the electrochemical interaction between the matrix and the Ag nanoparticles. Therefore, since the antibacterial activity is determined by electrochemical processes, the coating matrix should be carefully selected. Once the coating matrix and the Ag nanoparticles are physically connected, it is necessary to ensure that the matrix will not eradicate the Ag oxidation. Any physical contact between two distinct materials results in galvanic corrosion, where the most active metal acts as anode and the least active as cathode This process tends to accelerate the corrosion rate of the most active element. Thus, when choosing a coating matrix the standard galvanic series should be analyzed in order to ensure that the coating matrix is more noble than Ag. The galvanic series in sea water indicate that graphite is the most noble element, with a free corrosion potential vs SCE between 0.3 and 0.2, while Ag shows values between 0 and -0.5. This is in accordance with what has been historically known that the graphite grease deposited in aircraft fuel pipe couplings promote a severe corrosion of the alloys used in these components. Moreover, carbon in the amorphous form is also likely to cause galvanic corrosion. Obviously, the values above presented are just an indication of the electrochemical behavior of Ag/a-C coatings, since a-C is not pure graphite as discussed in the State of the Art; moreover, the electrochemical behavior is dependent on the electrolyte[11].

Thus, in order to understand if a-C matrix was a reliable choice for this study, the open circuit potential of a-C(C5), Ag thin film and bulk Ag is determined and compared with the OCP value of the Ag/a-C(C4) nanocomposite coating in 0.9% NaCl electrolyte. The coatings are deposited onto SS316L substrate for the study of the functional properties. The electrolyte is not the one used in antibacterial tests, which would be the ideal approach; nevertheless, since the ICP analyses are performed in physiological solution, the OCP analyses were also performed in this electrolyte to allow a direct comparison of the results. The OCP results are depicted in figure 54.

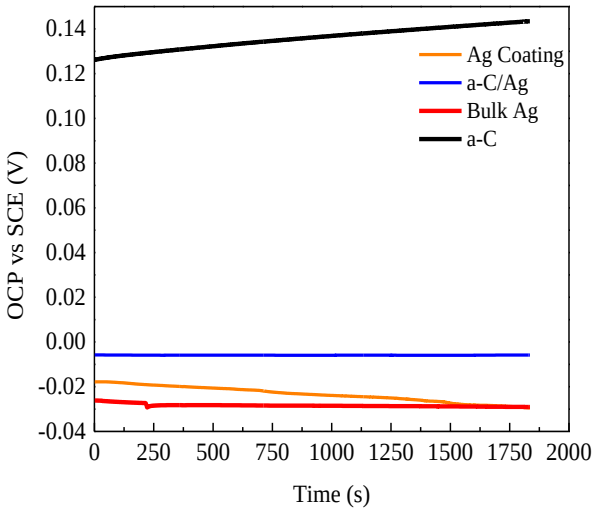

Figure 54 - OCP of a-C, Ag/a-C and Ag (bulk and coating) in 0.9 % NaCl

The a-C coating shows an open circuit potential of about 0.14 V, while both Ag coating and bulk Ag show very similar OCP values around -0.03 V. The positive OCP value of a-C coatings suggests that it should be spontaneously reduced. Ag is a noble metal with a positive standard reduction potential value, thus meaning that it does not tend to be oxidized. However, in 0.9%NaCl solution the OCP is negative which means that it tends to be oxidized. The Ag/a-C nanocomposite coating shows an intermediate behavior between Ag and a-C, with an OCP value around -0.006 V, which is somehow predictable taking into account the mixed potential theory which states that for two conductive phases in electrical contact the resulting OCP is located between the OCP values of both phases. Taking into account the OCP results it can be predicted that a-C matrix is suitable for this application since it shows a higher reduction potential in relation to Ag. Moreover, the Ag is oxidized in 0.9% NaCl which means that the combination of both phases should lead to an enhanced Ag oxidation, which in fact is the envisaged effect.

It should be mentioned that the OCP value is determined for Ag thin film and bulk Ag, which should be different from the OCP value of Ag nanoparticles. Nevertheless, the measurement of electrical parameters (in this case voltage) in nanoparticles is quite difficult to achieve in experimental conditions since if they lay on an inert glass substrate, no current flow occurs between the tested nanoparticles and the electrode used for the voltage determination. On the other hand, if the nanoparticles are deposited over a SS316L surface the analysis would be influenced by the substrate

itself. Thus, Ag thin films and bulk Ag were used in order to get some insight about its electrochemical behavior in 0.9% NaCl.

2.2 Coatings morphology

The coating studied in this Chapter is the C4 in the as-deposited state and after has been thermal annealed in an autoclave at a pressure of 3 bar and a temperature of 130°C, during a period of 5 minutes. The main objective is to evaluate the influence of coatings ageing on the Ag ionization rate and the antibacterial activity. These nanocomposite coatings are compared with a pure a-C layer (coating C5). The SEM top-view micrographs are depicted in figure 55 in SE mode ((a) to (c)) and BSE mode ((d) to (f)).

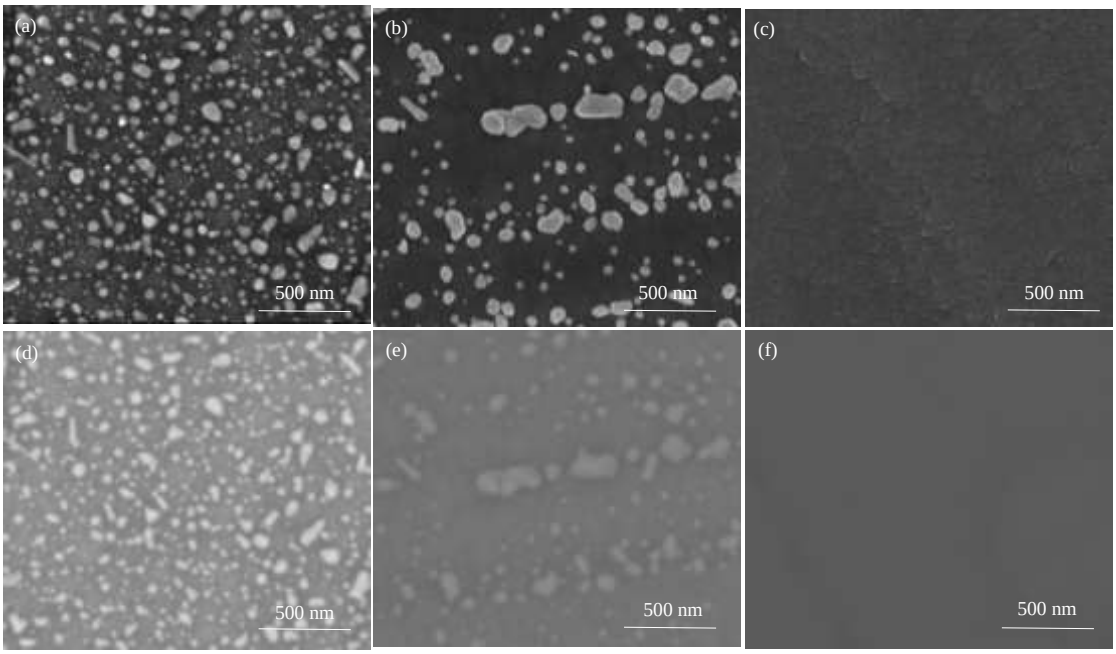

Figure 55 - (a,d) C4 as-deposited; (b,e) C4 autoclave and (c,f) C5

SEM shows that both a-C/Ag nanocomposite coating´s surfaces are covered with Ag nanoparticles, which size is clearly higher for the thermal treated sample. The Ag particle size distribution was analyzed in the SEM micrographs with *ImageJ* software and the histograms are shown in figure 56.

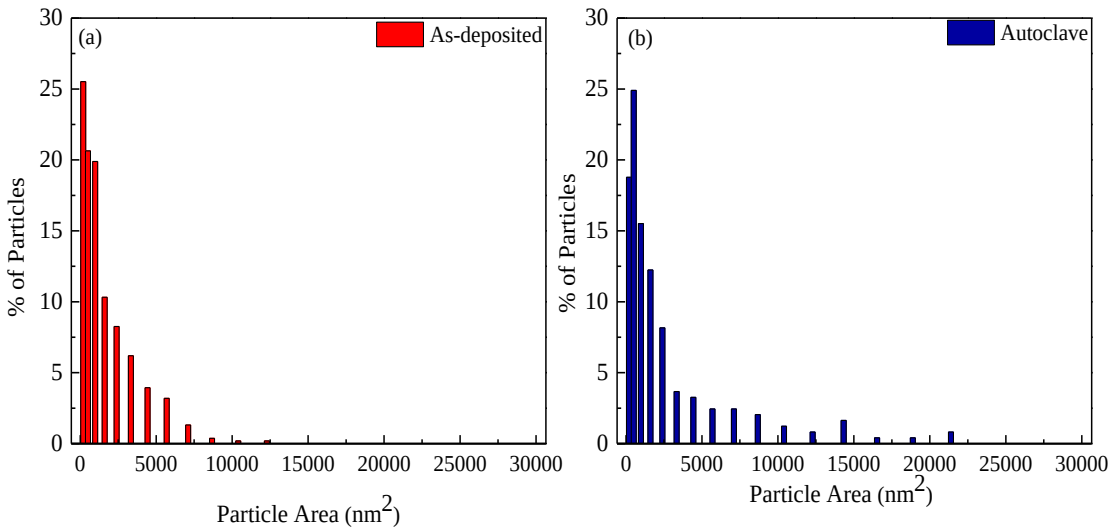

Figure 56 - Histograms of Ag particle area of C4 (a) as-deposited and (b) heat- treated in autoclave

In the as-deposited state most of Ag nanoparticles (25%) show an area of 196 nm^2 and the maximum value is close to 12000 nm^2. The sample thermal treated in the autoclave showed a shift of the mean value to 510 nm^2 and the maximum particle size increased up to 22000 nm^2. These results clearly indicated that the autoclave treatment promoted the agglomeration of the surface Ag nanoparticles; nevertheless, no Ag whiskering is detected, which means that the ageing is still in its very initial state.

The direct comparison between SE and BSE micrographs allows to conclude that all the big particles are sitting in the coatings surface. In fact, in SEM the depth of analysis is higher in BSE than in SE and, then, since no additional big particles are observed in the BSE image, all of them viewed in SE should be sitting at the coatings surface and those inserted in the bulk should be very small (~ 3 nm, undetectable by SEM) as suggested in previous chapters).

2.3 Ag ionization

The Ag ionization rate was determined by ICP analysis along a period of 30 days of immersion and the results are shown in figure 57.

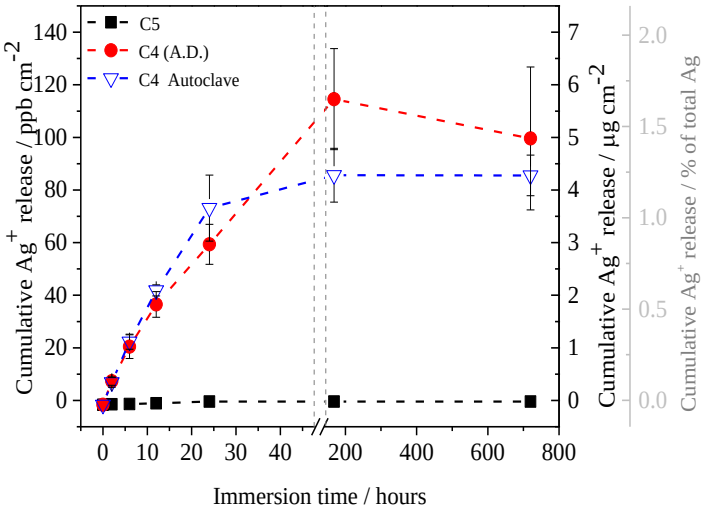

Figure 57 - ICP analysis of Ag ionization rate over a period of 30 days

As expected, no Ag ions are released in a-C coating, while both as deposited and autoclave treated samples show similar Ag ionization trends, which suggests that the variations in the surface Ag particle size does not influence the Ag ionization rate. The amount of Ag ions in physiological solution increases linearly in the first 24 hours up to about 60 to 70 ppb.cm^{-2}; afterwards, the amount of Ag ions increases slower up to about 80 to 110 ppb.cm^{-2} after an immersion period of 168 hours (7 days), remaining constant thereafter up to 720 hours (1 month). The mass % of Ag released is calculated and compared to the total Ag mass in Ag/a-C nanocomposite coatings, being the value depicted in the y axis (right side). The Ag ionization stabilized when 1.0% to 1.5% of the total Ag mass is released. The percentage of Ag particles sitting in the interface with air (column boundaries and coating surface) has been determined to be around 9%, according to the calculations provided in the annex and discussed in Chapter V. In fact, the interaction between the Ag nanoparticles and the liquid medium is required in order to achieve the Ag ionization and it can be somehow predicted that the Ag nanoparticles embedded in the compact a-C layer, within the columns, are much more difficult to ionize. The stabilization in Ag ionization should not be attributed to the lack of Ag in interfaces with liquid medium. Other studies with Ag nanoparticles immersed in different

liquid medium also show a stabilization in the Ag ionization occurring before the consumption of the total amount of Ag present in the liquid. In fact the % of ionized Ag in different liquids is always below 100% being strongly dependent on the tested liquid media[14,15]. Finally, the presence of negatively charged ions such as Cl^- which tend to bind to Ag^+ ions, forming AgCl crystals, might be one more reason for Ag ionization stabilization. In order to get a better insight about the possibility of Ag agglomeration or AgCl formation, SEM/EDS analysis is performed in coatings immersed in 0.9% NaCl, during 2 h, 24h and 30 days after immersion, being the results shown in figure 58.

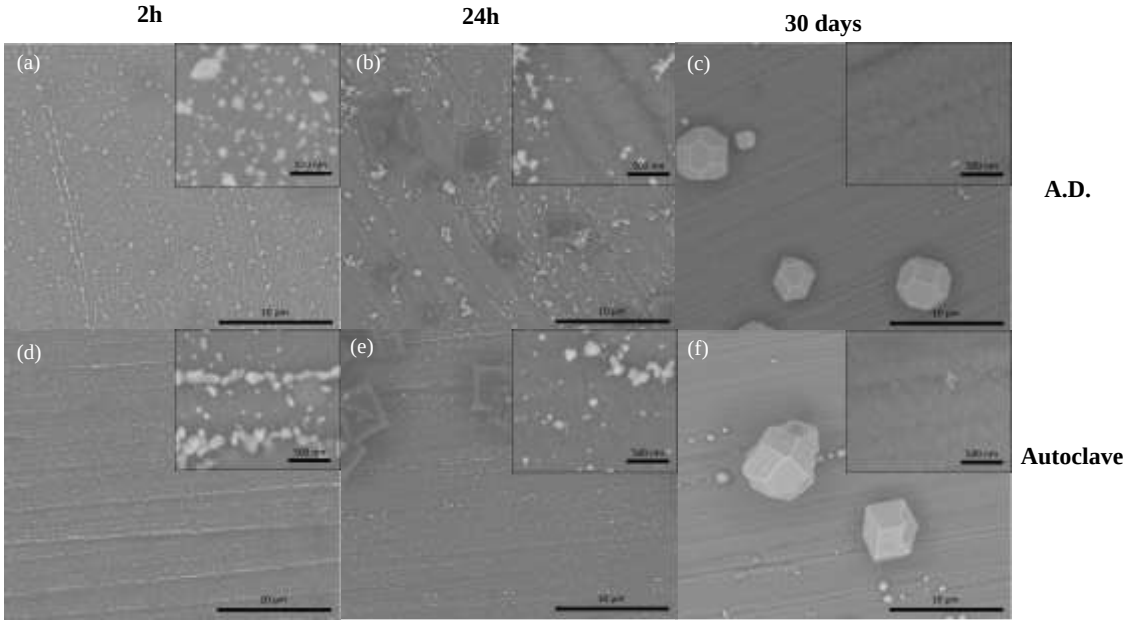

Figure 58 - SEM top-view micrographs after immersion in 0.9%NaCl during 2 hours (a) C4 (A.D.), (d) C4 autoclaved, 24 hours (b) C4 (A.D.), (e) C4 (autoclaved) and 168 hours (c) C4 (A.D.), (f) C4 autoclaved

After 2 hours of immersion, the surface of both, as-deposited and heat treated, coatings is covered with Ag agglomerates, with irregular and non-spherical shape, combined with small spherical Ag particles. Ag particles agglomeration increases with time (from 2 to 24 hours). The Ag nanoparticles agglomeration should be promoted by a dissolution-precipitation process, which has already been reported by Li et al.[22] The Ag agglomeration results in the development of similar morphologies in both coatings even after very short immersion times, which might explain the similar ionization rates in both coatings. Other interesting feature is the accumulation of Ag agglomerates in the scratched regions, which arise during the substrate polishing. At these sites, the formation of column boundaries is more likely to occur, due to shadowing effects, being

the Ag diffusion pathways located in these regions; thus, a higher density of agglomerates are observed in these areas.

The SEM images recorded 30 days after immersion, reveal the formation of crystals with sizes of a few micrometers and almost no additional Ag nanoparticles or agglomerates are visible. An EDS analysis is performed in one of this crystals and the results are depicted in figure 59, together with the SEM image.

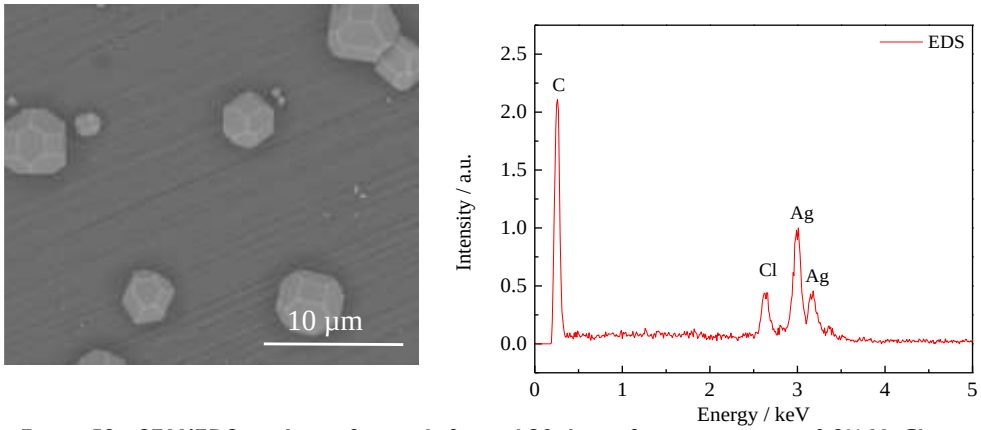

Figure 59 - SEM/EDS analysis of crystals formed 30 days after immersion in 0.9% NaCl

The EDS analysis allows to confirm the formation of AgCl crystals. As previously mentioned the formation of AgCl crystals might be one reason for the stabilization in the Ag ionization.

2.4 Antibacterial Activity

The coatings antibacterial activity is tested against *Staphylococcus epidermidis* (*S. epidermidis*, IE186 strain, a clinical isolate belonging to the CEB Biofilm Group collection), which have been used in the evaluation of antibacterial activity of different indwelling devices and surgical instruments. *S. epidermidis* colonizes the skin and mucous membranes of the human body, representing an important part of its normal microflora, which has emerged in the last few years as the most frequently isolated pathogen in nosocomial sepsis associated with prosthetic device-related infection[23,24]. Zone of inhibition (ZoI) tests, adapted from Kirby-Bauer test[25], are carried out to determine the diffusion of silver from the coatings surface. The halo size is used as a qualitative measure of the coatings antibacterial activity. Figure 61 shows an example of the halo tests carried

out on three different coatings and SEM images performed on their respective coatings surface after halo tests (figures 60 (a,d) to (c,f) correspond to C5 , C4 (A.D.) and C4 (autoclaved), respectively).

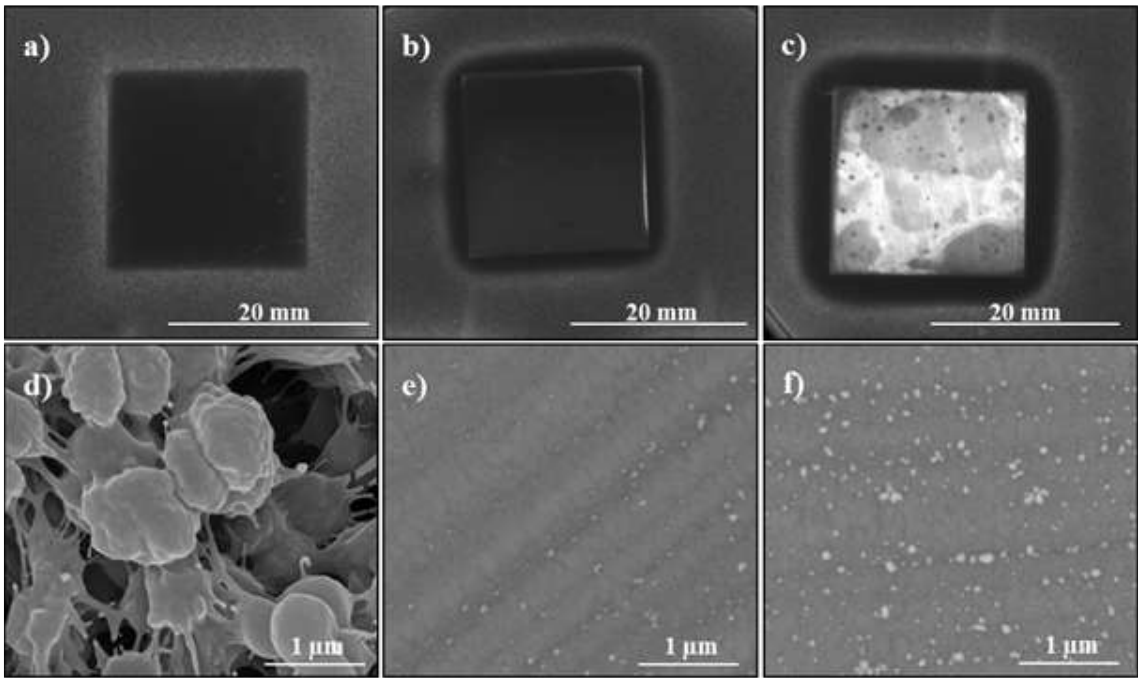

Figure 60 – (a) C5, (b) C4 (A.D.) and (c) C4 (autoclaved) coatings after ZoI assays against S. epidermidis, SEM micrographs of (d) C5, (e) C4(A.D.) and (f) C4(autoclaved) coatings surface after ZoI test.

Both Ag containing coatings show a clear halo surrounding the specimens, with dimensions of about 2.4 ± 0.02 mm and 3.5 ± 0.04 mm for C4(A.D.) and C4(autoclaved), respectively, which suggest that both coatings show antibacterial activity. Conversely, no halo is found around the C5 coating, thus suggesting no antibacterial effect. The SEM micrographs show that the a-C coating surface (figure 61 (d)) is covered with microbial colonies which shows the expected antibacterial inactivity of this material. Conversely no microorganisms are found in the surface of the Ag containing coatings; in fact only Ag agglomerates are visible in the surface of these coatings, which clearly reveals that no bacteria are adhering to the surface. The antibacterial activity of these coatings might be attributed to the release of Ag ions detected by the ICP analysis.

3. Tribological properties in biological medium

3.1 Pin-on-disk testing

The tribological properties of C5 and as-deposited C4 coatings are evaluated by pin-on-disk testing against an alumina counterpart in (i) dry sliding, (ii) HBSS and (iii) HBSS+BSA environments at 37°C. The applied load was 1 N, the ball diameter 10 mm, thus resulting in a contact pressure of 450 MPa. It should be pointed out that this value is lower than those used in Chapter III (690 MPa and 1180 MPa). However, tests with higher contact pressures (690 MPa), led to large areas of coatings delamination in dry sliding conditions, difference attributed to the lack of the adhesion Ti/TiN/TiCN interlayer used in Chapter III. Then, the Pm was reduced down to 450 MPa. The International Organization for Standardization *(ISO) 14242 - Implants for surgery — Wear of total hip-joint prostheses Standard*[26] specifies the loading and displacement parameters for wear-testing machines and corresponding environmental conditions for test. The Standard defines that the number of cycles should be $5x10^6$ and, according to the literature, the mean compressive stresses between the femoral and acetabular component during patient´s movement are around 1 to 10 MPa[27]. In this study the number of cycles is far below the number of cycles defined in the test (which would lead to very long tests); however, the contact pressure values are far higher than those found in real applications. The aim of these tests is mainly to compare a-C coatings, which are already accepted in the market, and Ag containing a-C coatings in body simulated conditions. Regarding the biological fluids, the ISO 1424 Standard[26] defines the use of bovine serum albumin (BSA) (25%) and distilled water (75%). Nevertheless, Hank´s balanced salt solution (HBSS) simulates better the environment found in real conditions, due to the presence of ionic compounds found within the synovial fluid. The chemical composition of these fluids are provided in Annex II.

The results of CoF for C5 and C4 are shown in figure 61 (a) together with the wear rate for both coatings in different environments (figure 61 (b)).

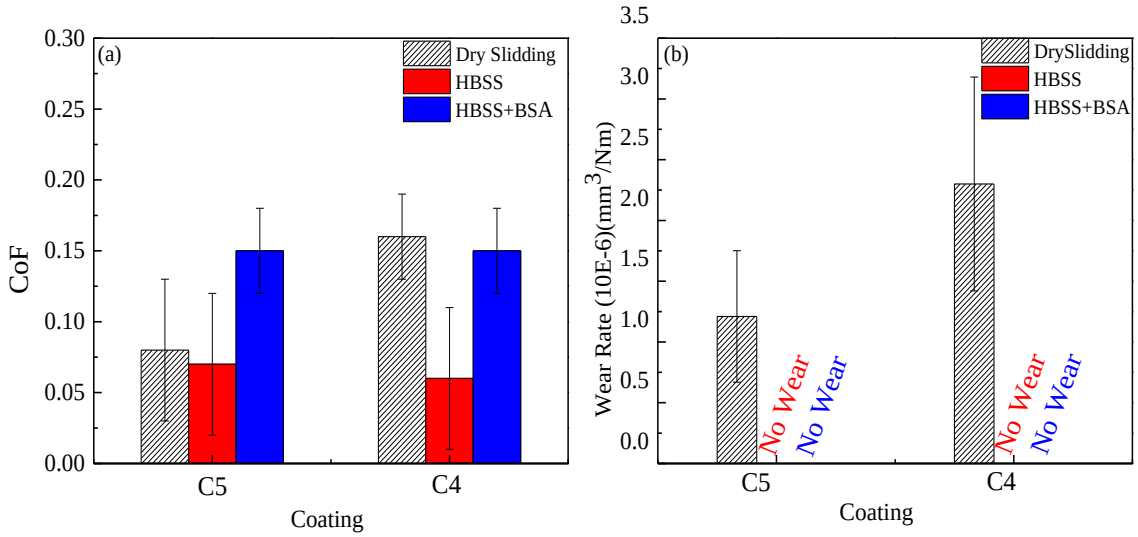

Figure 61 - CoF (a) and (b) wear rates of a-C and Ag/a-C coatings tested in different environments

Regarding a-C coating, the CoF value in dry sliding conditions is about 0.8, a value slightly lower than for Pm=690 MPa (0.10) but higher than at Pm=1180 MPa (0.05) (see Chapter III). Regarding the Ag/a-C nanocomposite coating, both the CoF and wear rate values are higher in relation to a-C coating, in good agreement with what the results reported in Chapter III. However, when tests are performed in liquid environments, no significant variation in the CoF are observed between the two coatings. In both cases, the wear is undetectable. These results show the importance of the contact conditions in the tribological results. In dry conditions, as explained in Chapter III the graphitization and formation of a compact transfer layer in the counterbody, also based in graphitic bonds, justify the low CoF values obtained in dry sliding of pure a-C coating. When silver is incorporated, an Ag rich transfer layer is formed, which in contact with the Ag rich coating surface, gives rise to much higher CoF. When testing in HBSS solution the CoF is similar in both coatings and very close to the one of a-C in dry conditions, in good accordance to Escudeiro et al[28] work on a-C coatings tested in dry sliding and physiological solution (PS) against a Ti6Al4V counterpart, where same CoF values were achieved in both testing conditions. The lubricant effect of the HBSS solution, which avoids the contact between the counterpart and the coating surface, makes the contact conditions in both coatings similar, thus justifying the close values of the CoF. In the Ag/a-C coating, HBSS will inhibit the contact between the surfaces rich in Ag making

decrease the friction coefficient from 0.15 down to 0.05, putting it close to the value of pure a-C sample. Hang et al[29] reported a decrease in the CoF from 0.15 down to 0.06, when simulated body fluid was introduced in pin-on-disk tests of a-C coatings sliding against Ti6Al4V. The presence of HBSS completely prevents the coatings wear, which is not detectable by profilometry measurements.

From the potential application point of view, the tests performed in HBSS+BSA solution are the most important. Again, similar behavior is found for both coatings, with CoF values around 0.15 and no detectable wear. The significant increase in the CoF in relation to the dry sliding of the a-C coating, making it similar to the one of Ag/a-C, enhances one more time the role of the contact conditions and, in particular the albumin, on the friction. In fact, when values are compared to HBSS tests, the difference has to be related with the presence of albumin. Several reports have focused on the influence of albumin containing solutions in the biotribological behavior of different types of surfaces[28-33]. During tribological contact, albumin adheres to the materials surfaces being the friction behavior determined by the albumin properties, i.e. the interaction forces within albumin or between the albumin and the surface of the materials in the contact. Hence, it can act as a lubricant agent, if the CoF in dry sliding is very high, or as a contributor for making harder the easy sliding, as it is the case of a-C coatings. In any case, it protects the surfaces from any wear. Escudeiro et al found that the CoF of Zr/a-C[30] and Ti/a-C[31] coatings showed values in the order of 0.15, when sliding against Ti6Al4V in albumin containing medium, which are similar to the ones shown in figure 61 and very close to those reported by Hang et al[29] (CoF of 0.12) and Anil et al[32] (CoF of about 0.10-0.12), both working a-C based coatings. In Escudeiro et al[28] report, the uncoated Ti6Al4V showed a much higher CoF, with a value of 0.38 in albumin containing solutions. As this value is higher than those achieved in the tests with the coated surface, it can be concluded that the friction values shown in figure 61 are being determined by the interaction forces between albumin and the coatings surface.

The above results allow to predict that, despite the degradation of the tribological properties in dry sliding conditions with the incorporation of Ag, in synovial fluids the tribological behavior should be similar to the one presented by a-C coatings. Nevertheless, it should be pointed out that biotribology is a complex field and these tests should be regarded as preliminaries for the study of the potential application of

silver doped a-C coatings in joint prosthesis. In fact, many other issues need to be understood:

- The influence of Ag incorporation on either the albumin adsorption or its effect on the protein configuration. In fact, the adhesion of albumin is necessary for improving the surface protection against wear, nevertheless, if the protein is denaturated during the interaction with the surface, this will promote the implant rejection. Thus, the understanding of the exact interaction between the protein and the surface is required,
- Despite the wide acceptance of a-C based in the biomedical field, recent studies performed in the group (in the scope of Escudeiro´s PhD thesis) revealed that these coatings enhance the tribological behavior of the base material in unidirectional pin-on-disk test; nevertheless in multidirectional pin-on-disk tests, simulating more closely the real conditions in joint prosthesis, the coatings failed due to interfacial deterioration in corrosive environments under mechanical loading. Thus, further research is necessary to improve the interfacial strength of these coatings,
- The Ag doped coatings showed promising antibacterial activity;, nevertheless, for indwelling device applications, cytotoxicity tests are required in order to get the best compromise between biocompatibility and antibacterial effect.

4. Conclusion

The main goal of this chapter is to analyze the functional properties of the Ag/a-C nanocomposite coating, in particular, the antibacterial activity and the tribological behavior in biological fluids simulating the synovial fluid present in the joint prosthesis environment. Before this analysis, due to its importance on the antibacterial behavior, the Ag ionization rate is also studied. The C4 coating is selected, despite of its non-stable behavior, since the presence of the columnar morphology is expected to enhance the interaction with the biological fluids and to promote a more pronounced antibacterial effect. Then, the effect of the coatings ageing on the functional properties was also analyzed. In total, 3 different samples were studied: a reference a-C layer and the Ag/a-

C(1000) nanocomposite coating in the as-deposited state and aged in an autoclave at 130°C and pressure of 3 bar.

The aged coating´s surface was covered with Ag agglomerates, being the average particle area higher than in the as-deposited coating. Nevertheless, no Ag fibers were found, meaning that the ageing process is at a very initial stage. The ICP results indicated that both coatings showed a similar ionization rate in 0.9 % NaCl. SEM observation after different immersion times shows that Ag particle size was approximately the same in both coatings and increased with time, which is attributed to the Ag particles coalescence induced by a dissolution-precipitation mechanism. This might explain the similar ionization rates, irrespective of the initial particle size. The Ag ionization is stabilized after 7 days of immersion. At this stage about 1 to 1.5% of Ag in the coating is converted into Ag ions which. SEM/EDS analysis revealed the formation of AgCl crystals. In this sense, the stabilization in Ag ionization could be related with the formation of AgCl crystals, which means that any increase in the amount of ionized Ag would result in the increase on the amount of AgCl crystals, but not in the amount of free Ag ions. The antibacterial activity, analyzed through zone of inhibition test against *S. epidermidis*, revealed that both Ag containing coatings are antibacterial, while a-C coating is inactive. These results might be related with the release of Ag ions found by ICP analysis.

The tribological tests are performed by unidirectional pin-on-disk test in three different environments: (i) dry sliding , (ii) HBSS and (iii) HBSSS+BSA. In dry sliding, the degradation of the a-C coatings tribological properties with the incorporation of Ag is observed, with higher CoF and wear rates. Nevertheless, in HBSS and HBSS+BSA solutions the tribological properties (CoF and wear rate) of Ag containing coatings are similar to a-C layer, which was mainly due to the lubricating properties of both solutions which avoid the contact between the counterpart and the coating surfaces, thus, avoiding the formation of Ag-Ag tribological pairs. In this sense, it is predicted that the incorporation of Ag in a-C layers would not result in the loss of the tribological properties, provided that convenient lubricants are used.

References

[1] Consumer Product Inventory, PEN – The Project on Emerging Nanotechnologies, Accessed in May 2015, Available online: http://www.nanotechproject.org/cpi/

[2] S. Chernousova, M.Epple, *Silver as Antibacterial Agent: Ion, Nanoparticle, and Metal*, Angewandte Chemical Internationl Edition, 52 (2013) 1636 – 1653.

[3] Consumer Advisory: Dietary Supplements Containing Silver May Cause Permanent Discoloration of Skin and Mucous Membranes (Argyria), Food and Drug Administration, Accessed in March 2014, Available Online: http://www.fda.gov/Food/RecallsOutbreaksEmergencies/SafetyAlertsAdvisories/ucm184087.htm

[4] J. Hasan, R.J. Crawford, E.P. Ivanova, *Antibacterial surfaces: the quest for a new generation of biomaterials*, Trends in Biotechnology, 31 (5) (2013) 295-304.

[5] D. Campoccia, L. Montanaro , C. R. Arciola, *A review of the biomaterials technologies for infection-resistant surfaces,* Biomaterials, 34 (2013) 8533-8554.

[6] A. Elsaesser, C. V. Howard, *Toxicology of nanoparticles*, Advanced Drug Delivery Reviews, 64 (2012) 129–137.

[7] L. Yildirimer, N.T.K. Thanhb, M. Loizidou, A. M. Seifalian, *Toxicological considerations of clinically applicable nanoparticles*, Nano Today, 6(2011) 585-607.

[8] L. Sintubin, B. De Gusseme, P. Van der Meeren, B. F. G. Pycke, W. Verstraete, N. Boon, *The antibacterial activity of biogenic silver and its mode of actio*n, Applied Microbiology and Biotechnology, 91 (2011) 153 – 162.

[9] Z. Xiu, Q. Zhang, H.L. Puppala, V. L. Colvin, P. J. J. Alvarez, *Negligible Particle-Specific Antibacterial Activity of Silver Nanoparticles*, Nano Letters, 12 (2012) 4271 – 4275.

[10] X.Yang et al, *Mechanism of Silver Nanoparticle Toxicity Is Dependent on Dissolved Silver and Surface Coating in Caenorhabditis elegans*, Environmental Science and Technology, 46 (2) (2012) 1119–1127.

[11] Zoski G., *Handbook of Electrochemistry*, Elsevier, 2007.

[12] Lide D.R. CRC *Handbook of Chemistry and Physics*, CRC Press: Boca Raton, 2009.

[13] J. Liu, R.H. Hurt, *Ion Release Kinetics and Particle Persistence in Aqueous Nano-Silver Colloids*, Environmental Science and Technology, 44 (2010) 2169–2175.

[14] K. Loza et al, *The dissolution and biological effects of silver nanoparticles in biological media*, Journal of Materials Chemistry B, 2 (2014) 1634.

[15] J. Liu, D. A. Sonshine, S. Shervani , R. H. Hurt, *Controlled Release of Biologically Active Silver from Nanosilver Surfaces*, ACS Nano, 4(11) (2010) 6903-6913.

[16] A.Taglietti et al, *Antibiofilm activity of a monolayer of silver nanoparticles anchored to an amino-silanized glass surface*, Biomaterials, (2015) 1779-1788.

[17] E. Unosson, D. Rodriguez, K. Welch, H. Engqvist, *Reactive combinatorial synthesis and characterization of a gradient Ag–Ti oxide thin film with antibacterial properties*, Acta Biomaterialia, 11 (2015) 503-510.

[18] S.B. Sant, K.S. Grill, R.E. Burrel, *Nanostructure, dissolution and morphology characteristics of microcidal silver films deposited by magnetron sputtering*, Acta Biomaterialia, 3 (2007) 341-350.

[19] C. N. Lok, C.M. Ho, R. Chen, Q.Y. He, W.Y. Yu, H. Sun, P. K. H. Tam, J.F. Chiu, C.M. Che, *Silver nanoparticles: partial oxidation and antibacterial activities*, Journal of Biological Inorganic Chemistry, 12 (2007) 527–534.

[20] G. A. Martınez-Castanon, N. Nino-Martınez, F. Martınez-Gutierrez, J. R. Martınez-Mendoza, F. Ruiz, *Synthesis and antibacterial activity of silver nanoparticles with different sizes*, Journal of Nanoparticle Research, 10 (2008) 1343–1348.

[21] G. A. Sotiriou, Sotiris E. Pratsinis, *Antibacterial Activity of Nanosilver Ions and Particles*, Environmental Science Technology, 44 (2010) 5649–5654.

[22] X. Li, J.J. Lnehart, H.W. Walker, *Dissolution-Accompained Aggregation Kinetics of Silver Nanoparticles*, Langmuir, 26(22) (2010) 16690-16698.

[23] I. Carvalho, M. Henriques, J.C. Oliveira, C.F. Almeida, A.P. Piedade, S. Carvalho, *Influence of surface features on the adhesion of Staphylococcus epidermidis to Ag-TiCN thin films*, Science and Technology of Advanced Materials, 14 (2013) 035009.

[24] F. Fitzpatrick, H. Humphreys, E. Smyth, C.A. Kennedy, J.P. O'Gara, *Environmental regulation of biofilm formation in intensive care unit isolates of Staphylococcus epidermidis*, Journal of Hospital Infections, 52(3) (2002) 212-8.

[25] J. Hudzicki, Kirby-Bauer Disk Diffusion Susceptibility Test Protocol, Available Online:http://www.microbelibrary.org/index2.php?option=com_resource&controller=article&article=3189&category_id=1&format=html&print=1&Itemid=73 1

[26] ISO Standard 1424:2002 . *Implants for Surgery – Wear of Total hip-Joint Prostheses*, by Technical Committee ISSO/TC 150, Implants for surgery subcommittee SC4, Bone and Joint Replacements.

[27] H. Yoshida, A. Faust, J. Wilckens, M. Kitagawa, J. Fetto, E.dmund Y. S. Chaao, *Three dimensional dynamic hip contact area and pressure distribution during activities of daily living*, Journal of Biomechanics, 39 (2006) 1996-2004.

[28] Escudeiro A., *Nanocomposite ZrC/a-C(:H) coatings for potential application onto biomedical implants*, s.l. University of Coimbra, 2014.

[29] R. Hang, Y. Qi, *A study of biotribological behavior of DLC coatings and its influence to human serum albumin*, Diamond and Related Materials, 19 (2010) 62–66.

[30] A. Escudeiro, T. Polcar, A. Cavaleiro, *Adsorption of bovine serum albumin on Zr co-sputtered a-C(:H) films: Implication on wear behavior*, Journal of the Mechanical Behaviour of Biomedical Materials, 3(9) (2014) 316-327.

[31] A. Escudeiro, T. Polcar, A. Cavaleiro*, Tribological behaviour a-C and a-C:H films doped with Ti in biological solutions*, Vacuum, 85 (2011) 1144-1148.

[32] M. Anil et al, *Tribological performance of hydrophilic diamond-like carbon coatings on Ti–6Al–4V in biological environment*, Diamond and Related Materials, 19 (2010) 300–304.

[32] S. Calderon V., J.C. Sanchez-Lopez, A. Cavaleiro, S. Carvalho, *Biotribological behavior of Ag–ZrC_xN_{1-x} coatings against UHMWPE for joint prostheses devices*, Journal of the Mechanical Behaviour of Biomedical Materials, 41 (2015) 83-91.

[34] C.F. Almeida Alves, F. Oliveira, I. Carvalho, A.P. Piedade, S. Carvalho, *Influence of albumin on the tribological behavior of Ag–Ti (C, N) thin films for orthopedic implants*, Materials Science and Engineering C, 34 (2014) 22–28.

Outputs and Future Research

The main goal of this thesis is the deposition of Ag/a-C nanocomposite coatings by two alternative routes and the detailed characterization of their structure and stability. The interest of this system from an application point of view is its potential antibacterial activity. Over the past years several reports have been focusing on the use of this nanocomposite coatings for different applications, supported by their interesting tribological, electrical, optical or biological behavior. In any of these potential applications the thermodinamical stability is one of the most important and many times disregarded issues. In fact, among the thousands of reports in the literature on Ag nanocomposite coatings, only a few are dedicated to the detailed characterization of the size and distribution of Ag nanoparticles in the matrix and their evolution with time. In this sense, despite of not discarding the study of the functional properties (antibacterial activity and tribological behavior), the majority of the thesis was devoted to the implementation of an alternative physical vapor deposition method for nanocomposite coatings deposition and the understanding of the coatings stability.

The first part of the thesis consisted in the characterization of Ag/a-C nanocomposite coatings deposited by magnetron sputtering. By varying the number of Ag pellets in the graphite target, different contents of Ag ranging from 0 at.% up to 13 at.% of Ag were achieved in the coatings. The macroscopical observation of the surface of the coatings, allowed to observe their instability when stored in atmospheric conditions. In fact, the initial dark grey color of the as-deposited state was gradually changed to a white appearance which, according to EDS analysis, was due to the enrichment of Ag in the coatings surface. This Ag rich layer was responsible for the degradation of the tribological behavior of the coatings, since the graphitized carbon-carbon tribological pair, characteristic of low friction, was replaced by an Ag-Ag contact with the inherent increase in the friction. With the used co-sputtering method, the size of the Ag nanoparticles increased significantly with the amount of Ag incorporated in the coating. This relationship leads to limitations in the coatings design since it was not

possible to control independently the amount and the size of the incorporated nanoparticles . It should be also noted another major disadvantage of this method: the poor reproducibility. Due to the differences in the erosion rate of the base target and the pellets, non-uniform distribution of the alloying element, either over large substrate areas or along the deposition time, is achieved. Thus, alternative deposition methods for the nanocomposite Ag/a-C coatings had to be tried. Plasma gas condensation (PGC) is a bottom-up physical method for the production of different kinds of nanoparticles, implemented few decades ago by Haberland. Since then, a large number of studies in this deposition method have been performed, mainly focused on the physical aspects related with the nanoparticles growth and the influence of the deposition parameters on the nanoparticles size. Up to now, the co-deposition of nanoparticles by PGC in a matrix coating produced by magnetron sputtering has not yet been reported, although Biederman and co-workers have studied already this approach using chemical vapor deposition methods for the matrix production. Then, in this thesis, the deposition of Ag/a-C coatings has been explored, by combining PGC and MS for Ag nanoparticles and a-C matrix production, respectively. Firstly, the influence of the main deposition parameters (current density and Ar flow) on the Ag particles size distribution was studied in PGC, having been concluded that distributions were broad and cannot be easily controlled and varied. This issue could be solved by the implementation of a mass filter which would allow to select the desired particle size. Besides the problems associated with the huge particle size distribution, the concentration of Ag particles over the substrate surface is very heterogeneous; following the substrate rotation direction the problem can be overcome but, in the transversal direction homogeneous chemical composition can be achieved only in a few centimeters. Therefore, as a first conclusion, PGC method can only be an alternative if much more intensive experimental work is performed to enlarge the covered area to make this method suitable not only for academic research but also for industrial applications. Therefore, with the problems encountered with both the above described methods, in the thesis core work, Ag/a-C coatings were deposited by dual magnetron sputtering, from two independent targets: Ag and C. The minimum and maximum power densities possible to be applied to the Ag and C targets, respectively, were used to allow to reach a final chemical composition of approximately 20 at.% of Ag and 80 at.% of C. Any other possible power combination would lead to an excessive Ag content, out of the desired for the study. Two

nanocomposite coating thicknesses, 250 nm and 1000 nm, were deposited in order to achieve different coatings morphology. Moreover, for specific studies, two multilayer coatings were produced: (i) an Ag/a-C(250) with a carbon barrier layer of 75 nm on the top and (ii) an Ag nanoparticles layer deposited by PGC with an a-C layer of 30 nm for encapsulation. Finally, an a-C(1000) coatings was also deposited as reference for the evaluation of the functional properties. To confirm the formation of the nanocomposite structure, a very thin Ag/a-C nanocomposite was deposited on a TEM grid with a carbon layer. A high density of Ag nanoparticles with a size of about 3 nm were observed inserted in an amorphous matrix, with additional bigger Ag particles with about 20 nm in size. The SEM analysis performed in the Ag/a-C(250) and Ag/a-C(250)+a-C(75) allowed to confirm the presence of 20 nm sized Ag particles only on the surface of the monolayer coating. The absence of Ag particles on the bilayer coating, in both surface and cross-section observation, suggested a bimodal distribution with 20 nm sized particles sitting on coatings surface, if lateral coalescence is allowed, while the bulk is composed of Ag nanoparticles 3 nm size. This hypothesis was confirmed by GIXRD analysis of the Ag/a-C layers at different incidence angles. This method allowed to differentiate Ag diffraction signals from the surface and the bulk, and Ag particle size determined by Scherrer method gave values close to those observed by TEM. The cross-sectional observations of Ag/a-C(1000) and Ag/a-C(250) coatings showed columnar and featureless morphologies, respectively.

Chapter V was devoted to the understanding of the coatings stability with time as well as of the possible Ag diffusion mechanisms intervening in the process. The thinner and compact Ag/a-C(250) coating was stable with time in atmospheric conditions, while the thicker and columnar one formed an Ag rich surface layer, forming nanowhiskers with about 10 nm of diameter and hundreds of nanometers in length. GDOES depth profiling confirmed that the thinner coating was stable during a period of 6 months; in the thicker coating, the presence of an Ag rich surface layer was confirmed, with Ag decreasing in the bulk from 18 at.% down to 14 at.% homogeneously across the entire coating thickness. This results suggest that Ag is moving from the interface with the substrate within the nanocomposite column boundaries, agglomerating and obliging Ag to sort as nanowhiskers, which diameter is similar to the column boundary spacing. In order to get some insight about Ag mobility within the compact a-C layers, an Ag nanoparticles layer was covered with a 30 nm thick a-C layer and observed by TEM in

an *in-situ* heating experiment. The a-C layer completely prevented the Ag nanoparticles sintering, opposing to the results of a similar experiment without additional barrier layer, reported in the literature. These results strongly suggest that Ag is immobile when inside the compact a-C layers, contrasting with its easy movement along free spaces, such as the column boundaries or the outwards surface. The influence of the humidity in the coatings stability was also accessed. The coatings stored in low humidity levels are stable with time, while increasing the humidity levels promoted the formation of big particles sizes and Ag nanowhiskers on the surface. GIXRD results revealed that the particles grew through a coalescence process and not by agglomeration. Moreover, neither changes in the stress state nor the formation of oxides occurred with time, phenomena found in the whiskering of soft metals. In this sense, the exact mechanism of Ag whiskering still remains unclear. Nevertheless, the observation of the coalescence growth mechanism suggests a dissolution-precipitation growth mechanism. More detailed studies with simulation and experiments with *in-situ* TEM observation of the Ag growth in different humidity levels are required.

The final Chapter of the thesis aimed to analyses the coatings functional properties. As suggested by the thesis title, the main goal was to develop antibacterial surfaces, for a wide range of applications (indwelling medical devices, surgical instruments, food packages, among others). In order to get some insights about the influence of Ag nanocomposites ageing on the ionization rate and, consequently, on the antibacterial activity, an Ag/a-C(1000) coating was compared in the as-deposited and the aged states with a reference a-C coating with similar thickness. The Ag ionization rates measured over a period of 1 month showed a linear increase over a period of 7 days; thereafter the Ag ionization was stabilized. Both as-deposited and aged coatings showed a similar behavior, despite the higher initial Ag particle size found in the aged coating. The stabilization in the Ag ionization rate was related with the formation of AgCl crystals detected in SEM/EDS analysis. In dry sliding conditions, the presence of Ag increased the CoF and wear rate of the coatings; nevertheless, in Hank´s Balanced Solution (HBSS) and HBSS with bovine serum albumin (BSA) wear was detected neither in a-C nor in Ag/a-C coatings. The dominant role of albumin, determines the friction behavior and protects the coatings from wear.

As a final conclusion, the results achieved showed that the Ag/a-C system seems to be promising for application as antibacterial coating. Nevertheless, more studies are

needed in order to reach the best compromise between antibacterial activity and biocompatibility. In addition, the long term antibacterial activity must be evaluated in more severe test conditions at longer times. Finally, more intensive research is required to optimize the tribological behavior of the coatings in real conditions, especially in what concerns the coatings interfacial strength.

Annex I

This Annex aims to provide all the details about the calculations related with the determination of:

- % of Ag-NP sitting in column boundaries and interfaces;
- Determine if it is possible to form Ag fibers with the amount of Ag-NP present in the column interfaces;
- Determine the influence of coating´s morphology (columns diameter and intercolumnar spacing) on the fibers heigth/length.

This Annex aims to complement the results presented in Chapter V – Section 5.1.

1.Determination of the distance between two Ag nanoparticles

According to EPMA analysis the chemical composition in terms of weight % is: 28.30 wt. % C; 70.19 wt. % Ag and 1.50 wt. % O. These values are used to estimate the % of volume of C and Ag; the weight values are rounded to 70 wt. % Ag and 30 wt. %C, and the oxygen is not considered in the analysis. The volume is determined through the equation:

$$\rho = \frac{m}{V} \tag{A.1}$$

The ρ values considered were 10.5 g/cm^3 [1] for Ag and 2.2 g/cm^3 for carbon, which represent the theoretical density values of bulk Ag and sputtered carbon a-C, according to Robertson[2]. Accordingly, two equations can be found, which allow to predict the % of volume of each of the elements:

$$\frac{m_{Ag}}{M_T} = 10.5 g/cm^3 V_{Ag} \tag{A.2}$$

$$\frac{m_C}{M_T} = 2.2 g/cm^3 V_C \tag{A.3}$$

Where m_C and m_{Ag} are the carbon and silver mass and M_T the total mass, considering $m_{Ag} + m_C$.

Accordingly, the volume % of each element will be:

$$V_{Ag} = 33\%$$

$$V_C = 67\%$$

The GIXRD results reveal an Ag grain size of 2-3 nm, and according to the HRTEM cross-sectional observation the Ag nanoparticles size is around 2.5 nm. Despite some heterogeneities in Ag size distribution and also on its dispersion in the matrix as suggested by TEM analysis, in this calculations it is assumed that the sample is perfectly

homogeneous – the particles all have exactly the same size (Ø=2.5 nm) and the distance between two particles is always constant, with a length l. The Ag distribution is imagined as shown in the figure below, in an array that resembles the cubic primitive cell.

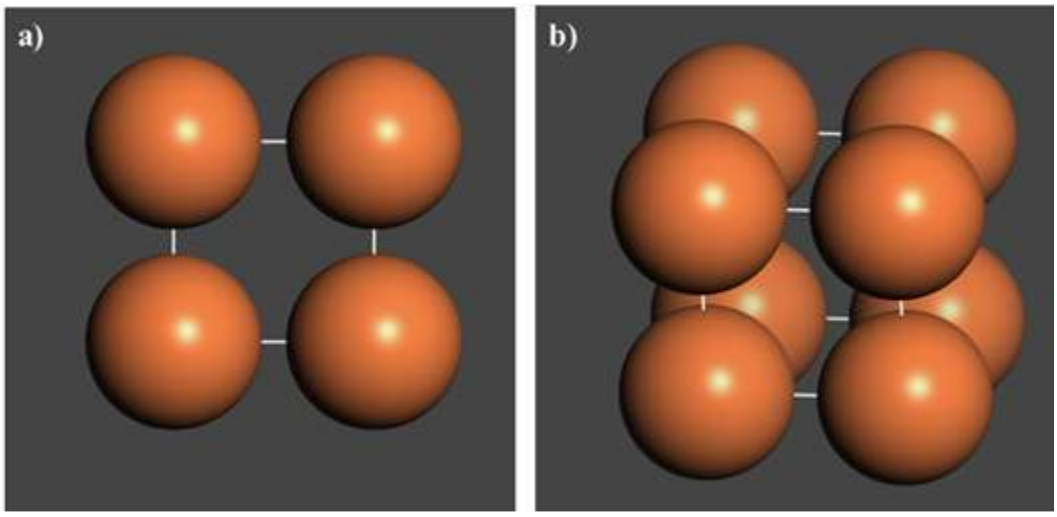

Figure A 1 1– Schematic representation of Ag distribution in a-C coating

If we imagine this type of distribution of Ag nanoparticles in the matrix, than the calculation of the distance l is very simple. Assuming that each Ag particle is a sphere of diameter Ø=2.5nm, the volume of one Ag nanoparticle is:

$$V = \frac{4}{3}\Pi R^3 \tag{A.4}$$

$$V = 8.2\ nm^3$$

Knowing that this value represents 33% of the total volume, then the volume of one cell is:

$$V = 24.85\ nm^3$$

Which means that $a = 2.9\ nm$. Each side, a, is occupied by two spheres radius, which means that the distance between two successive Ag nanoparticles is:

$$\boldsymbol{l} = 2.9nm - 2.5nm = \mathbf{0.4}\boldsymbol{nm}$$

2. Determination of the number of Ag nanoparticles in one column and at the surface of a column

The SEM top-view micrographs allowed to determine the mean dimensions of a column. As previously shown in Chapter V. Section 5.1, the polymer and SS316L coated Ag/a-C samples show different morphologies, thus, for each type of coating different column diameters, column spacing's and thicknesses must be considered. The SEM images used in the determination of column diameters are shown in the figure A1 2. The mean size of major and minor dimensions were determined taking into account the dimensions of 5 columns (see Table A1 1), which are indicated in the SEM micrographs shown in figure A1 2.

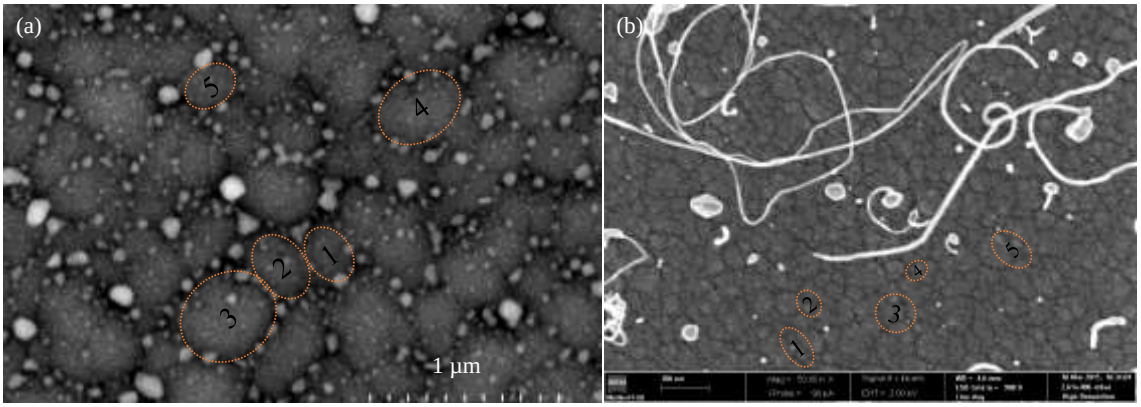

Figure A 1 2– SEM micrographs of Ag/a-C coatings deposited on (a) polymer foil and (b) SS316L with indication of column´s diamet

Table A 1 1– Mean dimensions of columns present in Ag/a-C coatings deposited on polymer foil and SS316L

	Polymer Foil		SS316L	
	Major	**Minor**	**Major**	**Minor**
1	300	256	190	108
2	395	281	122	98
3	487	419	176	175
4	477	339	103	82
5	256	306	196	129
Mean	**383±103**	**320±63**	**157±42**	**118±36**

The SEM micrographs presented in figure A1 2 indicate that the column size in each coated substrate shows a wide size distribution. Nevertheless, in order to get some insight about the mean size 5 columns with different sizes were selected. The results shown in the SEM micrographs and Table A1 1 indicate that the polymer coated Ag/a-C nanocomposite shows a higher column diameter in relation to SS316L coated nanocomposite.

How many Ag nanoparticles exist in one single column?

Let's imagine the column as a cylinder shaped with a radius of $R = 175\ nm$ and height of $h = 750\ nm$ (in case of polymer foil coated Ag/a-C) where Ag nanoparticles are spheres with a diameter Ø=2.5 nm. In this situation the total volume of the column as well as the carbon and Ag nanoparticles volumes, based on the above 66% / 33% ratio, can be calculated. Then, from the individual volume of each nanoparticle, the total number of Ag nanoparticles in one single column can be determined. A similar approach is used for SS316L coated sample, where the $R = 68.8\ nm$ and $h = 1000\ nm$ dimensions are considered. Accordingly the number of Ag nanoparticles in a single column can be estimated following the calculations provided in Table A1 2.

Table A 1 2– Determination of number of Ag-NP in a column

	Polymer Foil	**SS316L**
Column Volume (nm^3)	$V_T = \pi h R^2$	
	7.22*10^7	1.49*10^7
Carbon volume in 1 column (nm^3)	$V_C = 0.67 * V_T$	
	4.83*10^7	9.96*10^6
Ag volume in 1 column (nm^3)	$V_{Ag} = 0.33 * V_T$	
	2.38*10^7	4.91*10^6
Volume of 1 Ag sphere (nm^3)	$V_{nanoAg} = \frac{4}{3}\pi R^3$	
	8.18	
Number of Ag-NP in 1 column	**2.91*10^6**	**6.00*10^5**

How much of Ag-NP are sitting in column boundaries, coating´s surface and interface with substrate?

Knowing the total number of Ag nanoparticles in the column we can now estimate if all these particles are sitting in the column interfaces (means column boundaries and top of a column in interface with air and bottom of a column in interface with substrate). Let´s imagine the column boundary surface as a rectangle (2D projection of cylinder outer surface) with a length similar to the perimeter of the base and the width similar to the column height (see figure A1 3). The surface area of this rectangle represents the column boundaries surface area and it is given by:

$$A_{CB} = 2\pi Rh$$

The surface area of the top and bottom of one column is given by:

$$A_s = \pi R^2$$

The total surface area of one column interface is the sum of the column boundary area, coating´s top surface (interface with air) and bottom surface (interface with substrate) areas, which is given by:

$$A \quad = 2\pi Rh + 2\pi R^2$$

Considering that the particles have a $Ø = 2.5\ nm$ and are separated by a distance $l = 0.4\ nm$, then the area occupied by each nanoparticle is given by:

$$A_{Ag} = 2.9\ nm * 2.9\ nm = 8.41\ nm^2$$

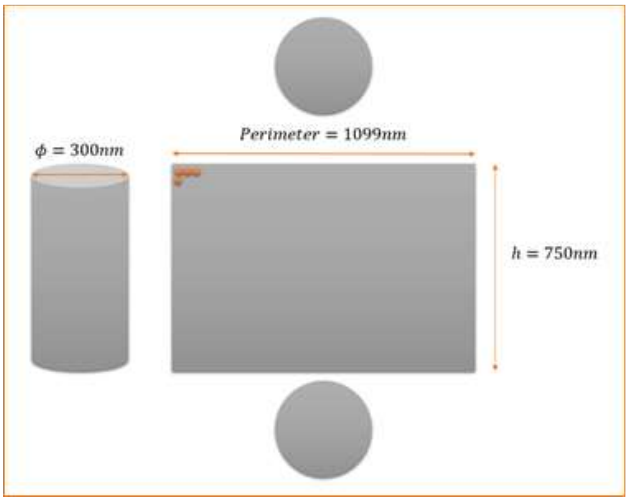

Figure A1 1– 2D projection of the column interfaces (the dimensions represent the polymer foil coated Ag/a-C)

Assuming this simple calculations and the total number of Ag particles in one single column (see Table A1 2), it is possible to determine the number of Ag particles in a column boundary (rectangle projected in 2D) and base (coating´s top-surface and interface with substrate) and the total number of Ag-NP in the column interfaces (sum of the Ag-NP present in column boundaries and surfaces in interface with air and substrate); as well as the % of particles sitting in this surfaces. The resulted are presented in Table A1 3.

Table A 1 3– Number and % of Ag-NP in column boundaries, base and column interfaces

	Number of Ag		**% of Ag**	
	Polymer Foil	**SS316L**	**Polymer Foil**	**SS316L**
Column Boundaries	$9.81*10^4$	$5.14*10^4$	3.37	8.57
1 Base	$1.14*10^4$	$1.77*10^3$	0.39	0.29
Column Interfaces	$1.21*10^5$	$5.49*10^4$	4.15	9.15

The calculations allow to confirm that Ag nanoparticles are sitting either in column interfaces and also inside the columns. It also clear that the % of Ag-NP present in interfaces is low (about 4.15% and 9.15%), and becomes lower in columns with higher diameters.

3.Determination of the volume of Ag in column boundaries and the size of Ag fibers for different column boundary spacing´s

Consider that the coating is composed of columns with a cylinder shape where spherical Ag nanoparticles with $\phi = 2.5\,nm$ are sitting inside the column boundaries and also in the column interfaces (see figure A1 3), which are separated at a distance of $l = 0.4\,nm$. Now let´s us consider that only particles sitting in the columns interfaces (excluding the particles in top-surface) contribute to the fibers formation. The question is: ***is it expectable that the amount of Ag sitting on these surfaces can form the fibers or agglomerates that are observed by SEM or TEM?***

By taking into account the number of Ag-NP present in column boundaries + number of Ag-NP present in the interface with substrate in one single column it is possible to determine the volume of Ag in this interfaces (see Table A1 4). Now if we consider that the fibers can only grow in between the column boundaries, their diameter should be similar to the column boundary spacing. This parameter is quite difficult to measure, nevertheless, based on this idea it is easy to determine the fibers diameter from SEM top-view micrographs, which should be similar to the column spacing. Once again the SEM top-view micrographs of polymer foil and SS316L coated samples are shown and the diameter of different Ag fibers is indicated.

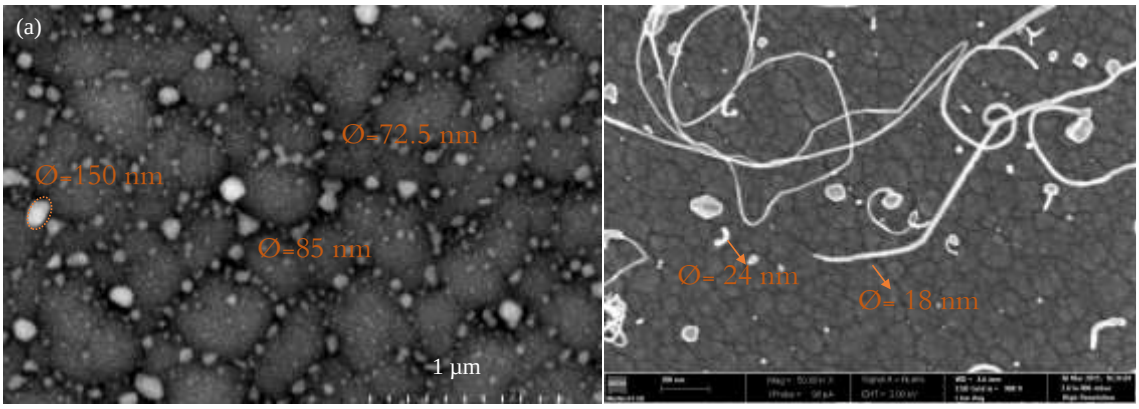

Figure A 1 3– SEM micrographs of (a) polymer foil and (b) SS316L coated Ag/a-C with indication of fiber´s diameter

By knowing the volume of Ag present in column interfaces and fibers diameter/intercolumnar spacing it is possible to determine the fibers height for different intercolumnar spacing´s. It is assumed that the fibers also show a cylindrical shape. The values of fibers height for different fiber diameters are shown in Table A1 4.

Table A I 4– Determination of fibers height

	Polymer Foil		SS316L	
Number of Ag	$1.09*10^5$		$5.32*10^4$	
Volume of Ag	$8.96*10^5$		$4.35*10^5$	
Fiber Ø (nm)	85	150	18	24
Height (nm)	158	51	1709	961

The results presented above clearly indicate that as the column boundary spacing becomes larger the height of the fibers becomes lower. This also explains why in Ag/a-C coatings deposited over a polymer substrate no fibers are visible, while in SS316L the formation of large fibers is enhanced in regions with low columnar spacing and higher column diameter, due to the presence of larger amounts of Ag-NP.

References

1 – Chang R., *Química*, 8th Edition, Mc-Graw Hill, 2005, Spain.

2 – J.Robertson, *Diamond-like amorphous carbon*, Materials Science and Engineering R, 37 (2002) 129-281.

Annex II

In this Annex the chemical composition of SS316L substrates and HBSS solution prepared for the tribological tests are provided.

Table A II 1 – Chemical composition of SS316L

Element	Wt.%
Fe	68.40
Cr	16.40
Ni	11.10
Mo	2.28
Mn	1.30
Si	0.39
P	0.06
C	0.03

Table A II 2- Chemical composition of Hank´s Balnced Salt Solution prepared for tribological tests

Component	g/L
Calcium chloride	0.1855
Magnesium sulfide 7H20	0.204
Potassium chloride	0.4
Monopotassium phosphate	0.06
Sodium bicarbonate	0.35
Sodium chloride	8.00
Disodium phosphate	0.0475